# DETERMINATION OF THREE DIMENSIONAL TRACE ELEMENT DISTRIBUTIONS BY THE USE OF MONOCHROMATIC X-RAY MICROBEAMS

by

Paul Boisseau

B.S., Massachusetts Institute of Technology
(1978)

Submitted to the Department of Physics
in Partial Fulfillment of the Requirements
for the Degree of

DOCTOR OF PHILOSOPHY

at the

MASSACHUSETTS INSTITUTE OF TECHNOLOGY

January, 1986



Signature of Author Signature redacted
Department of Physics
January, 1986

Certified by Signature redacted
Prof. Lee Grodzins
Thesis Supervisor

Accepted by Signature redacted
Prof. George F. Koster
Chairman, Graduate Committee

# DETERMINATION OF THREE DIMENSIONAL TRACE ELEMENT DISTRIBUTIONS BY THE USE OF MONOCHROMATIC X-RAY MICROBEAMS

by

Paul Boisseau

Submitted to the Department of Physics
in January 1986, in partial fulfillment of the requirements
for the degree of Doctor of Philosophy

Abstract

The technique of x-ray induced x-ray fluorescence analysis has long been used for the determination of trace element concentrations for a wide variety of specimens. The development of high flux density synchrotron beams allows the technique to be extended to provide spatially resolved analysis using x-ray microbeams. X-ray tomographic analysis for the imaging of density variations in the interior of materials has been developed during the past 15 years. In this thesis, the x-ray tomographic technique has been combined with x-ray fluorescence using high flux density monochromatic synchrotron beams. The result is the first tomographic determination of trace element distributions through the interior of objects. Trace elements are detected by fluorescent excitation of characteristic x-rays along a collimated beam path scanned through the specimen. Tomographic reconstruction techniques are used to determine planar distributions. Estimates are made of sensitivity in the tomographic mode. Experimental results of the technique are presented.

Thesis Supervisor: Dr. Lee Grodzins
Title: Professor of Physics

## ACKNOWLEDGEMENTS

Over the last few years, I have been lucky enough to work on a whole range of exciting topics, and my education could not have been more suitable to my interests and abilities. This state of affairs is wholly due to my thesis advisor, Lee Grodzins. Lee always seemed to know when to get me involved in something that was a little beyond my abilities, as well as when to leave me alone. His continous personal and professional concern for me has made all of the difference.

One of my oldest friends at MIT, Bob Ledoux always had the ability to look on the bright side of things, even when there wasn't one. His combination of hard work and easygoing attitude has always been an inspiration, although admittedly it never made much sense to me.

Evita Vulgaris has constantly been a reminder that there are people who are just nothing like me. Her friendship, both in and out of the lab, has been and always will be appreciated.

Bill Nett has been a good friend during all of my student days, and has helped me out in many ways. I will always appreciate his help, even though I have my own car now.

I would like to thank Phil Kesten for his years of friendship and support, as well as for helping out in the Last Days of the Thesis. Next time I will start the thesis a week earlier.

This thesis would have been quite different with no data, and I thank Cullie Sparks and the Oak Ridge synchrotron research group for their support and flexibility.

My first experience with research was with the Scanning Proton Microprobe. Jean Ryan showed remarkable calmness in the face of a number of near disasters, and allowed me to acquire a great deal of experience over the years.

My first experience with 'real world' research was due to the people at Eaton/Oxygen. I would like to thank them for the chance to develop the optical tomography project.

The Heavy Ion Group has always been a unique group, and my experiences here would not have been the same without people like Stuart Gazes and Andy Smith, or

for that matter any of the past or present members. I have confidence that the group will always have the peculiar way that made my work at MIT such a pleasure

Finally, I would like to thank the members of my family for the support that they have shown over the years- I hope that the thesis will finally show them just exactly what I have been doing all this time.

# TABLE OF CONTENTS

## LIST OF FIGURES

## REFERENCES


[Ba72] W. Bambynek et al. *Rev. Mod. Phys* **44** (Oct. 1978).

[Bi63] L.S. Birks et al, *J. of Applied Physics* **35**, 2578 (1963).

[Bu78] T.F. Budinger *A Primer on Reconstruction Algorithms* LBL-8212, (1978).

[Co79] J.A. Cookson *Nucl. Inst. & Meth.* **165**, 477 (1979).

[Fo74] F. Folkman et al *Nucl. Inst. & Meth.* **84**, 141 (1974).

[Ga70] J.D. Garcia *Phys. Rev.* **1** , 5 (1970).

[Ga78] R.K. Gardner and T.J. Gray *Atomic Data and Nucl Data Tables* **21**, 515 (1978).

[Go77] F.S. Goulding and J.M. Jaklevic *Nucl. Inst. & Meth.* **142**, 323 (1977).

[Go78] J. Gould *Science* **201**, 1026 (Sept. 1978).

[Go] B.M. Gordon, Sensitivity Calculations for Multielemental Trace Analysis by Synchrotron Radiation Induced X-Ray Fluorescence, *Nucl. Inst. & Meth.*, in press.

[Gr83] L. Grodzins *Nuc. Instr. Meth.* **218** , 203 (1983).

[Gr83b] L. Grodzins and P. Boisseau *IEE Trans. Nuc. Sci.* **30** , (April, 1983).

[Gr83c] L. Grodzins *Sixth International Conference on Ion Beam Analysis* Tempe, Arizona May 23-27, 1983

[Gr] L. Grodzins *Electron, Proton, and Photon induced X-ray Microprobes: Analytic Sensitivity vs. Spatial Resolution,* J. of Neurotoxic., to be published.

[Ho75] P. Horowitz, L. Grodzins *Science* **189** , 797 (1975).

[Ho82] M.R. Howells and J.B. Hastings *International Conference on X-Ray and VUV Synchrotron Radiation Instrumentation,* Hamburg, Germany, August 9-13, 1982

[Ic83] G.E. Ice and C.J. Sparks *Proc. Third National Conference on Synchrotron Radiation Instrumentation,* Brookhaven National Laboratory Sept. 12-14, 1983, (1983).

[In] Indiana University Cylotron Facility Proposal

[Jo70] T.B. Johansson, R. Akselsson and S.A.E. Johansson, *Nucl. Inst. & Meth.* **84**, 141 (1970).

[Jo76] S.A.E. Johansson and T.B. Johansson *Nuc. Instr Meth.* **137** , 473 (1976).

[Ki83] S. Kirkpatrick et al *Science* **220**, (May 13, 1983).

[Li78] T.- L. Lin et al *Nucl. Inst. & Meth.* **151**,439 (1978).

[Ma] M.F. Mahrok et al, Proton Induced X-Ray Fluorescence Analysis and its Application to the Measurement of Trace Elements in Hair, submitted to *Analytical Chemistry*

[Mu72] R.O. Muller *Spectrochemical Analysis by X-ray Fluorescence*, Plenum Press (1972).

[Pe] M. Peisach et al, PIXE Induced X-Ray Fluorescence Analysis, *Annual Research Report of the Nuclear Institute of van die Suidelike Univeriteite* (1981)

[Sm86] H. Smith, Massachusetts Institute of Technology, Private communication.

[Sp80] C. J. Sparks *Sychrotron Radiation Research* Plenum Publishing , (1980).

[Sp82] C. J. Sparks et al *Nucl. Inst. & Meth.*, **195**, 73 (1982).

[To84] *Proc. Topical Meeting on Industrial Applications of Computed Tomography and NMR Imaging*, August 13-14, 1984 Optical Society of America. (1984)

[Wo73] R. Woldseth *X-Ray Energy Spectrometery,* Kevex Corp. (1973).

# CHAPTER 1
## Introduction

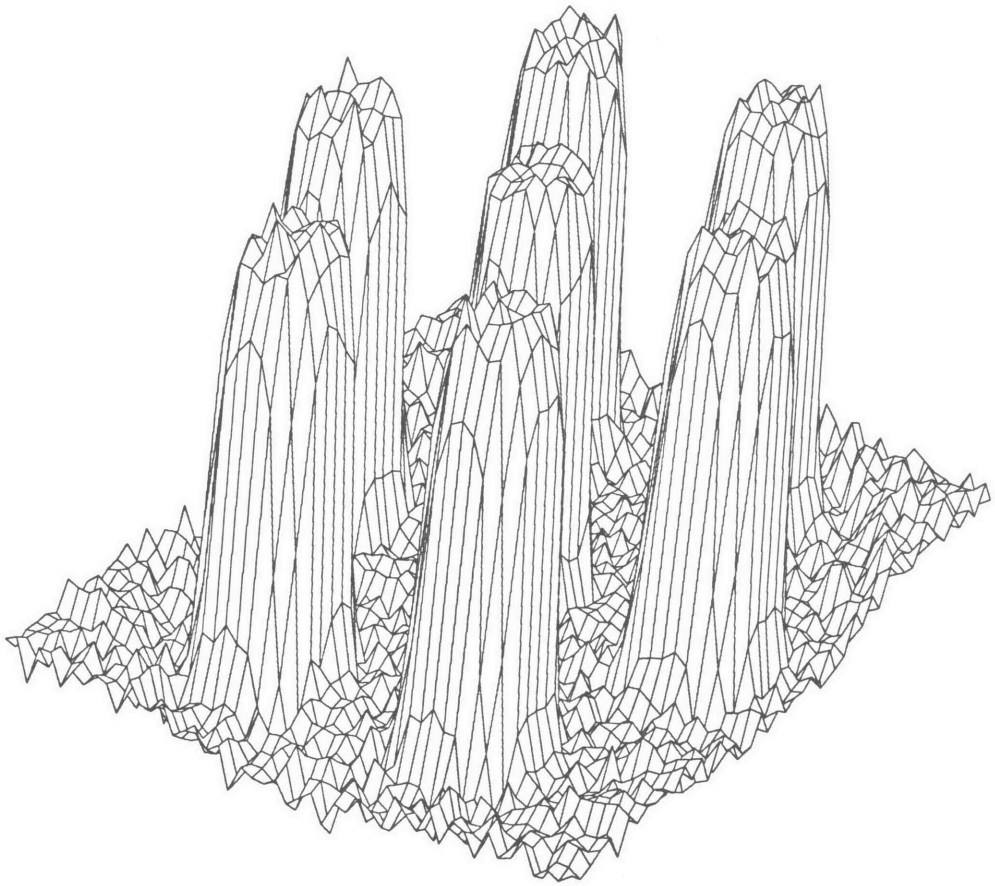

# CHAPTER 1
## Introduction

The detection of trace elements has long been one of the most important steps in the solution of many problems in material analysis. The use of chemical methods has been augmented by a large number of physical methods starting with optical spectroscopy and including mass spectrometry, x-ray fluorescence, neutron activation, and proton induced x-ray emission. As new technology is created and old technology is refined, these analysis techniques will continue to grow in importance.

Although for many analysis problems there exists an appropriate means of analysis, there are significant problems for which the ideal technique does not exist. A relatively ideal general analytical technique might have the following characteristics:

The ability to detect concentrations $\leq 10^{-9}$.
Sensitivity to a wide range of element/matrix combinations.
The ability to provide spatial resolution.
Instrumental simplicity.

We might extend the requirements to include characteristics not strictly elemental in nature, such as molecular structure or chemical environment. Frequently however, an elemental analysis that is insensitive to these factors is desired.

Techniques which utilize the detection of induced characteristic x-rays are of particular importance. With these, the sample is bombarded with radiation capable of ejecting inner shell electrons from the trace element atoms. The cross-section for ionization depends on both the Z of the target atom and the type of incident radiation (Figure 1.4). The atom will de-excite through the emission of an x-ray or Auger electron. The probability of x-ray emission, the fluorescence yield, is a strong function of atomic number. As shown in Figure 1.2 the fluorescence yield is small for atoms of low atomic number. Although *ionization* cross-sections increase for decreasing Z, the actual x-ray yield is determined by the product of ionization cross-section and fluorescence yield.

De-excitation takes place when an electron vacancy is filled by an electron transition from a higher energy level. In the case of the removal of an n=0 electron, the

most likely transition will be from the n=1 level. The resulting x-ray is referred to as a $K_\alpha$ x-ray. The K refers to the initial vacancy and the $\alpha$ refers to the source level. Actually, the $K_\alpha$ is made up of two closely spaced lines, the $K_{\alpha 1}$ and the $K_{\alpha 2}$. This is due to the splitting of the L shell energy levels. Other x-rays, corresponding to transitions to the K shell from higher shells, appear as the $K_\beta$, $K_\gamma$ etc. Transitions to the n=1 level are labelled as the L lines. The transition energy from level n to level m is given by the following:

$$E_{n_1,n_2} = RZ^{*2}(\frac{1}{n_1^2} - \frac{1}{n_2^2})/eqno(1.1)$$

where $Z^*$ is the effective charge of the nucleus due to screening. The energy of the inner atomic energy levels is not appreciably affected by the atomic environment so that matrix effects can usually be ignored.

The induced x-rays are detected with an energy or wavelength dispersive detector. In most cases, the identification of the element corresponding to a particular energy x-ray is unambiguous; the x-ray spectrum is a unique signature. The concentration of the trace elements in the sample can be derived from from the x-ray intensities. This may be done either by knowing cross-sections and beam intensity, or through the use of internal or external trace element standards.

Induced x-ray analysis techniques may be characterized by the method of excitation. The incident beam may be made up of electrons, protons, heavy ions, or photons.

### Electron Bombardment

The scanning electron microprobe (SEM) uses a beam of energetic electrons to excite the target atoms. The technique is capable of very high spatial resolution, but has relatively poor sensitivity. The limit to sensitivity is due to the large bremsstrahlung background, which is produced when the incident electron beam is stopped in the sample. The count rate due to this continuum background can be minimized by increasing the energy resolution of the detector. An optimum situation is to use a detector with an energy resolution equal to the natural line width of the induced x-ray line. This limit can be approached through the use of crystal spectrometers.

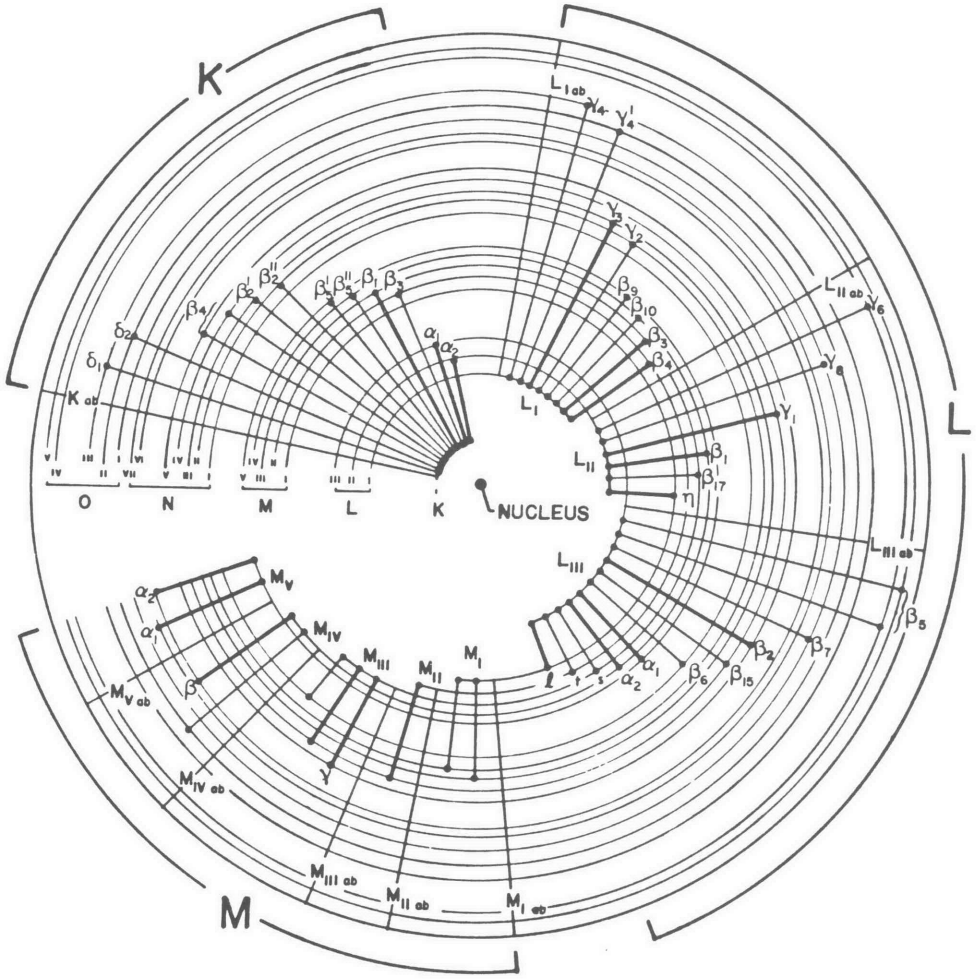


**Figure 1.1**

Atomic model, showing electron transitions that may follow electron vacancies. Transitions are labeled with conventional notation for associated emission lines. [Wo75]

| Z | Element | $\omega_K$ | | $\bar{\omega}_L$ | | $\bar{\omega}_M$ | Z | Element | $\omega_K$ | | $\bar{\omega}_L$ | | $\bar{\omega}_M$ | |
|---|---|---|---|---|---|---|---|---|---|---|---|---|---|---|
| 4 | Be | 4.5 | -04 | | | | 45 | Rh | 8.07 | -01 | | | | |
| 5 | B | 10.1 | -04 | | | | 46 | Pd | 8.19 | -01 | | | | |
| 6 | C | 2.0 | -03 | | | | 47 | Ag | 8.30 | -01 | 5.6 | -02 | | |
| 7 | N | 3.5 | -03 | | | | 48 | Cd | 8.40 | -01 | | | | |
| 8 | O | 5.8 | -03 | | | | 49 | In | 8.50 | -01 | | | | |
| 9 | F | 9.0 | -03 | | | | 50 | Sn | 8.59 | -01 | | | | |
| 10 | Ne | 1.34 | -02 | | | | 51 | Sb | 8.67 | -01 | 1.2 | -01 | | |
| 11 | Na | 1.92 | -02 | | | | 52 | Te | 8.75 | -01 | 1.2 | -01 | | |
| 12 | Mg | 2.65 | -02 | | | | 53 | I | 8.82 | -01 | | | | |
| 13 | Al | 3.57 | -02 | | | | 54 | Xe | 8.89 | -01 | 1.1 | -01 | | |
| 14 | Si | 4.70 | -02 | | | | 55 | Cs | 8.95 | -01 | 8.9 | -02 | | |
| 15 | P | 6.04 | -02 | | | | 56 | Ba | 9.01 | -01 | 9.3 | -02 | | |
| 16 | S | 7.61 | -02 | | | | 57 | La | 9.06 | -01 | 1.0 | -01 | | |
| 17 | Cl | 9.42 | -02 | | | | 58 | Ce | 9.11 | -01 | 1.6 | -01 | | |
| 18 | Ar | 1.15 | -01 | | | | 59 | Pr | 9.15 | -01 | 1.7 | -01 | | |
| 19 | K | 1.38 | -01 | | | | 60 | Nd | 9.20 | -01 | 1.7 | -01 | | |
| 20 | Ca | 1.63 | -01 | | | | 61 | Pm | 9.24 | -01 | | | | |
| 21 | Sc | 1.90 | -01 | | | | 62 | Sm | 9.28 | -01 | 1.9 | -01 | | |
| 22 | Ti | 2.19 | -01 | | | | 63 | Eu | 9.31 | -01 | 1.7 | -01 | | |
| 23 | V | 2.50 | -01 | 2.4 | -03 | | 64 | Gd | 9.34 | -01 | 2.0 | -01 | | |
| 24 | Cr | 2.82 | -01 | 3.0 | -03 | | 65 | Tb | 9.37 | -01 | 2.0 | -01 | | |
| 25 | Mn | 3.14 | -01 | | | | 66 | Dy | 9.40 | -01 | 1.4 | -01 | | |
| 26 | Fe | 3.47 | -01 | | | | 67 | Ho | 9.43 | -01 | | | | |
| 27 | Co | 3.81 | -01 | | | | 68 | Er | 9.45 | -01 | | | | |
| 28 | Ni | 4.14 | -01 | | | | 69 | Tm | 9.48 | -01 | | | | |
| 29 | Cu | 4.45 | -01 | 5.6 | -03 | | 70 | Yb | 9.50 | -01 | | | | |
| 30 | Zn | 4.79 | -01 | | | | 71 | Lu | 9.52 | -01 | 2.9 | -01 | | |
| 31 | Ga | 5.10 | -01 | 6.4 | -03 | | 72 | Hf | 9.54 | -01 | 2.6 | -01 | | |
| 32 | Ge | 5.40 | -01 | | | | 73 | Ta | 9.56 | -01 | 2.3 | -01 | | |
| 33 | As | 5.67 | -01 | | | | 74 | W | 9.57 | -01 | 3.0 | -01 | | |
| 34 | Se | 5.96 | -01 | | | | 75 | Re | 9.59 | -01 | | | | |
| 35 | Br | 6.22 | -01 | | | | 76 | Os | 9.61 | -01 | 3.5 | -01 | | |
| 36 | Kr | 6.46 | -01 | 1.0 | -02 | | 77 | Ir | 9.62 | -01 | 3.0 | -01 | | |
| 37 | Rb | 6.69 | -01 | 1.0 | -02 | | 78 | Pt | 9.63 | -01 | 3.3 | -01 | | |
| 38 | Sr | 6.91 | -01 | | | | 79 | Au | 9.64 | -01 | 3.9 | -01 | | |
| 39 | Y | 7.11 | -01 | 3.2 | -02 | | 80 | Hg | 9.66 | -01 | 3.9 | -01 | | |
| 40 | Zr | 7.30 | -01 | | | | 81 | Tl | | | 4.6 | -01 | | |
| 41 | Nb | 7.48 | -01 | | | | 82 | Pb | 9.68 | -01 | 3.8 | -01 | 2.9 | -02 |
| 42 | Mo | 7.64 | -01 | 6.7 | -02 | | 83 | Bi | | | 4.1 | -01 | 3.6 | -02 |
| 43 | Tc | 7.79 | -01 | | | | 92 | U | 9.76 | -01 | 5.2 | -01 | 6 | -02 |
| 44 | Ru | 7.93 | -01 | | | | | | | | | | | |

**Figure 1.2**

Fluorescence Yields [Ba72]

Such detectors have considerably smaller solid angles than the lower resolution ($\geq$140 eV) Si-Li detectors, typically losing a factor of about 100. Also, conventional crystal spectrometers are not able to detect multiple x-ray lines simultaneously. Minimum concentrations detectable with the SEM are $\geq$ .1%, not quite sensitive enough to qualify as trace analysis.

### Proton Bombardment

Because the direct bremsstrahlung background is proportional to the inverse square of the mass of the incident particle, a proton or heavy ion probe will provide a much lower level of background. Typically this reduction is about a factor of 1000 below that of the electron microprobe, and is unimportant. The background reduction is limited by the bremsstrahlung contribution from secondary electrons created by the primary beam. A typical proton microprobe easily provides sensitivities of 1 ppm. for elements of $14 \leq Z \leq 40$.

The maximum cross-section for the ionization of an atom by protons is achieved when the speed of the proton approximately matches the classical orbital speed of the atomic electrons. The actual maximum yields beam energies in the range of 8-32 MeV for elements of $20 \leq Z \leq 40$. Generally, a proton energy of 2-4 MeV is used, since noise from nuclear gamma rays increases rapidly above 4 MeV. These energies are achievable by many small electrostatic accelerators.

For proton microprobes operating in vacuum, spatial resolution of less than 1 micron has been obtained[]. Some proton microprobes take the beam out into air through a thin window [Ho76]. This allows the analysis of many kinds of samples that are not easily prepared for vacuum analysis, such as hydrated organic specimens [Ho75].

### Photon Bombardment

The use of x-rays as a means of excitation has several advantages over the use of particle probes, and is the technique on which most of the work presented here is based. X-ray fluorescence [XRF] analysis requires that the specimen be bombarded with x-rays of sufficient energy to eject an inner shell electron from the trace element atoms. The cross-section for ionization of a particular atom displays a series of discontinuous jumps as a function of energy, an increase in the cross-section occurring whenever the

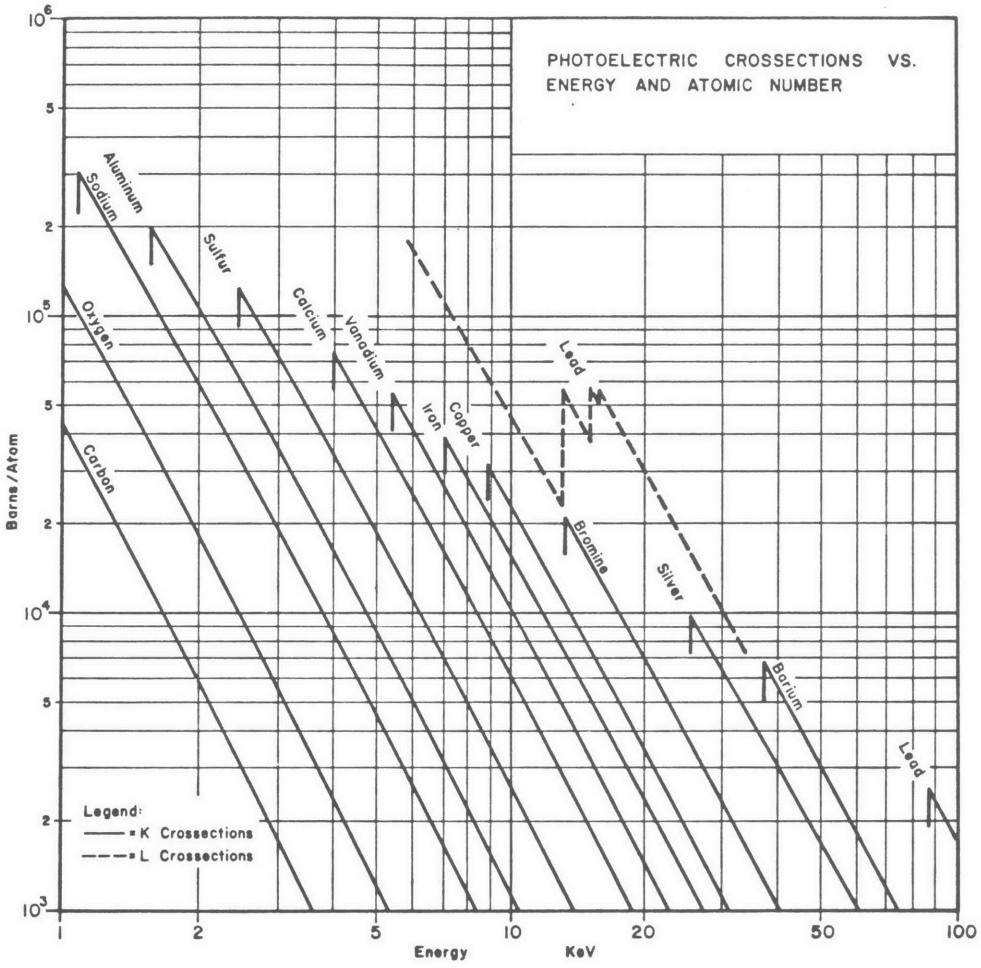


**Figure 1.3**

Ionization Cross-sections. [Wo75]

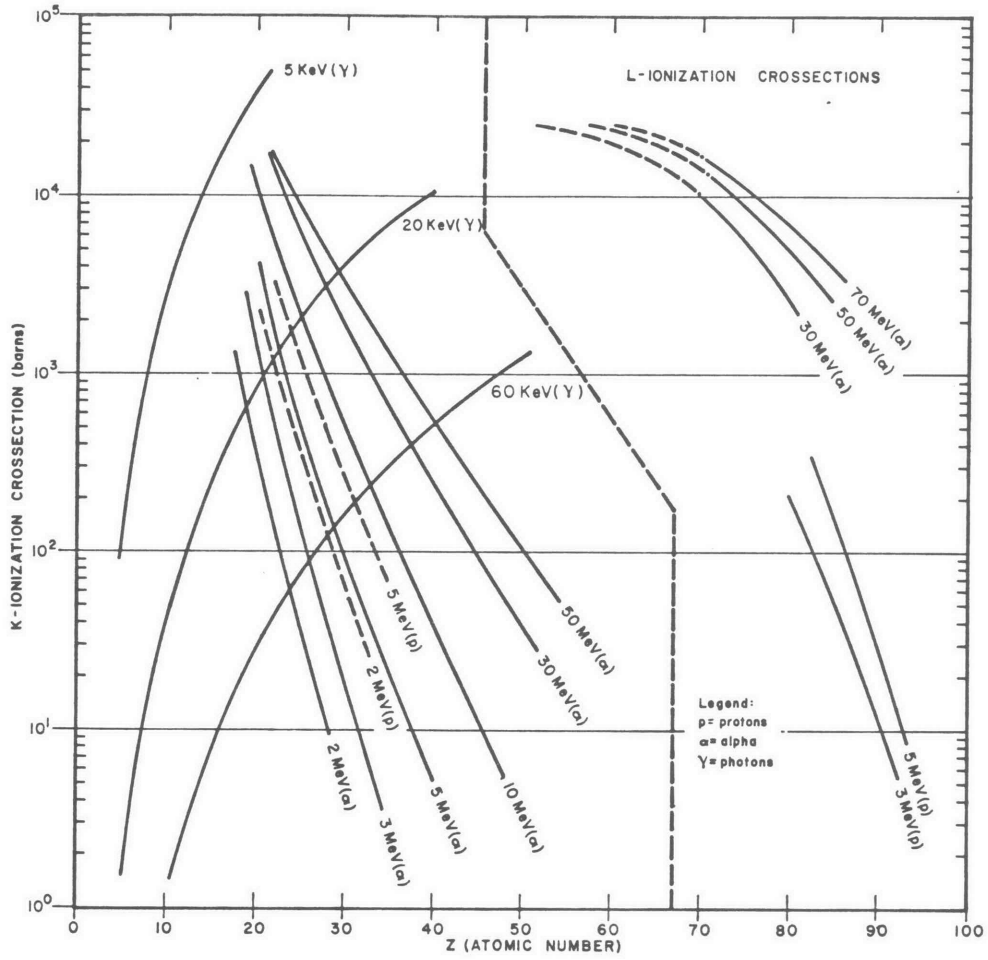


**Figure 1.4**

Comparison of charged particle and photon excitation for characteristic x-ray production. [Wo75]

bombarding energy exceeds each successive atomic energy level (Figure 1.6). X-ray emission cross-sections for an incident photon just above the K-edge of a particular target atom can exceed $10^4$ barns (Figure 1.3).

The cross-section discontinuity allows the possibility of tuning the incident photon beam to optimize the fluorescent signal from a particular trace element, while suppressing the signal from nearby higher-Z components. Very high sensitivity is possible if the incident beam is monochromatic, since the only source of continuum background is due to low energy secondary electrons. Extending the incident photon energy upward to increase total beam intensity will also create higher energy electrons, with a corresponding increase in background. The actual energy bandwidth used is a compromise between signal intensity and background. The signal due to elastic and inelastic scattering may be eliminated with sufficient energy discrimination in the detector.

The sensitivity of all of the above techniques is dependent on the total beam dose available. Given sufficient time, it might be expected that an arbitrary sensitivity could be achieved by increasing the analysis time. Aside from the practical considerations imposed by available beam intensities for each of the techniques, there is a limit due to the effects of the incident radiation. If trace elements are being evaporated due to surface heating, results will be inaccurate. In the case of spatially resolved analysis, displacement of the constituent atoms by distances comparable to the beam resolution will become an important effect.

These problems are much less important for XRF, since the energy imparted to the sample atoms is usually much lower than for electron or proton probes. The ultimately achievable sensitivity of XRF is therefore much higher than that of the other techniques (Figure 2.7). The real limitation is now the quality of available x-ray sources.

The recent development of dedicated synchrotron x-ray facilities, such as the National Synchrotron Light Source at Brookhaven, has made available x-ray beams several orders of magnitude more intense than were previously available. Through the use of tuneable monochrometers and x-ray focussing elements, it has become possible to create beam spots with densities exceeding $10^{10}$ photons/$\mu$m$^2$ in a 1% $\delta E/E$ and spatial dimensions of less than 30 microns. Newly proposed synchrotrons could yield flux densities 1000 time higher.

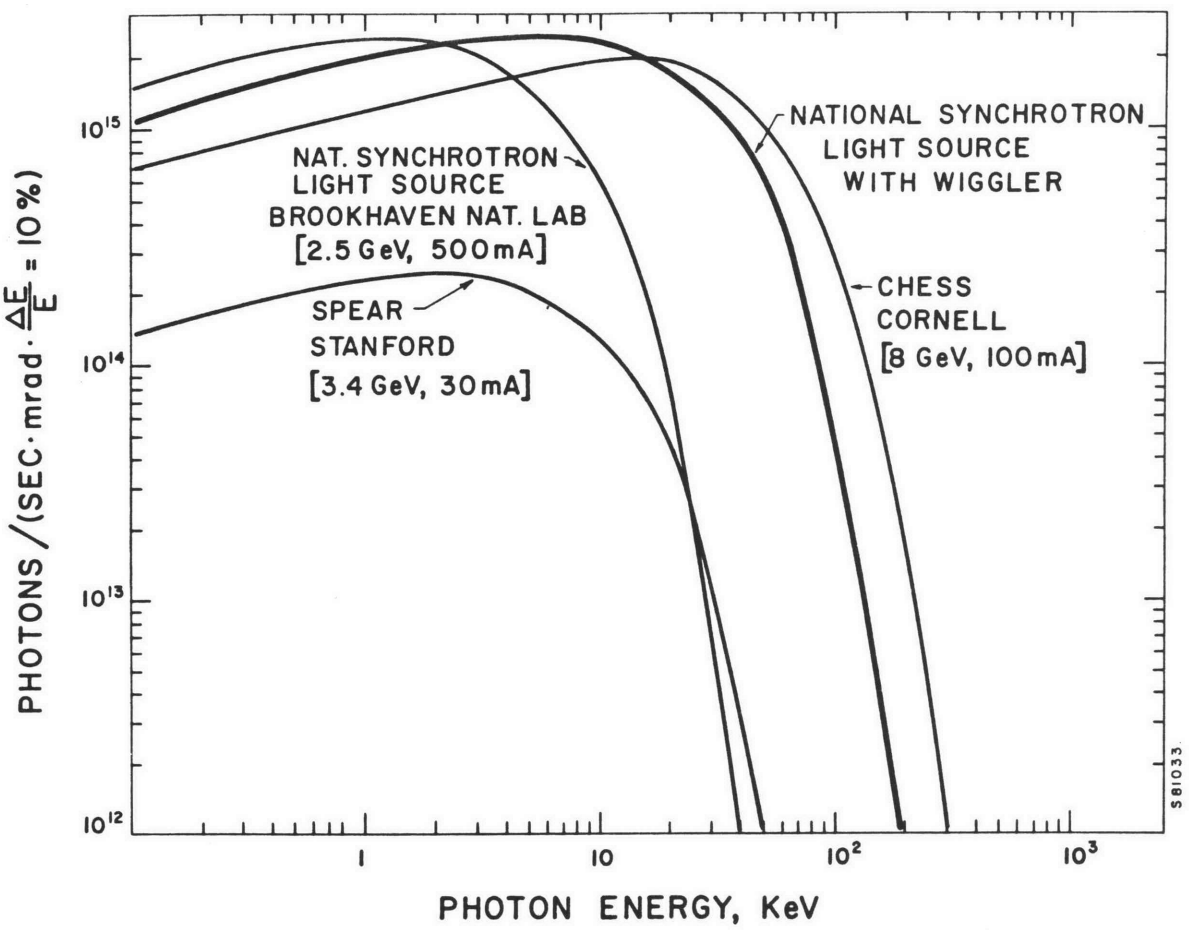


Figure 1.5

X-Ray Spectrum for the NSLS

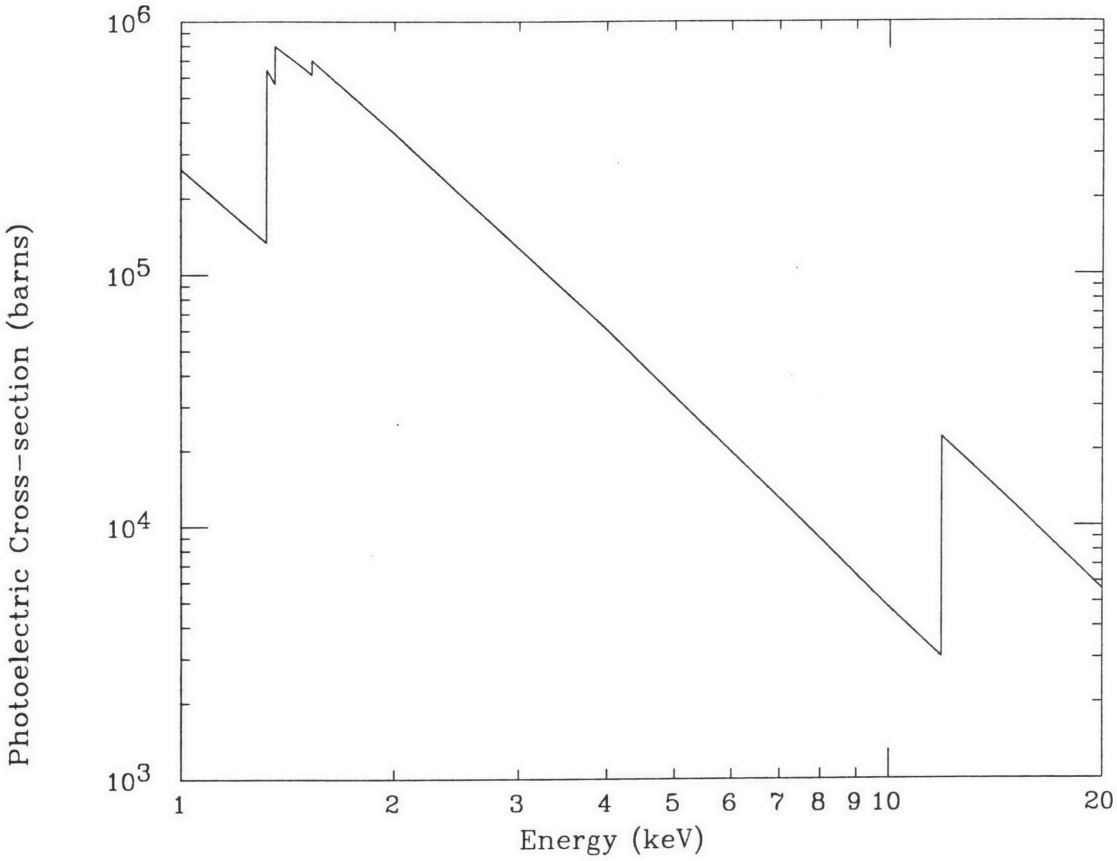


**Figure 1.6**
Photoelectric Cross-section for Arsenic

Our original intent was to develop the use of tomographic techniques for x-ray fluorescence analysis. The work was to be done on the microprobe beam line at the National Synchrotron Light Source at Brookhaven National Laboratory. This would first have involved the creation of an intense x-ray beam with spatial dimensions of less than 50 microns and a monochromaticity of better than 5 percent. Such a microbeam would allow spatially resolved elemental analysis with sensitivities below 100 parts per billion (ppb). A more complete description of the NSLS photon microprobe is given in Appendix A.

Tomographic analysis of elemental distributions requires the use of beams with small spatial dimensions. This is due to the nature of the technique. Such analysis requires x-ray beams in the range of 1-20 keV to induce characteristic x-rays from the trace elements that are to be mapped. This imposes a limit on the size of the specimen, since the incident beam must be able to penetrate the specimen without extreme attenuation. It is expected that the first real use of the technique will be for the analysis of metals in small ($\leq$ 1 mm) organic specimens, such as the larger cells of the human nervous system. Useful analyses of this type could be done with beams with spatial dimensions of $\leq 25\mu$m. If sufficiently intense beam spots $\leq 1\mu$m. in diameter are produced, analysis of silicon microstructures will become possible.

Calculations were made to determine ultimate detection limits of x-ray fluorescence with the synchrotron beam. Work was done both at MIT and Brookhaven on the focussing optics (Appendix A) and monochrometer design. As the NSLS x-ray ring fell more and more behind schedule, it was decided to search for possible ways of testing the main aspects of the XRF tomographic technique, such as the Ion–X-ray–X-ray (IXX) technique. In this way, it would be possible to take advantage of time on the NSLS if it became available. These investigations are outlined below.

## Synchrotron Tomography

The determination of trace element distributions in a specimen is usually restricted to a two dimensional analysis over a surface. Three dimensional information can sometimes be obtained by mechanically sectioning the specimen, but this is frequently difficult or impractical. The technique of Computer Assisted Tomography (CAT) can be used to determine internal structure under some circumstances. X-ray fluorescence can take advantage of tomographic techniques, providing a sensitive three dimensional determination of trace element distributions for suitable specimens.

A tomographic analysis of this type requires a monochromatic x-ray beam with a small spot size and low angular divergence. The spot size determines the spatial resolution of the technique; angular divergence must be small enough to prevent beam spreading over the distance necessary to traverse the specimen. In order to achieve part-per-million sensitivity, a very high photon flux is required. The availability of dedicated high-intensity synchrotron sources has made such beams possible.

The analysis proceeds by scanning the beam across the diameter of the specimen (Figure 1.7). At each position, fluorescent x-rays emitted along the incident beam path within the specimen are detected and recorded. The intensity of these x-rays is proportional to the concentration of the trace element integrated along the beam path. No attempt is made to determine where along the path the x-rays originated. The sample is rotated, and the lateral scan is repeated. For a sufficient number of rotation angles, the two dimensional distribution of the trace element can be determined mathematically. A collection of such two-dimensional slices can be built up to provide a three-dimensional view of the trace element distribution.

Synchrotron beams now becoming available should be able to provide detectability to the 1 ppm. level for spatial resolutions of 25 microns in a tomographic mode. This assumes an image grid of 100x100 picture elements (pixels) for the reconstructed image.

The NSLS facility was beginning to become operational at the time of this writing, and we were fortunate to arrange a collaboration with the ORNL group at the NSLS, headed by C.Sparks. and were able to perform some preliminary tests of synchrotron tomography. The ORNL beam line was able to produce a beam which, although developed for other purposes, was suitable for preliminary tests of synchrotron fluorescence tomography. A set of experiments were done, and the results are presented in Chapter 2.

## IXX

Although no x-ray source matches the flux density of the synchrotron, some tests could be done with any source of relatively monochromatic x-rays. Our previous work with proton induced x-ray emission analysis suggested the use of ion induced characteristic x-rays as a low background source. The use of such a source for bulk

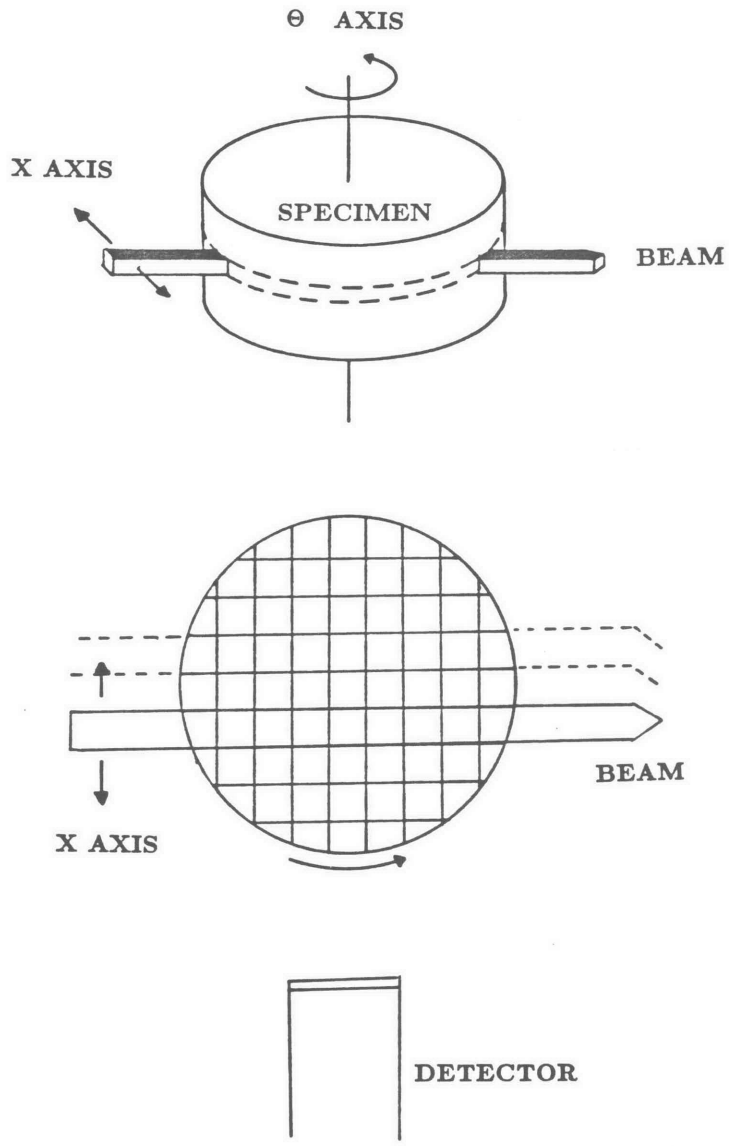


**Figure 1.7**
**Synchrotron Tomography**

The tomographic analysis of a cylindrical object. The analysis wil determine the trace element distribution over a single slice of the object. The synchrotron beam is scanned across the slice while induced x-rays are counted at each position. After the slice diameter has been traversed, the sample is rotated about its axis and the lateral beam scan is repeated. After a full sequence of rotations, enough information is obtained to allow the determination of the concentrations at all grid points.

analysis was investigated and found to be a useful technique in its own right [Gr83b]. The results of this research is covered in Appendix B.

### Optical Tomography

The usefulness of tomographic techniques in non-medical applications has been widely recognized [To78], and we were able to apply the technique to the optical analysis of intense ion beams used in ion implantation work. A visible image of the ion beam is produced by the interaction of the beam with the residual gas in the vacuum chamber. Tomographic analysis of the visible image allows beam profiles to be determined without affecting the beam or contaminating the process. The design of this system and its results are presented in Chapter 3.

### Scanning Rutherford Backscattering

While this work was progressing, we became interested in testing the results of this ion implantation process. This led to to development of a scanning Rutherford Backscattering Spectroscopy technique. RBS analysis is used to provide depth distribution of dopants in silicon wafers. The ability to scan a full silicon wafer under computer control to provide spatially resolved RBS provides a very convenient means of determining total dose uniformity, as well as depth uniformity.A review of this work is included as Appendix C.

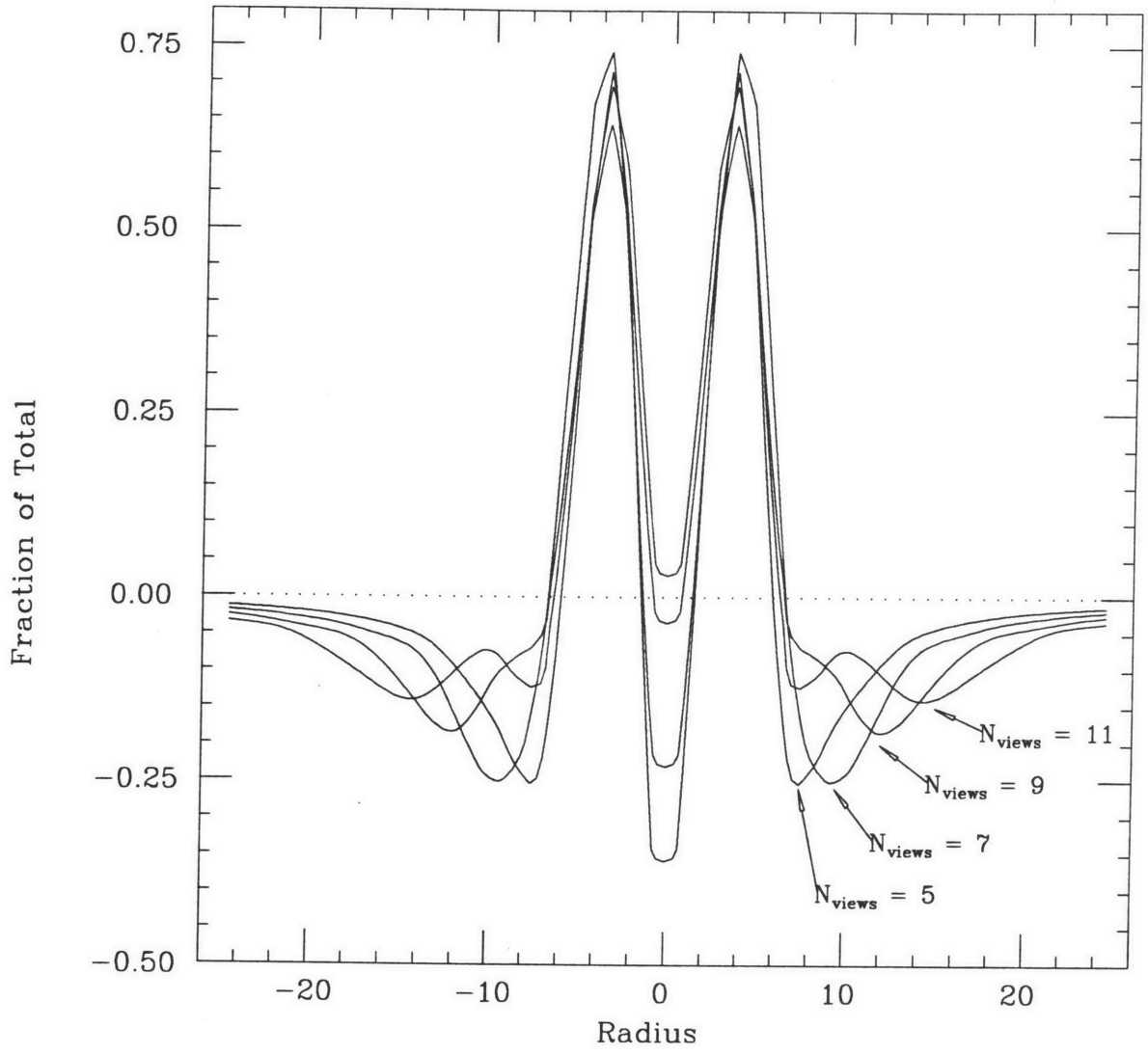
0.75
0.50
0.25
0.00
−0.25
−0.50
Fraction of Total
−20
−10
0
10
20
Radius
N views = 11
N views = 9
N views = 7
N views = 5

# CHAPTER 2
## Tomographic Reconstruction

The wide range of techniques used for material analysis is a consequence of the extreme diversity in the types of questions that are asked. A particular problem might require the analysis of bulk properties or microscopic structure. It might require the stoichiometry of major components or trace element analysis to the level of one part in a billion. The sample might be a gas, a thin film, or a complex biological structure. It is frequently desirable to obtain information about the spatial variation of a particular property of the specimen. We will be concerned with those techniques which are capable of providing spatial information.

Many techniques used for material analysis are capable of providing information on the spatial variation of the physical characteristic which they measure. These imaging techniques include all forms of microscopy such as optical, electron, ion, and x-ray microscopy. Also capable of providing spatial information are techniques such as such as SIMS, Rutherford Backscattering Spectroscopy, etc. These kinds of analysis are frequently limited to two dimensional information - they examine the sample surface. Conventional analysis does not usually provide three dimensional information directly. In some instances, the use of tomographic techniques allows the internal structure of samples to be determined without physically dissecting the specimen.

The most common tomographic application, medical x-ray transmission tomography, determines internal density variations by measuring the attenuation of high energy ($\approx$ 150 KeV) x-rays through the body. Positron emission tomography maps the distribution of injected radioisotopes by detecting positron-electron pairs. Optical emission tomography will determine the luminosity distribution in a transparent incandescent source. An application of this technique is developed in Chapter 3. Other probes, providing a range of information, have been used and continue to be developed. The development of x-ray fluorescence tomography for trace element analysis will be described in Chapter 2.

In order to describe the general characteristics of tomographic analysis, we consider as an example an extended source of visible light with negligible self-attenuation (Figure 2.1). This might represent a flame, a gas discharge, or a particle beam - gas

interaction. We wish to determine the luminosity of any small volume element of the source by measuring the light emission from the entire source.

Since a three dimensional distribution of the intensity may be built up from a stack of 'slices' through the source, it is only necessary to determine the two-dimensional distribution of intensity over an arbitrary slice through the object. One such slice is shown in Figure 2.2. We divide the slice into a grid of discrete points with the required spatial resolution. In this example, we have divided the slice into 10x10=100 spatial points. We now must determine the values at each point of the grid.

The light emission from the object is measured by means of a camera made up of a lens and a one dimensional photodiode array. The camera is focussed to project an image of the luminous object onto the sensor array. It is assumed that the camera is far away compared to the total size of the object, so that distortion is negligible and all image rays are approximately parallel. Consider the line passing through a point on the photodiode array and the optical center of the lens. The image intensity at that point of the photodiode array is proportional to the sum of the luminosities contributed by all object volume elements also lying on the line. For the assumed 10 element photodiode array, a single measurement obtains the projection of the intensity distribution along one axis. If we consider the array values to be a set of 100 unknown quantities, we now have 10 equations in 100 unknowns. These are simply the following:

$$P_1 = \sum_{y=0}^{10} I(1,y)$$

$$P_2 = \sum_{y=0}^{10} I(2,y)$$

$$P_3 = \sum_{y=0}^{10} I(3,y)$$

$$\vdots$$

$$P_{10} = \sum_{y=0}^{10} I(10,y)$$

where $I(x,y)$ is the intensity of the object grid point at coordinate $x,y$. 90 more independent equations must be generated in order to solve for all 100 unknown intensities.

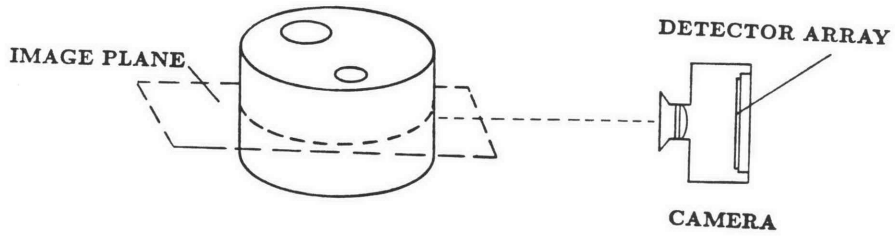


**Figure 2.1**

Geometry of Optical Tomography. The cylindrical object represents a luminous specimen. The intensity distribution across the plane indicated may be determined tomographically.

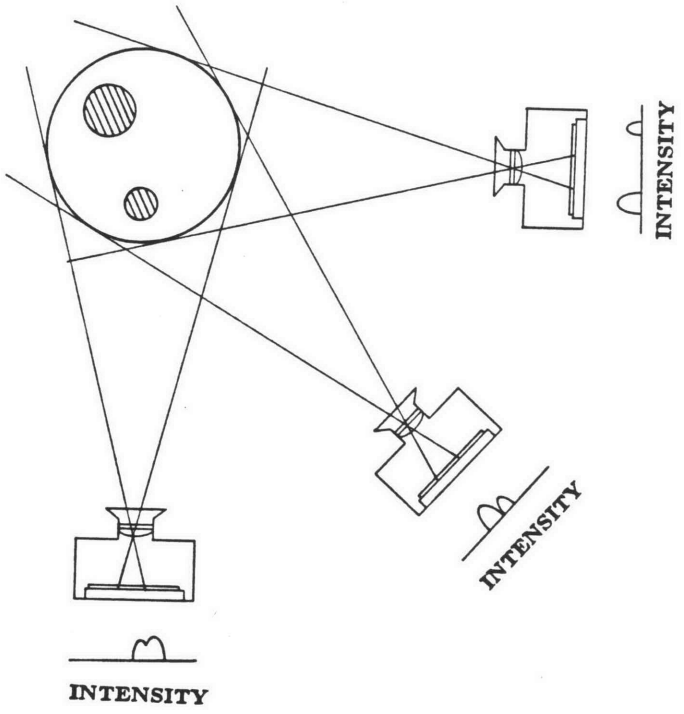


**Figure 2.2**

View in the analysis plane. A one dimensional image is formed by the camera at each of several angular positions. Each image measures the projection of the intensity distribution along a single axis. A complete set of such images will allow the reconstruction of the original object

A new set of projections is generated when the object is rotated about its center by some angle $\theta$. In this case, it is reasonable to assume that a set of 10 rotations equally spaced through 180° might be sufficient to determine all 100 unknowns, since this would provide a total of 100 equations. It will be shown that this estimate is actually low by a factor of $\pi/2$. This indicates that, in order to provide a reasonable reconstruction of a 10x10 array, a series of at least 15 angular views is needed, each with a spatial resolution of less than 1/10 of the sample diameter.

Once we have determined a sufficient set of projection values, the task of solving the set of equations remains. One possibility is to solve the problem analytically; for the 10x10 cell reconstruction being considered, this would require the inversion of a 100x100 matrix. Although such an approach might seem reasonable in this case, a more typical reconstruction might involve a 500x500 pixel image array, requiring the inversion of a 250000x250000 matrix. In addition, it has been asssumed that the projection data is perfect, *i.e.* that it contains no noise. When noise is present, the matrix cannot be inverted since the noisy projections do not correspond to a unique solution. A proper reconstruction should in some sense describe the 'best fit' to the projection data. In general, an analytical solution is not considered; instead an approximate solution is found by one of several methods. The methods differ in their complexity, speed, ability to deal with sparse data, and sensitivity to noise. We will review some of the more commonly used methods below.

## RECONSTRUCTION TECHNIQUES

The multiple one-dimensional angular views may be converted to a plane image through any of several reconstruction methods [Bu78]. The three most common techniques are:

1) Algebraic Reconstruction Technique (ART)
2) Filtered Back Projection (FBP)
3) The Method of Fourier Transforms (FT)

A new technique which has been applied to reconstruction problems recently is:

4) Maximum Entropy (ME)

## ALGEBRAIC RECONSTRUCTION

ART is an iterative process made up of three steps (Figure 2.3):

1) An trial image matrix, initially blank, is projected in the directions corresponding to the available projection data. We now have a set of trial projections, and the set of real data. For the first iteration, all trial projections are zero for all points.

2) For each angle in turn, the pair of one-dimensional projection arrays are compared, and the difference between them is calculated point by point. This error matrix is then projected back across the image matrix after proper normalization. This insures that the image projection at that angle now agrees with the real data. This agreement is short-lived, since the next angle correction will change the image data.

3) The image matrix now contains the first approximation to the final image. Steps (1) and (2) are now repeated. The image matrix should continue to improve as the error matrices decrease in magnitude. Clearly, if the image acquires values which are consistent with the real projection data, the error matrices will be zero and no further change will take place.

In general the data will not be perfect and so the iteration could be continued indefinitely. There is a problem with the technique, however. The image will usually slowly converge to an optimum solution and then it will start to diverge, especially if the data contains noise. For this reason, care must be taken to stop the iteration at the proper point.

ART is conceptually simple, and is particularly effective for situations where a complete set of angular projection are not available. However, the calculation is slow, and data at all angles must be available from the beginning of the procedure. Other techniques act on one projection at a time, allowing data collection and calculation to be done simultaneously.

## FILTERED BACK PROJECTION

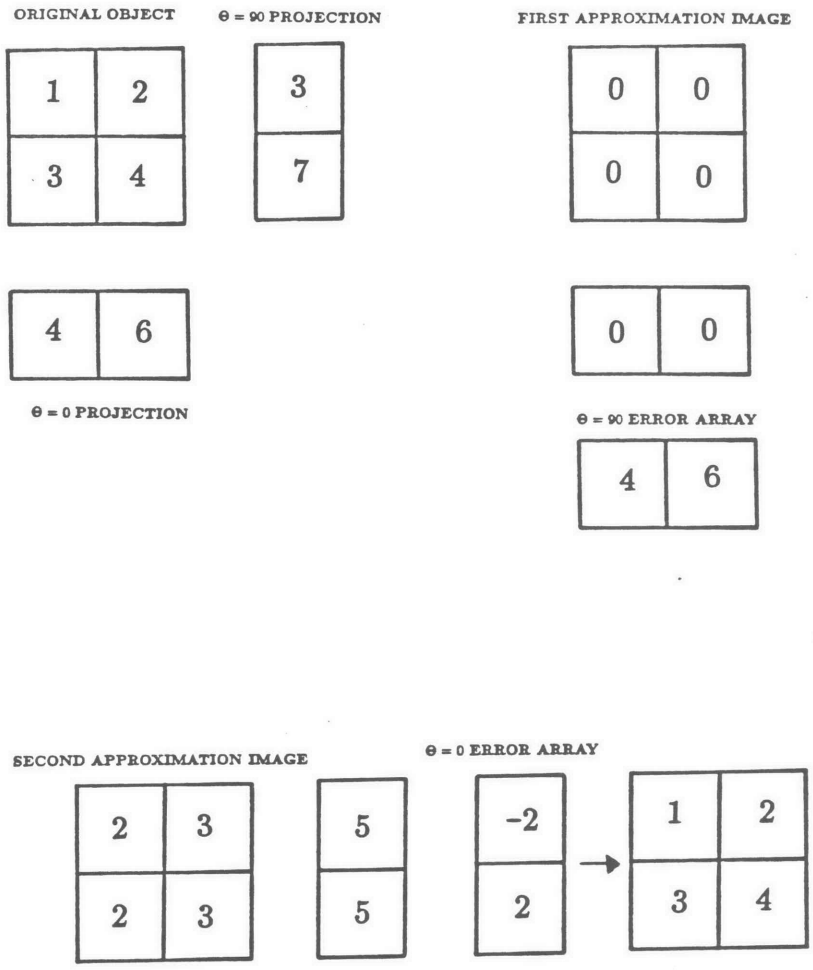


**Figure 2.3**

Algebraic Reconstruction Technique. Here, a 2x2 image (top left) will be reconstructed from its projections along two axes ($\Theta$=0 and $\Theta$=90) A blank matrix is used as a first approximation to the image. The projections of the trial image are compared to the true projections, and the resulting error array is divided by 2 and added back to the trial iamge. The process is repeated for the second axis, yielding the original image. For larger arrays, projections are taken along a range of angles, and the process is iterated.

Back projection was the first method used for the reconstruction of a tomographic image. An image is built up by projecting each data array across an initially blank two-dimensional image matrix, and summing the contributions. Each projection is done at the angle at which the data was collected.

Since any object can be represented by a superposition of point objects, obtaining a clear reconstruction of a point image is all that is needed. The Figure 2.4 demonstrates the results of this method assuming a point object centered in the field of view. Each data projection is similar, consisting of a single central point. One projection array is back-projected in Figure 2.4b. The result is a narrow stripe across the image array. As subsequent back-projections are added, a star-shaped image is produced with a large central value. In the limit of infinite resolution and an infinite number of angular projections, the resulting shape is a 1/r cusp (Figure 2.4d). An arbitrary original object would reconstruct to a blurred image. A modification of the method is clearly necessary.

If the projections for a point object are to sum to zero outside of the central region, there must be some negative components to the arrays before they are back-projected. It can be shown that the original data arrays must be convolved with a filter function of the form:

$$F = \begin{cases} 4, & |x| < 1/2 \\ -1/x^2, & |x| > 1/2 \end{cases} \tag{2.1}$$

shown in Figure 2.4d. This filter function will result in projection arrays which contain a positive pulse and negative side lobes as shown. When these filtered projections are back-projected across the image array, the central pulses add constructively. Any point outside of the intersection region receives both positive and negative contributions which sum to zero. This last property follows from the fact that the integral of the filter function is zero. Although there is theoretical justification for the above filter function, other filter functions may be selected for purposes of edge enhancement, smoothing, etc.

The algorithm for filtered back projection has the advantage that data can be filtered and back-projected one angle at a time, therefore the system can be calculating the partial solution while waiting for additional data to become available. The

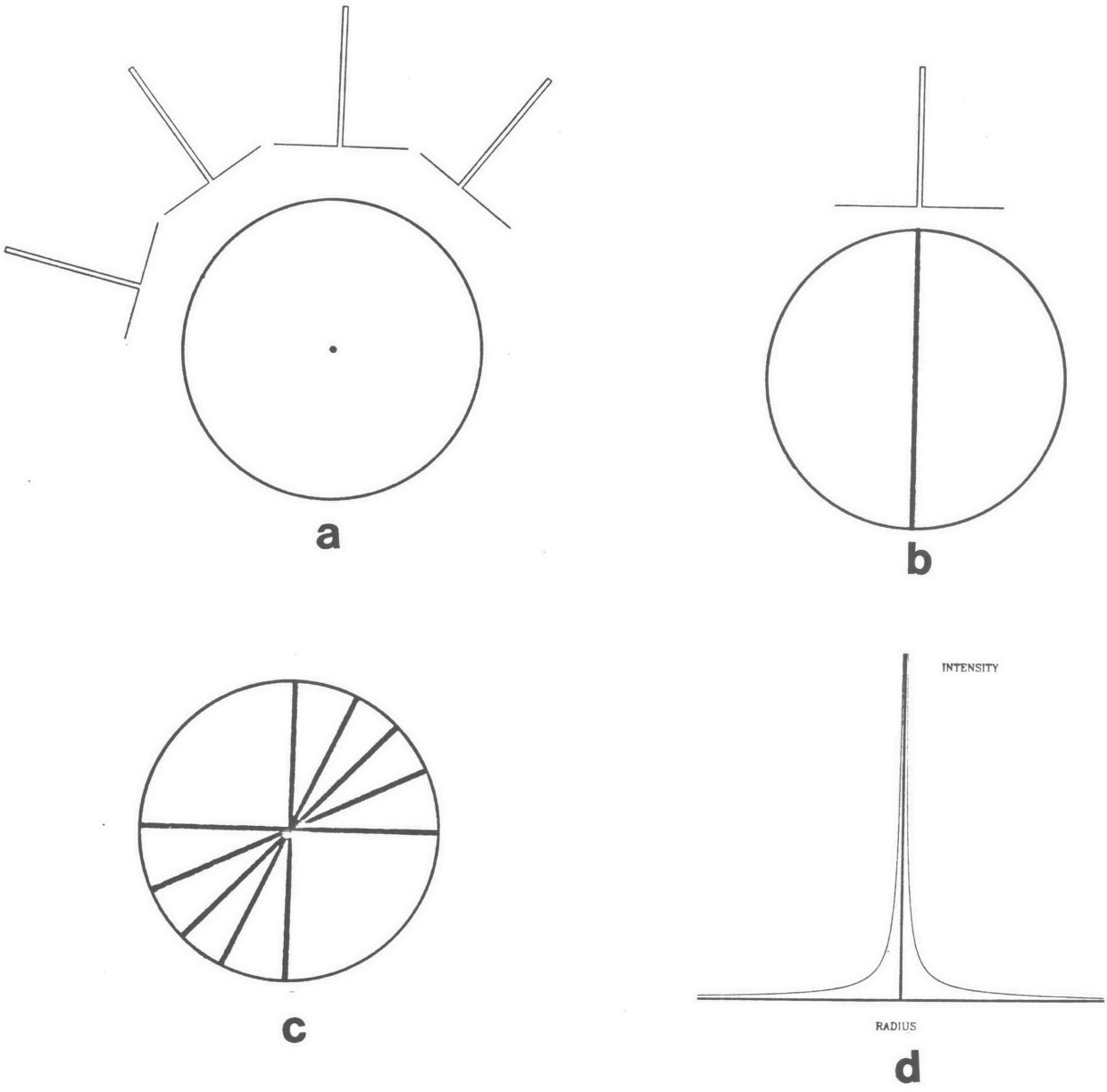


**Figure 2.4**

Back Projection. Figure (a) represents a central point object projected on to four axes. When a single projection is projected back across a blank image figure (b) results. In the limit of a large number of angles, the result of projection/back-projection is a 1/r blur (d)

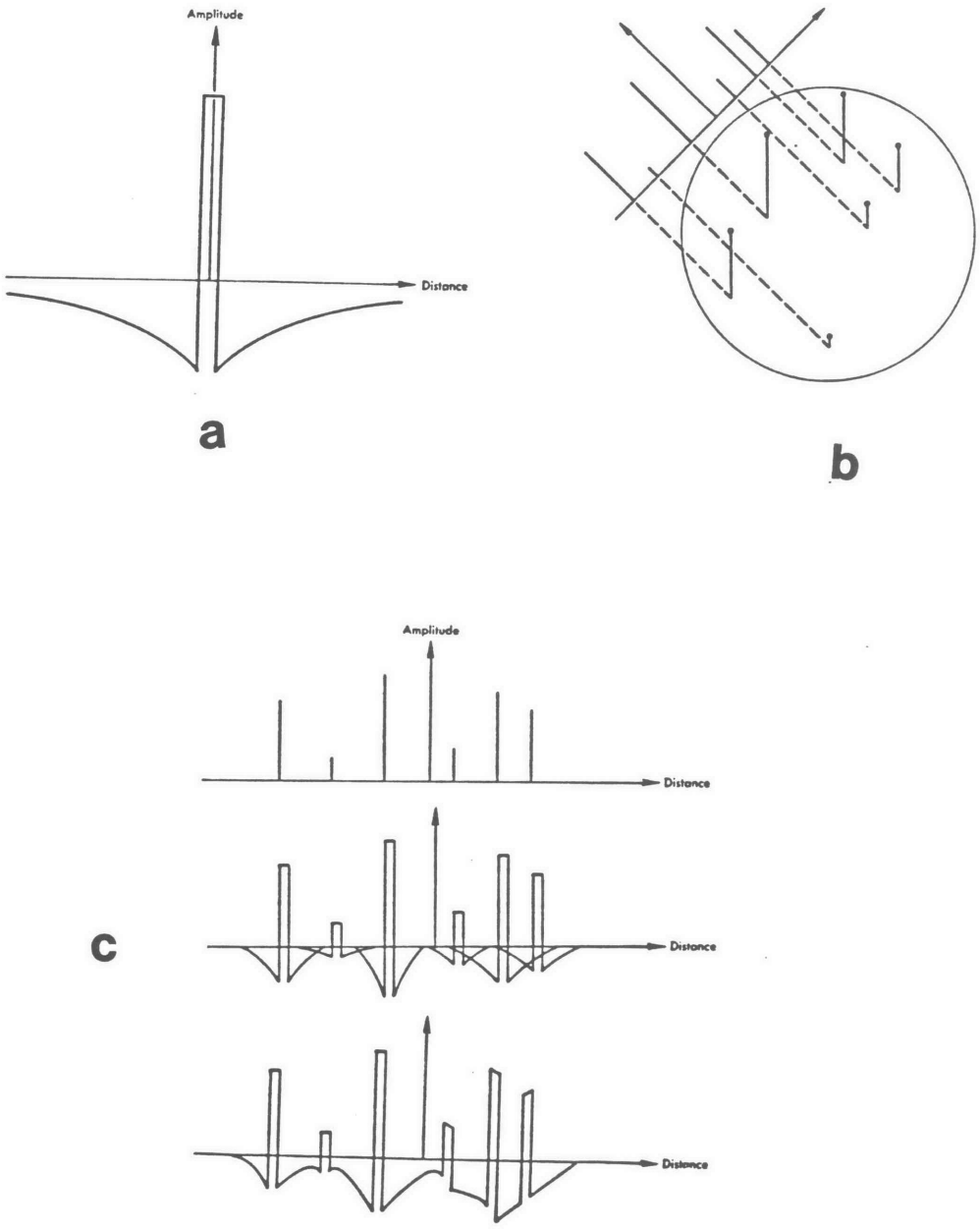


**Figure 2.5**

Filtered Back Projection. Figure (a) shows the convolution function used for filtered back projection. An arbitrary projection (b) is convolved with the filter function and the resulting projection shown in (c).

algorithm is quick and relatively simple, and is the method used for the experimental results presented in the next chapter.

## FOURIER RECONSTRUCTION

The Fourier Transform method of reconstruction is not as conceptually simple as the methods described previously. The Fast Fourier Transform algorithm is used to do in frequency terms what filtered back projection does in spatial terms. Instead of summing projections in image space, the Fourier Transforms of the projections are calculated, and these one-dimensional transforms are back-projected to form a two-dimensional frequency distribution. Particular frequency cutoff functions serve the purpose of the particular FBP filter functions. A two-dimensional inverse Fourier Transform of the frequency distribution produces the final image.

Although somewhat more mathematically sophisticated than the previous methods, the Fourier technique is quite fast. Image quality is similar to that of Filtered Back Projection.

## MAXIMUM ENTROPY

A relatively new technique developed for certain intractable problems [Ki83] has been applied recently to the problem of image reconstruction. This method borrows from the formalism of statistical mechanics to search for a solution to a multiparameter fitting problem, which the problem of image reconstruction may be considered to be.

Given a set of N parameters which are to be varied in order to minimize some error function, several general methods are available. The most straightforward is to try all combinations of all possible parameter values. If there are more than a very small number of parameters, this method is far too slow. In the case of ten variables each with a range of only ten values, $10^{10}$ evaluations of the error function are necessary.

A more practical method optimizes one parameter at a time, and iterates through the parameter list until a minimum in the error function is found. This works if the parameters are reasonably independent, and there are no relative minima in the error function. Unfortunately, many real problems are not well behaved, and the error space is littered with spurious minima.

Most conventional searches rely on the change in an error function to determine the direction of parameter changes. If a given parameter change reduces the value of the error function, the changed parameter set is accepted as the starting point for the next step in the search. If the error function is increased, the parameter change is discarded. The ME technique differs in this respect. Here, a parameter change yielding an improved fit is still kept, but one which gives a worse fit may also be accepted with a probability given by a weighting factor of the form $\exp(-p/T)$ where p is the change in the error function for the new parameter set. For large T, a poor change in the parameter set will be accepted with high probability as long as it is less than 1/T in magnitude. For small T, the search will act more like a conventional method, with bad parameter changes being rejected.

The technique begins with an initial parameter set and a large value of the parameter T. Random variations are made in the parameter set; these random variation may be accepted or rejected according to the above criterion. After some number of variation steps, the parameter T is reduced in value, and the procedure is repeated. Eventually the problem converges to a solution at low T. The rate at which T is reduced - the 'annealing schedule', must be determined for a particular set of problems. This method has been used for tomographic reconstruction by varying image pixel values and comparing the resulting image with the experimental data.

## NOISE IN RECONSTRUCTED IMAGES

The nature of the tomographic reconstruction process must be considered when predicting the minimum limits on the detectability of trace elements in a matrix. With conventional X-ray fluorescence, this calculation is reasonably straightforward. We will briefly outline noise considerations for conventional x-ray fluorescence, then describe the limits imposed by the reconstruction process itself.

Three sources of noise must be considered for X-ray fluorescence:

1) Elastic scattering from the incident beam

2) Inelastic scattering from the incident beam

3) Detector noise

Figure 2.6 shows a typical spectrum produced from the analysis of iron distribution in an organic specimen using a Si-Li detector with a resolution of 240 eV. Because the K edge of iron is at 7.1 keV, the fluorescence cross-section is at a maximum for an incident beam energy just above that value. An energy somewhat higher, 7.2 keV is used so that the elastically scattered beam is separated from the iron x-ray line at 6.4 keV. The inelastically scattered beam appears as a broadening of the elastic peak. The signal from scattering of the incident beam provides the primary source of background in a measurement of the iron signal. It is found that Si-Li detectors produce a uniform background which extends down from each peak in a spectrum, and which contains 3-5% of the peak intensity. For this reason, the background from the elastically and inelastically scattered peaks is greater than would be predicted from the detector resolution and peak spacing.

A minimally detectable quantity may defined as that concentration of material which yields a signal just equal to the fluctuations in the background signal for a given detector. Since we are considering an x-ray counting technique, this may be expressed in terms of the signal count rate $S$, the noise count rate $B$, and the counting time $t$. Since the standard deviation of a count $n$ is $n^{1/2}$, we have the condition:

$$St = (Bt)^{1/2}$$
$$S = (B/t)^{1/2}$$

The required signal count rate, and therefore the required elemental concentration, decreases as $1/t^{1/2}$ for a fixed background count rate. Given a sufficiently long counting time, any arbitrary concentration could be seen. Different techniques can be compared if analysis time is assumed fixed, and typical incident fluxes are used.

A minimum concentration not explicitly dependent on counting time can be derived from the condition that the signal count rate equal the background count rate. Although the concentration thus derived is not a true minimum, the result is useful for comparing different techniques, since the result is not dependent on counting times or beam flux, but only on background count rates. Since background signal is a smooth function of energy, the signal to background ratio is optimized by the use of a detector with a resolution equal to the x-ray line width. This limit can be approached with the use of crystal spectrometers.

A comparison of charged particle and photon-induced x-ray fluorescence sensitivity is shown in Figure 2.7. Three assumptions have been made:

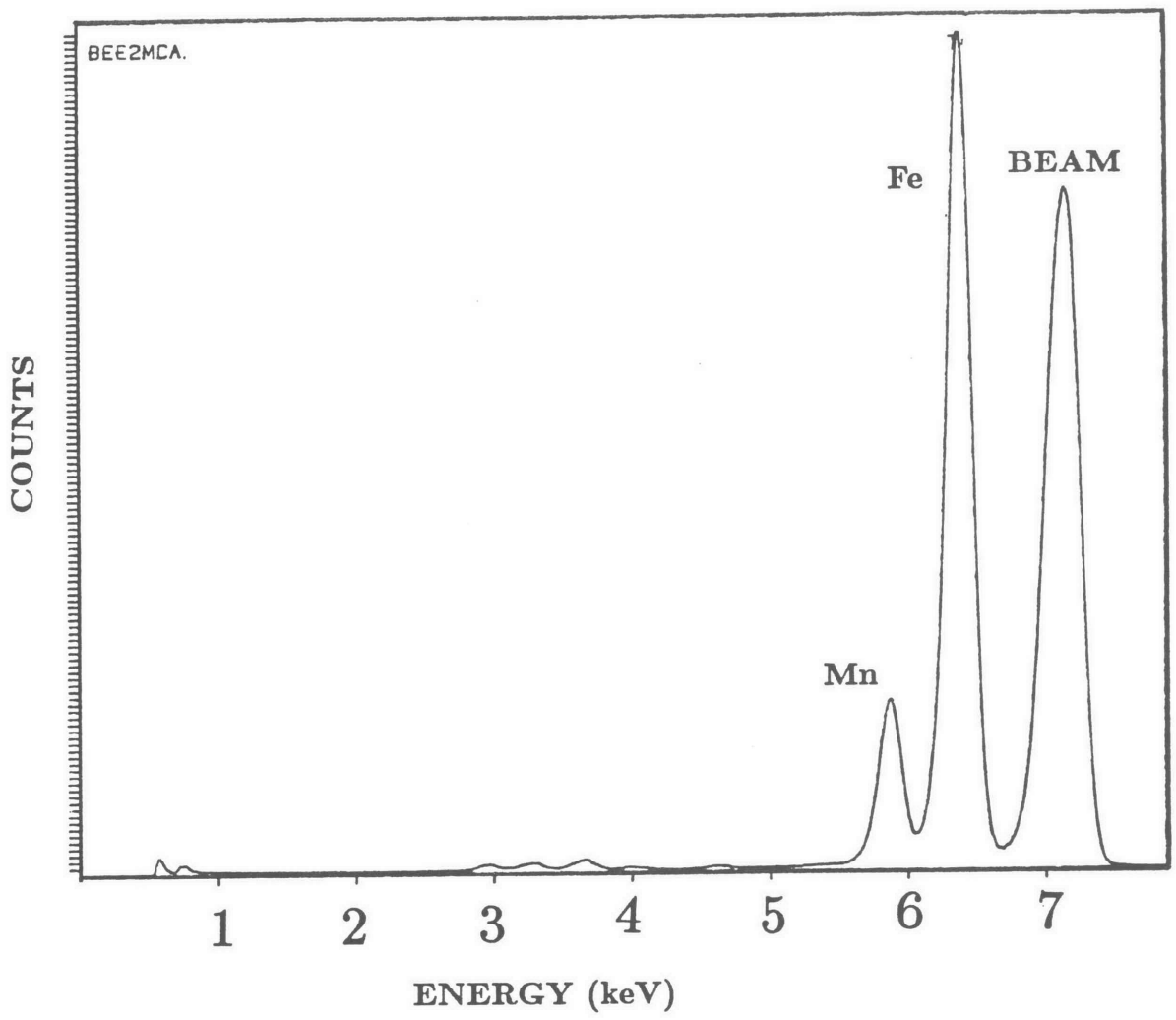


**Figure 2.6**

Fluorescence Spectrum: Iron in Carbon Matrix The spectrum of a honeybee with a 7.2 keV beam incident. The broad high energy peak is due to elastic and inelastic scattering of the incident beam by the organic matrix. A manganese peak is seen below the iron peak.

1) The signal intensity is equal to the background generated by secondary electrons in the matrix.

2) The incident projectile parameters have been optimized for the best signal to noise ratio.

3) The detector has a resolution equal to the line width of the induced x-ray.

Although the detectability limits for trace elements can be determined from background considerations, other effects must be considered when an image is to be produced tomographically. For images created by a conventional two-dimensional surface scanning technique, the statistical fluctuation in an image element containing $N$ counts is $\sqrt{N}$. The statistical significance of a high count pixel is determined by comparison to the value of $\sqrt{N}$. When the image is created tomographically, this simple statistical statement no longer holds.

We will examine the effect of the reconstruction process by considering the case in which the background is small compared with the statistical $(N)^{1/2}$ uncertainty of the signal itself. It is assumed that the collected counts represent a real signal. The analysis assumes the use of the Filtered Back Projection method of reconstruction.

A slice of thickness $w$ through an object of diameter $D$ is shown in Figure 2.8. An trace inclusion of iron is concentrated in a volume of dimension $w^3$ at its center. Let the incident photon beam be square in cross-section, with a height and width of $w$, and negligible divergence. We will consider the object to be divided into an array of volume elements (pixels) of size $w^3$. A tomographic analysis on this grid would require $v = D/w$ angular projections, each with a spatial resolution of $w$. The beam must therefore be scanned to $D/w$ positions at each angular orientation. Here we have used the approximation that reconstruction of an $v \times v$ matrix requires $v$ projections each with $v$ values; this is correct to about a factor of 2.

The data collection proceeds by scanning the synchrotron beam in equally spaced steps across the specimen. At each step, the beam will induce x-ray emission from all pixels along the beam path. Some fraction of these induced x-rays will be detected. Any x-rays within the energy limits set for the particular trace element of interest will

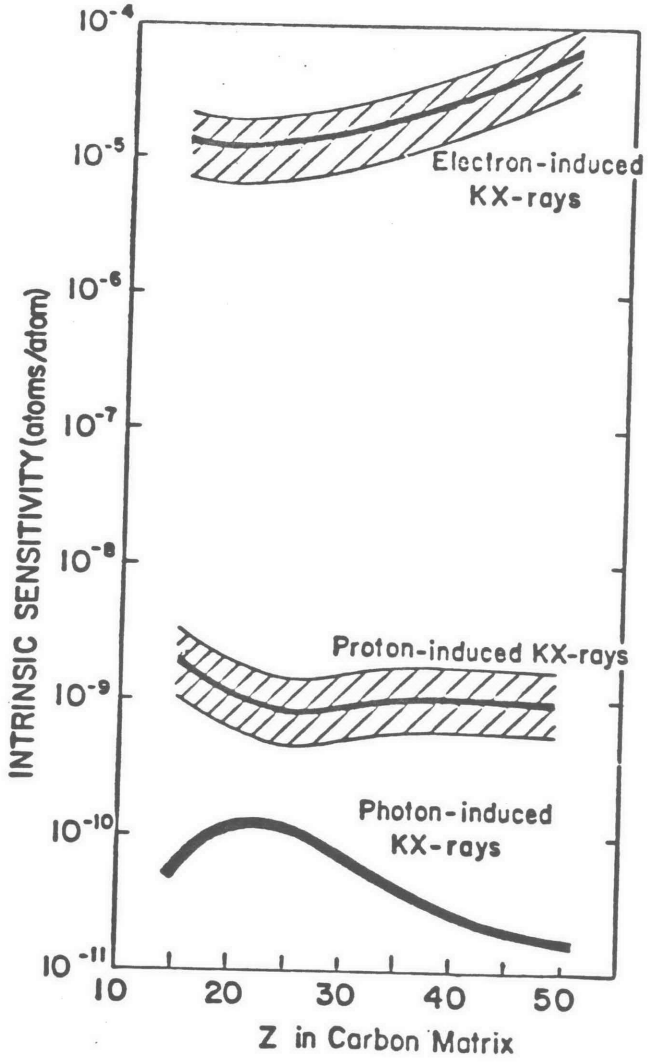


**Figure 2.7**

The intrinsic sensitivity as a function of the sought-for trace element in a carbon matrix for three techniques of x-ray fluorescence analysis using: Upper curve, electrons of from 50 to 100 keV; middle curve, protons from .4 to about 2 MeV; lower curve, photons whose energy is 1% above the binding energy of the K electrons of the sought-for species. [Gr83]

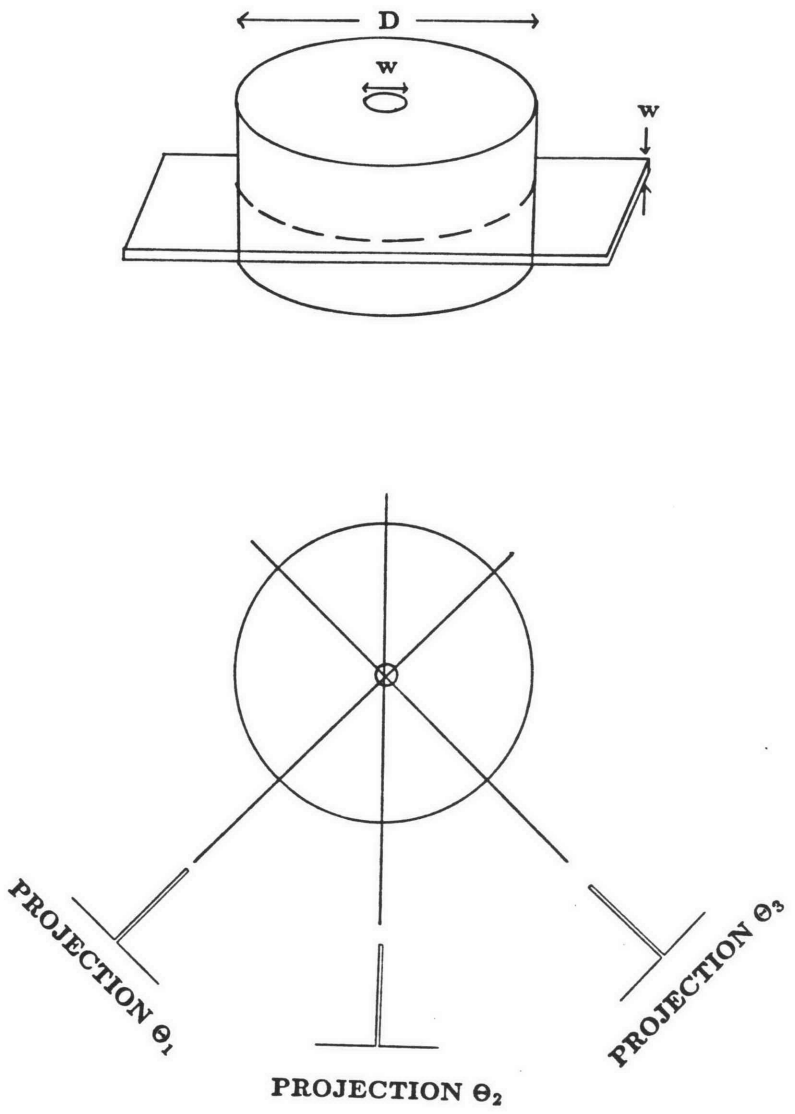


**Figure 2.8**

Tomographic Analysis of Single Inclusion. The reconstruction of an object with a single, central nonzero value results in a set of indentical projections (bottom). If the original measurement contains a noise component, the reconstruction process will add that noise to the entire image.

be counted and stored. In the case of the present specimen, some number ($n$) counts will be collected at that beam position which passes through the central pixel, and zero counts elsewhere (Figure 2.8). When the lateral scan is complete, an array of $v$ projection values will have been determined. This array is stored, and the specimen is rotated through an angle of $\pi/v$. A new data set is collected at this angle, and for all angles up to $\theta = \pi$. The data collection will thus yield a set of similar projections each with a value of $n \pm \sqrt{n}$ counts in the central position, and zero elsewhere. The $v$ projections are then convolved with the filter function, then each filtered projection array is back-projected across an initially blank image matrix, each at the angle corresponding to its collection angle. As the filtered projections are superimposed on the image matrix, the central image pixel will accumulate a total count of approximately $N = nv$. Points outside the central pixel will receive a positive contribution from one projection, and negative contributions from all others. The resulting for image positions corresponding to a zero value in the original object is an avaerage value of zero. However, although the *average* value of the 'outside' pixels is zero, there is a fluctuation about zero. We will show that this results from the statistical fluctuation in the counts originating from the single central pixel.

The final reconstruction produces a value of **N** counts in the central point, made up of a superposition of **v** views each contributing **N/v** counts. The standard deviation of the contribution of a single view is thus $\sqrt{\mathbf{N/v}}$. For any other pixel, the value of **N/v** will be added once, leaving a net average result of zero. The deviation from zero will be the sum of the deviations from the positive and negetive values:

$$\delta = \sqrt{2N/v}$$

Image positions which contributed no signal therefore have a variation in value which is $2\sqrt{1/v}$ times the noise fluctuation in the single central pixel. The results of computer simulations of point image reconstruction with statistical noise are shown in Figures 2.9-2.10

If the counts come from an extended source instead of a single pixel, we may sum the noise contributions from each contributing pixel in order to determine the effect on a non-contributing pixel:

$$\sigma^2 = 2(\frac{N_1}{v} + \frac{N_2}{v} + \frac{N_3}{v} ....)$$

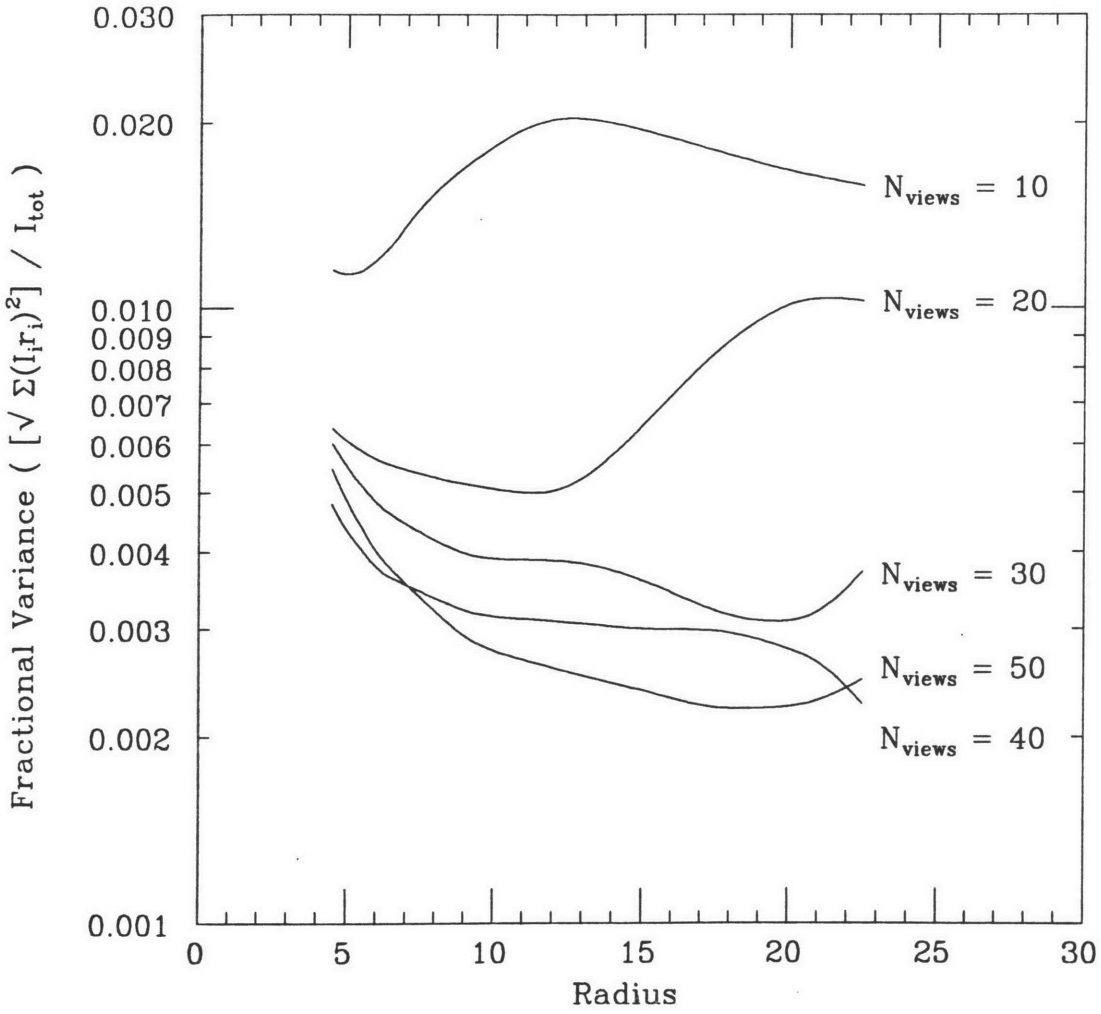


**Figure 2.9**

Statistical fluctuation in non-central points for specimen with single central inclusion. Data is shown for several values of angular resolution. Fluctuation is expressed as a fraction of central reconstructed amplitude, which is held constant at 1000 counts

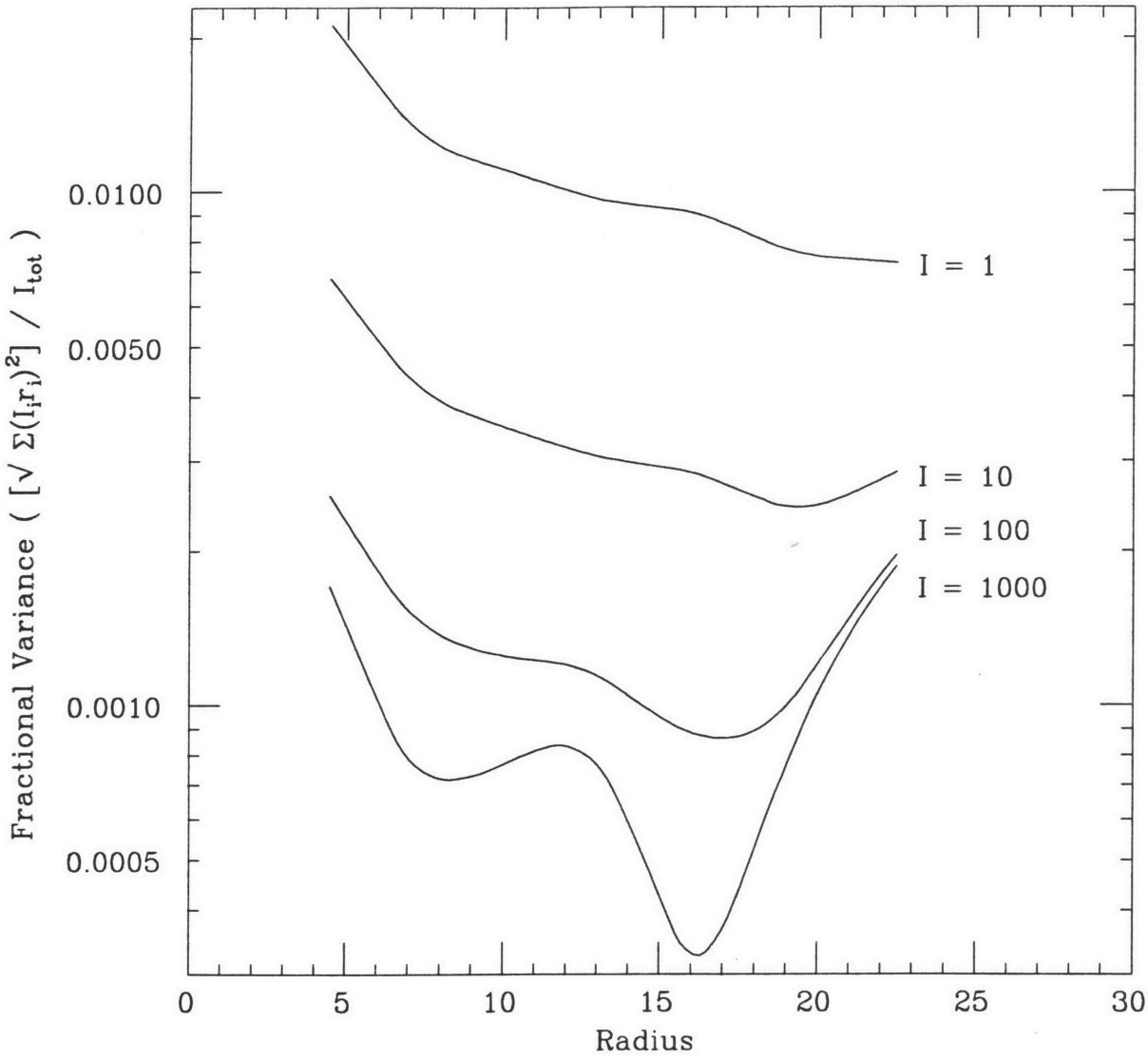


**Figure 2.10**

Statistical fluctuation in non-central points for specimen with single central inclusion. Counts expressed as a fraction of central amplitude. Number of views is fixed at 50. The curves are labeled with the value of the central pixel for a *single* projection.

$$\sigma^2 = \frac{(2 * \text{total})}{v}$$

$$\sigma = \sqrt{\frac{(2 * \text{total})}{v}} \tag{2.2}$$

Where the $N_i$ are the reconstructed values over all contributing pixels. Of course, the sum could be taken over all image pixels, since all others are assumed to contribute an average value of zero. This noise contribution will add to the contributing pixels as well, and must be convolved with their $\sqrt{N}$ noise to obtain the total noise.

For a low contrast image extending over the entire field, we may express the relative noise in terms of the average image value $\bar{N}$ and replace 'total' with $v^2\bar{N}$, yielding a noise over the image of:

$$\frac{\sigma}{\bar{N}} = \sqrt{\frac{2 * total}{\bar{N}^2 v}}$$

$$\frac{\sigma}{\bar{N}} = \sqrt{\frac{2v^2\bar{N}}{\bar{N}^2 v}} = \sqrt{\frac{2v}{\bar{N}}} \tag{2.3}$$

A low contrast image in which the pixel values are just equal to their statistical fluctuation requires that

$$\sigma/\bar{N} = 1, \tag{2.4}$$

and so v=N; the total counts in the reconstructed pixel must be equal to number of angular views in the reconstruction, and so equal to the square root of the number of pixels in the reconstruction. In other words, the number of counts contributed by each pixel from a single angular view is equal to 1. The results of computer simulation of an extended image reconstruction with statistical noise is shown in Figure 2.11.

Clearly, the use of a reconstruction technique to produce an image does exact a price: for a low contrast image, the statistical noise in the final image is not equal to the square root of the image value, but is worsened by a factor of $\sqrt{v}$. The relative fluctuation is that which would be expected from the counting statistics for a single view.

It is also clear that the effect of reconstruction on statistical noise depends on the image. For an image made up of a few small areas of high intensity, these areas have a relative statistical variation which is approximately equal to $1/\sqrt{N}$ where $N$ is the

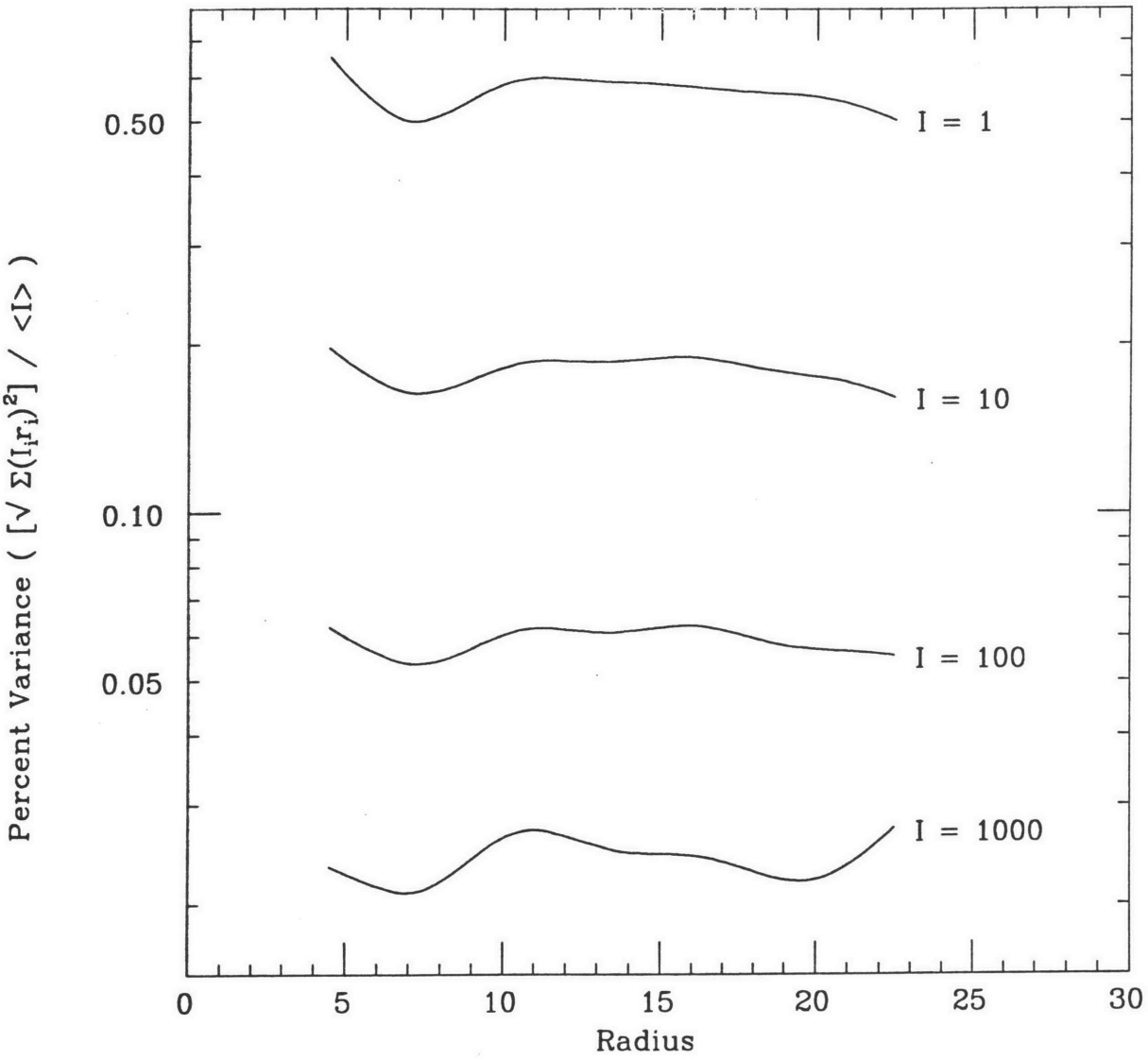


**Figure 2.11**

Statistical fluctuation in a low contrast extended specimen. The result is expressed as a fraction of the reconstructed value. All curves represent 50 view reconstruction, and are labeled with the value of the central pixel for a *single* projection.

reconstructed count in that area. Images which contain large uniform areas will have relative variations on the order of $\sqrt{v/N}$.

# CHAPTER 3
## Synchrotron Fluorescence Tomography

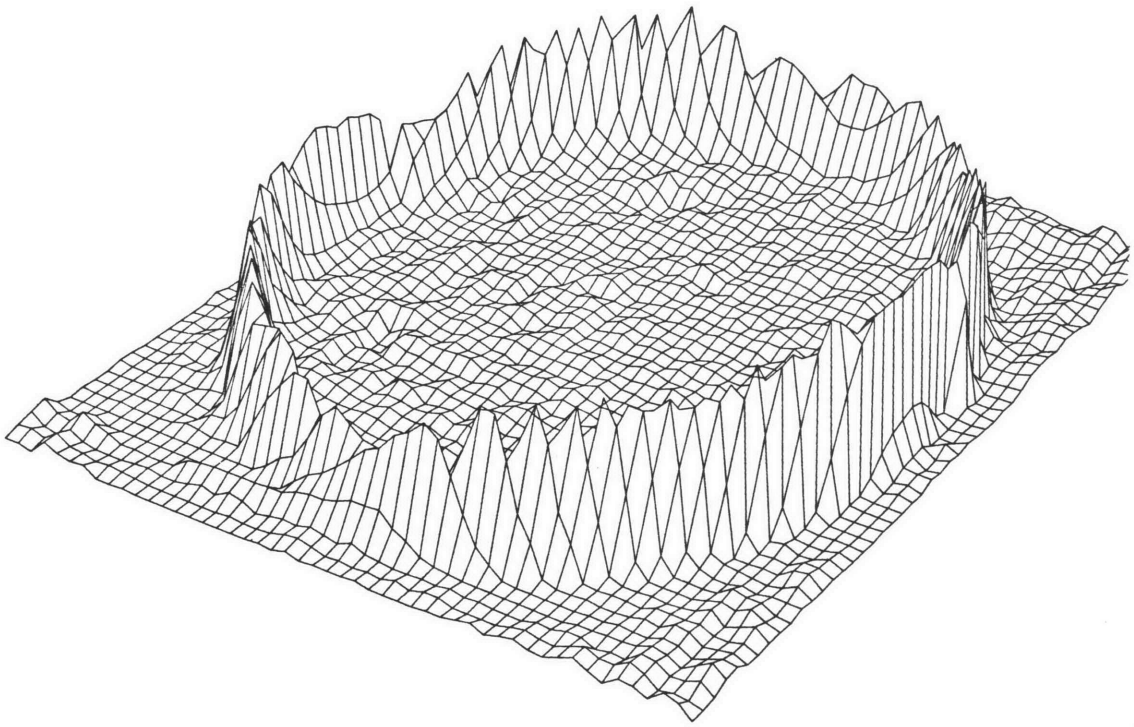

# CHAPTER 3
## Synchrotron Fluorescence Tomography

Although the acquisition of data for fluorescence tomography does not require an elaborate experimental setup, an appropriate x-ray source must be available. For our purpose, the source must be able to provide high flux density beam spot with a size considerably less than 1 mm. For example, the analysis of trace amounts of Fe in an organic sample requires the use of an incident beam with an energy above the K edge of Fe. For maximum sensitivity, the incident beam should have an energy that is just slightly greater than that of the K edge - about 7.2 keV. Given this beam energy, the sample must be small enough that the incident beam can penetrate the specimen, and the induced Fe x-rays can escape from the interior.

The table below indicates the attenuation distance for various trace element fluorescent x-rays, for two sample matrices. The first matrix is an organic matrix with a density of .5 gm/cm$^3$; the second is a silicon matrix with a density of 3 gm/cm$^3$.

| Trace Element | Energy (keV) | Attenuation Distance (Organic matrix) | Attenuation Distance (Silicon matrix) |
|---|---|---|---|
| K | 3.312 | 290 | 5 |
| V | 4.949 | 1030 | 13 |
| Fe | 6.490 | 2300 | 28 |
| As | 10.532 | 10500 | 117 |
| Mo | 17.443 | 35000 | 509 |

The reconstruction of the image is greatly simplified if there is negligible attenuation, and so the ideal sample would be smaller than the attenuation distances shown. Clearly, the most favorable situation is the analysis of heavy elements in a light matrix. However, even for the case of Fe in carbon, the limiting size is about 2 millimeters.

To obtain useful spatial information, a reconstruction grid of at least 10x10 pixels is required, thus the beam size should be at least an order of magnitude smaller than the specimen size. For many purposes, a reconstruction grid of 50x50 is desired. Although it would be useful use monochromatic x-ray beams of micron size, it is clear that the technique may be tested with a 100 micron beam if an appropriate

organic specimen is used. Although such tests have now been done successfully and the results presented here, the technique will be most useful when it can be applied to sub-millimeter specimens; this will have to wait for the availability of micron size beam spots.

Beam lines on the x-ray ring of the National Synchrotron Light Source started to become available in 1985. Although a focussed microbeam end-station was planned based in part on our design, it had not been completed at the time of this writing. Fortunately, a beam line operated by the Oak Ridge National Laboratory was made available for a short experimental run. The beam line was designed for x-ray diffraction work, and could be modified to produce beams on the order of 200 microns in diameter through a combination of focussing and slit collimation [Sp82]. The predicted photon flux was $10^{11}$ photons/sec/mm$^2$. This beam density was difficult to achieve in practice, however, and most of the experiments were done with a beam at least one order of magnitude weaker. A schematic diagram of the beam line is shown in Figure 3.2.

The first optical component in the beam line is a sagittal focus silicon crystal monochrometer. The monochrometer has an energy resolution of $\delta E/E = 1.5 \times 10^{-4}$, and can be tuned over a wide energy range. One crystal of the monochrometer is bent to provide focussing in the horizontal direction. A platinum grazing incidence mirror is used to focus the beam in the vertical direction, resulting in imaging the synchrotron source spot with a magnification of approximately 1:1. The focussing combination ideally yields a photon flux of $10^{11}$ photons/sec in a 1 mm$^2$ beam spot.

The beam exits the vacuum system through a beryllium window, traverses a short path in helium, and enters the sample position through a Kapton window. A collimating slit system is situated just past the beryllium window, and is used to define the beam size. The smallest practical beam size is limited by two factors: the need for a minimum acceptable count rate and the effect of beam divergence.

A lower limit on the beam diameter is set by the need to produce a reasonable count rate for the expected elemental concentrations. Consider an organic carbon matrix of density $\approx$ 1 gm./cm$^2$. We wish to determine the count rate from a single pixel of the sample which contains a mass fraction $f$ of iron. Pixels are assumed cubic. Using the following notation:

$d$ = pixel width (centimeters)

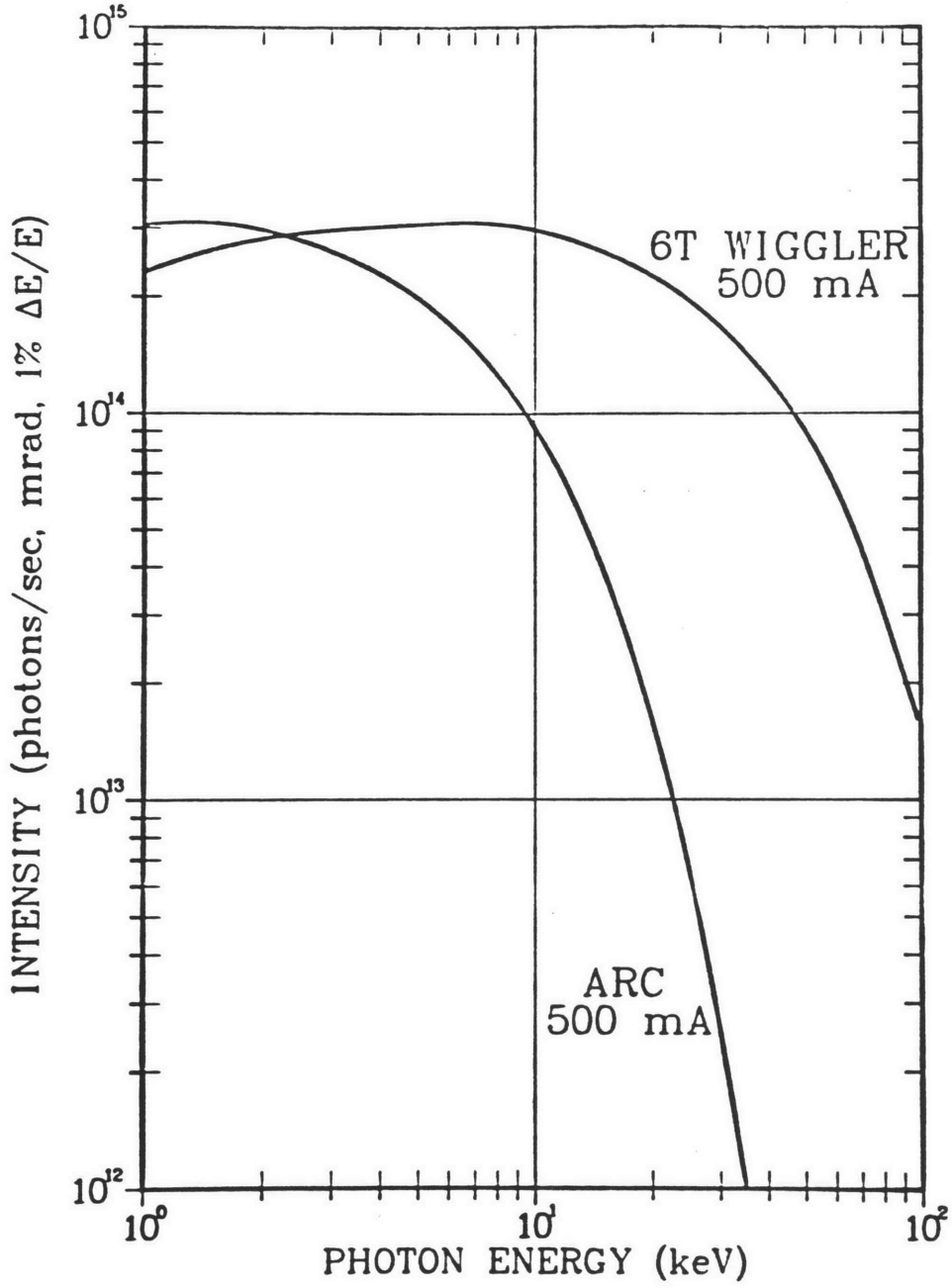


**Figure 3.1**
**Beam Parameters NSLS**

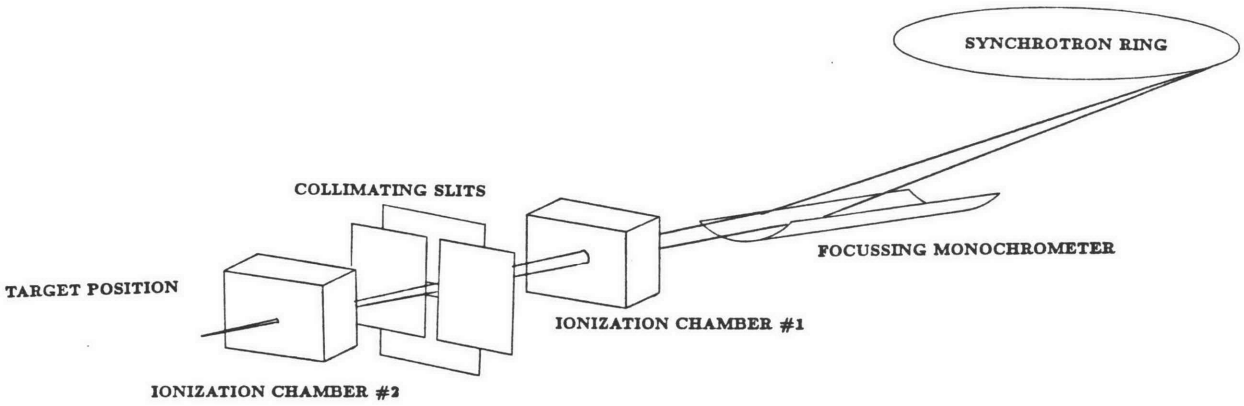


**Figure 3.2**
**ORNL Beam Line**

$J$ = incident photon flux (photons/sec-cm$^2$)
$f$ = trace element concentration (gm/gm)
$\sigma$ = fluorescent cross-section (cm$^2$)
$\rho$= matrix density (gm/cm$^2$)
$\omega$ = trace element fluorescent yield
$\Omega$ = detector solid angle (steradians/$4\pi$)
$A$ = atomic number of trace element
$N$ = Avagadros number

the total number of iron atoms in the pixel volume $d^3$ is

$$N_{tot} = f\rho d^3 N/A$$

The number of induced photons emitted from the volume element $d^3$ is given by:

$$N_\gamma = Jf\rho d^3 \sigma N/A\omega$$

so that the number of photons detected is

$$N_\gamma = Jf\rho d^3 \sigma N/A\omega\Omega$$

If we assume a trace element concentration of 50 ppm., and with

$d = 250 \times 10^4$ centimeters
$J = 10^{12}$photons/sec-cm$^2$
$\sigma = 3 \times 10^{-20}$cm$^2$
$\rho = 1$gm/cm$^2$
$\omega = .35$
$\Omega = 3 \times 10^{-4}$

We predict a rate of 25 counts per second. For our collection time of one second, this pixel size is a good choice for the desired sensitivity of 50 ppm.

The second factor determining minimum beam size, and the real limitation in this case, is the divergence of the beam between the collimating slits and the sample. Given the beam divergence of 5 mrad. horizontally and .3 mrad. vertically, the present working distance of 20 cm. produces a beam spread of 500 microns in the horizontal direction, and 80 microns in the vertical direction. In order to image a 10 mm$^2$ square object on a 50x50 pixel array, a beam resolution of less than 200 microns is necessary. The 500 micron limitation of the horizontal divergence was dealt with by orienting the object so that the horizontal dimension of the photon beam determined the thickness of the slab of specimen and the vertical dimension determined the pixel width. This allowed the use of a 500 micron (horizontal) by 150 micron (vertical) collimating slit opening, resulting in a vertical beam size of about 230 microns (Figure 3.4) and a slab thickness of 750 microns. This results in a minimum detection limit of 3 ppm. for a

beam with an intensity of $10^{11}$ photons/mm$^2$. Preliminary runs indicated however, that the actual intensity was down by at least a factor of 10, presumably because of component misalignment. This indicates an approximate lower limit of 30 ppm.

It was decided to collect data for a 50x50 grid, scanning over a cross-section of 10 mm. diameter. This gives a final spatial resolution of 200 microns in the reconstructed image. Under ideal circumstances, this would require scanning the beam laterally through 50 microns in 200 micron steps, for each of 300 angular positions distributed equally through 180 degrees. Because of time limitations, it was decided to use only 50 angular positions.

The sample was mounted on a 4-axis positioning stage shown in Figure 3.3. The x, y, and $\theta$ motions are driven by stepping motors which are under computer control. The finest resolution available for the x and y axes is 1.58 microns; the finest angular step on the $\theta$ stage is .9°. Data collection is done by rastering the stage in x and $\theta$. The total x distance required to span the sample is divided into 50 points, and the stage is moved under computer control to each of these points in sequence. At each x point, the $\theta$ stage is stepped through 50 points spaced uniformly through 180°. Data is collected at each point in the x-$\theta$ raster for a preset amount of time, typically 0.5-1.0 seconds. At each of the 2500 stage positions which make up the total scan, data is collected and stored.

Fluorescent photons are collected by means of a lithium-drifted silicon (Si-Li) detector. The detector used has an energy resolution of 240 eV; detectors with resolutions of $< 135$ eV. are available. The detector resolution was not a serious limitation in this particular experiment, since we are dealing with concentrations of greater than 100 ppm. With much lower trace element concentrations, the detector would not be able to separate the fluorescent x-ray signal from the primary scattered radiation. In the present experimental setup, analytical background subtraction is not possible, since the full spectrum at each spatial point was not saved. The combination of background subtraction and a high resolution detector should allow the detection of trace elements below the 100 ppb level.

The data collection geometry is shown in Figure 3.5. As the specimen is scanned through the beam, fluorescent x-rays are emitted along the path of the beam through the specimen. A fraction of these x-rays are detected with the Si-Li detector. The primary sources of noise are from the elastic and inelastic scattering of the incident

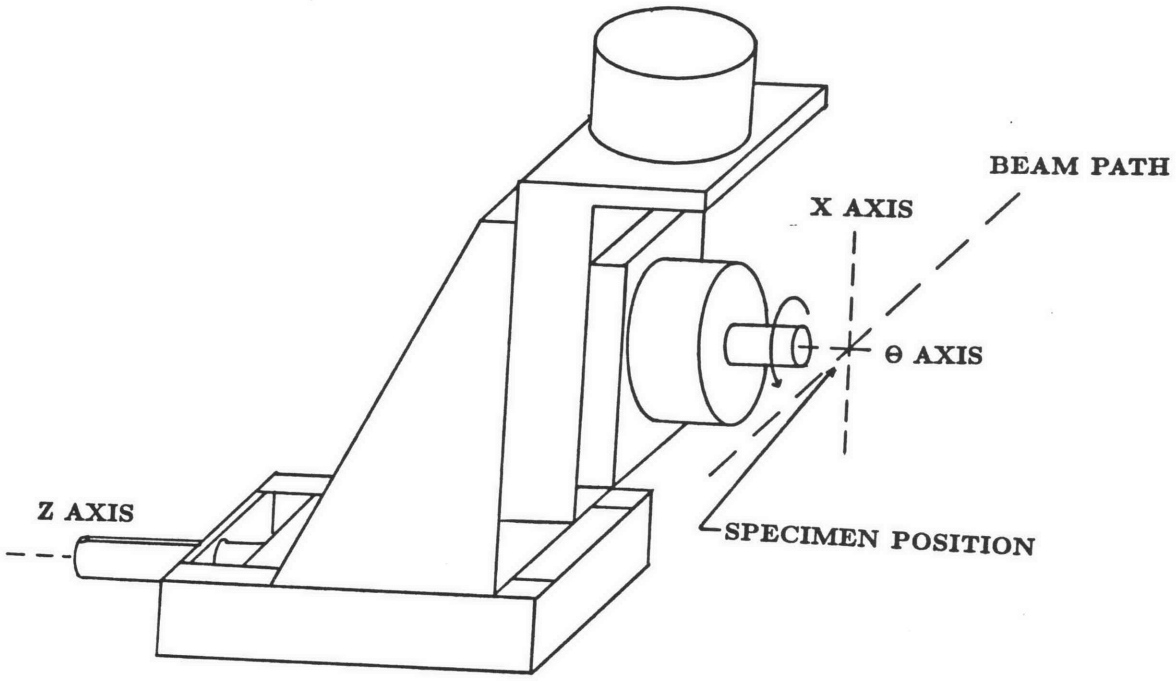


**Figure 3.3**
**Tomographic Stage**

With the beam position fixed, the specimen must be scanned through the beam while being rotated. This computer controlled stage has a minimum spatial step size of 1.5 microns, and a minimum rotation angle of $< 1°$.

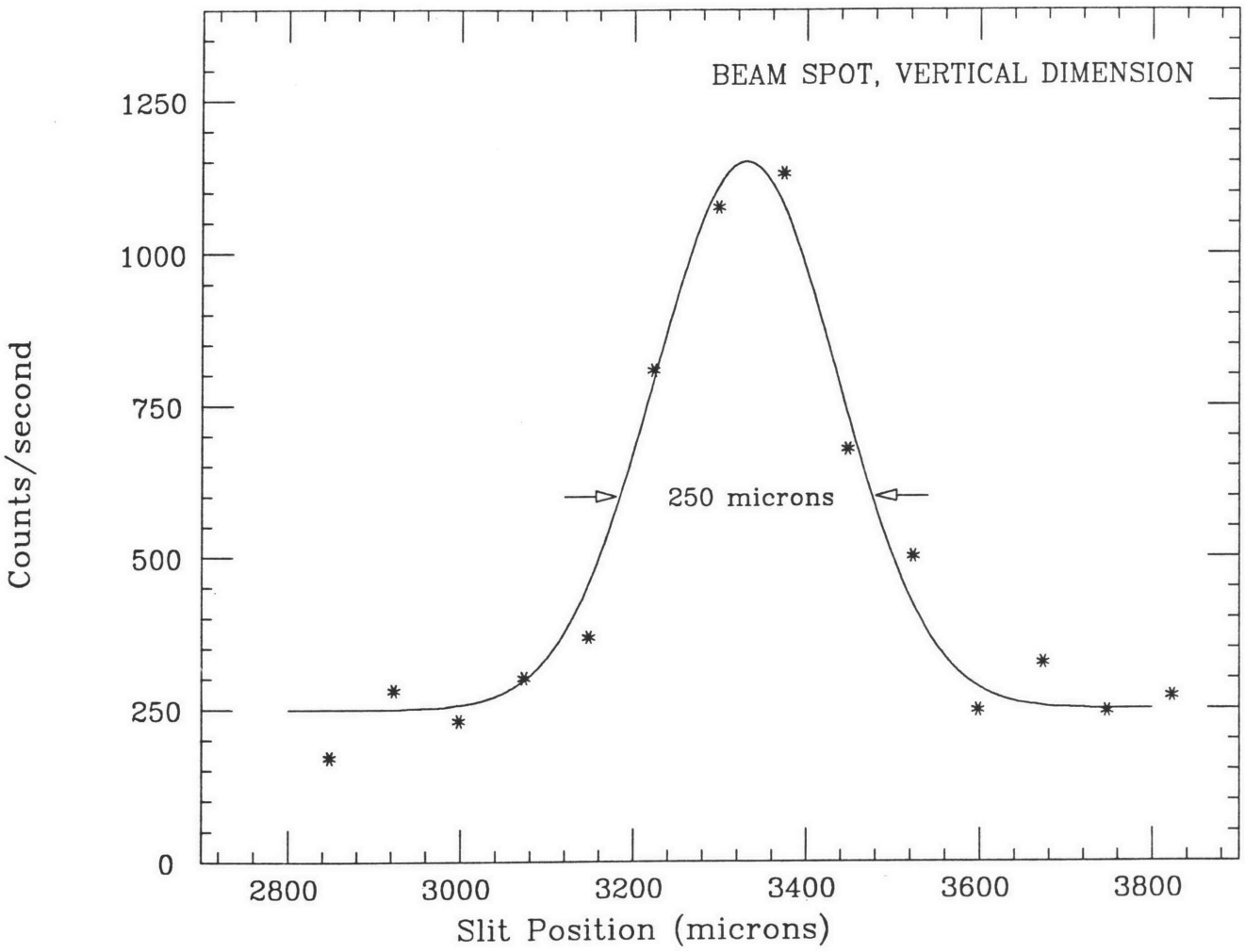


**Figure 3.4**

Beam Profile at Sample Position. The profile was produced by scanning a Fe bearing glass fiber 75 microns wide across the beam.

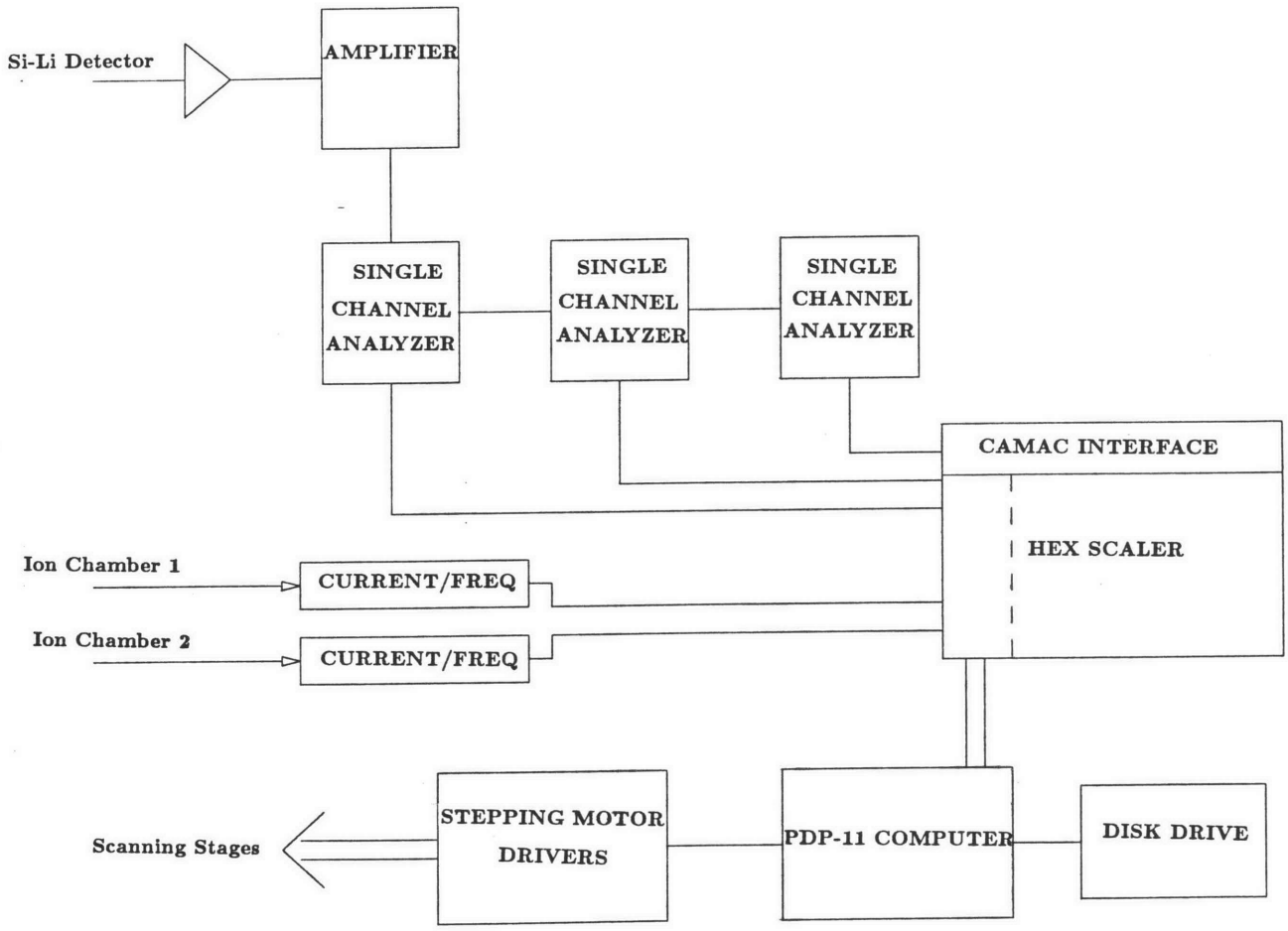


**Figure 3.5**
**Data Collection System**

beam. The polarization properties of the synchrotron radiation reduce the cross-section of scattering at 90° in the plane of the synchrotron. For this reason, the Si-Li detector is mounted at that position.

The pulses from the Si-Li preamplifier are amplified by means of a gaussian shaping amplifier; the use of a pulsed optical reset preamp and pulse pileup rejection circuitry allow count rates in excess of 10 kHz. without significant loss of resolution. Improvements in the detector electronics should allow rates in excess of 70 kHz. This is important for high sensitivity measurements, since the count rate into the detector is dominated by the scattered synchrotron beam. An increase in maximum count rate would allow a higher beam intensity to be used before the detector electronics is loaded down.

The x-ray spectrum was recorded with a pulse height analyzer for the duration of each scan. Unfortunately, the entire spectrum could not be saved on a point-by-point basis because of the excessive data transfer time that would be involved. For this reason, the output signal was passed through a set of three single channel analyzers, each set to a particular x-ray line of interest. The logic pulses from the SCA's were used to increment a CAMAC scaler. When the stage is moved to each x-$\theta$ point, the scalers are cleared, and a timer is started. Counts are collected for a preset time, and the accumulated counts are stored. The stage is then moved to the next point in the scanning sequence. These operations are repeated under computer control, until all 2500 spatial points have been measured. The file of data is stored on disk for later analysis.

The dwell time at each point was one second. Count rates were sufficiently high that a dwell time as short as 100 msec. could have been used except for a stepping motor controller overhead time of $>$ 500 msec. which dominated the collection time. The result is that a full scan with the present setup required more than a full hour of beam time. With improvements in detector electronics and stepping motor control, similar scans could be done in less than 10 minutes.

For the purpose of normalizing the data to beam intensity fluctuations, the current from a pair of ionization counters, one before and one after the collimating slits, is recorded. This was done by converting each current into a pulse frequency, and counting the pulses with a CAMAC scaler.

The experimental conditions were optimized to detect the presence of iron in small organic samples - this required a photon energy of 7.2 KeV. The range of 7.2 KeV photons in a carbon matrix is a few millimeters, and therefore the test samples were 5 millimeters or less in diameter.

Two specimens were selected to provide a test of the technique. Specimen #1 was a common honeybee (Figure 3.5) There is a significant amount of interest[] in the distribution of trace amounts of iron in certain organisms, including the honeybee. It has been determined that some organisms are sensitive to magnetic fields, primarily through the action of magnetic fields on inclusions of magnetite ($Fe_3O_4$) held within the organism's body. These inclusions have been located in particular bacteria and algae, and there is interest among insect anatomists in determining the form and location of such structures within the body of the honeybee. Although these magnetite inclusions are much smaller (10 microns) than the resolution of the present system, it is hoped that a map of the distribution of iron in the bees body on a coarser scale would be useful. The main advantage of this specimen is that it is the right size - a beam tuned just above the K edge of iron is not highly attenuated in traversing the sample.

Specimen #2(Figure 3.7) was a artificial calibration object ('phantom') made up of two components. An outer shell of plastic tubing containing titanium and iron was filled with a small amount of epoxy cement. Two 75 micron glass fibers were inserted parallel to the long axis of the tubing. The glass fibers were drawn from wafers of Trace Element Standard #612 obtained from the National Bureau of Standards. This glass contains approximately 500 parts per million of a wide range of elements (Figure 3.8).

For the analysis of the bee abdomen, the bee was cemented onto the scanner as shown in Figure 3.3. Care was taken to use an adhesive and stage materials that contained no significant metal contamination. The SCA settings were adjusted to detect the iron $K_\alpha$ line and the scattered synchrotron radiation. During the scan, it was observed that a significant amount of iron was being detected from some parts of the specimen. The maximum count rate observed for the iron signal was approximately 1000 counts/sec. The total accumulated spectrum is shown in Figure 3.9.

Specimen #2 was run with SCA settings set to detect both iron and titanium. As data was collected, the displayed iron projection data clearly showed the 500 ppm.

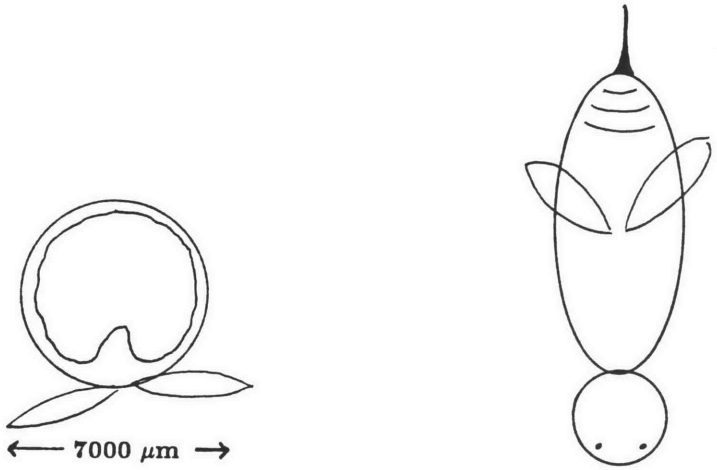


**Figure 3.6**

Specimen #1, Bee. Top view and cross-section through abdomen.

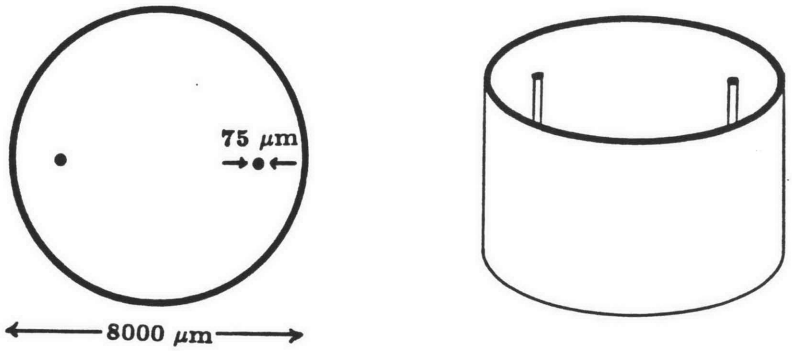


**Figure 3.7**

Specimen #2, 500 ppm. Glass Strands in Tube. Two trace element glass fibers are imbedded with epoxy cement into a plasic tube, coaxial with the tube. Fiber thickness is 75 microns. Tube wall thickness is also 75 microns. The tubing contained $>$ 1000 ppm titanium, as well as some iron.

| Z | Element | KODAK TEG-50-B | KODAK TEG-50-C | NBS #612 | NBS #610 |
|---|---|---|---|---|---|
| 3 | Li | | 47 | | |
| 4 | Be | | 42 | | |
| 5 | B | | 51 | (32) | (351) |
| 11 | Na | 397 | 185 | | |
| 12 | Mg | 256 | 73 | | |
| 13 | Al | 60 | | | |
| 19 | K | | 94 | (64) | (461) |
| 20 | Ca | 2025 | 570 | | |
| 22 | Ti | | | (50.1) | (437) |
| 23 | V | | 52 | | |
| 24 | Cr | 47 | 47 | | |
| 25 | Mn | 48 | 45 | (39.6) | (485) |
| 26 | Fe | | 64 | 51* | 458* |
| 27 | Co | 46 | | (35.5) | (390) |
| 28 | Ni | 52 | | 38.8* | 458.7* |
| 29 | Cu | 51 | 49 | 37.7 | 444 |
| 30 | Zn | 53 | | | 433 |
| 31 | Ga | | 48 | | |
| 32 | Ge | | | | |
| 33 | As | 115 | | | |
| 34 | Se | 39 | | | |
| 37 | Rb | | 46 | 31.4* | 425.7* |
| 38 | Sr | | 48 | 78.4* | 515.5* |
| 40 | Zr | | 45 | | |
| 42 | Mo | | 59 | | |
| 47 | Ag | | 56 | 22.0* | (254) |
| 48 | Cd | 45 | | | |
| 49 | In | | 48 | | |
| 50 | Sn | | 47 | | |
| 51 | Sb | 57 | | | |
| 52 | Te | 45 | | | |
| 56 | Ba | 50 | 44 | | |
| 60 | Nd | | | (36) | |
| 79 | Au | | | (5) | (25) |
| 80 | Hg | 55 | | | |
| 81 | Tl | 46 | | | |
| 82 | Pb | 59 | | 38.57* | 426* |
| 83 | Bi | 49 | 43 | | |
| 90 | Th | | | 37.79* | 457.2* |
| 92 | U | | | 38.38* | 461.5* |

**Figure 3.8**

**NBS Trace Element Standard #612 500ppm.**

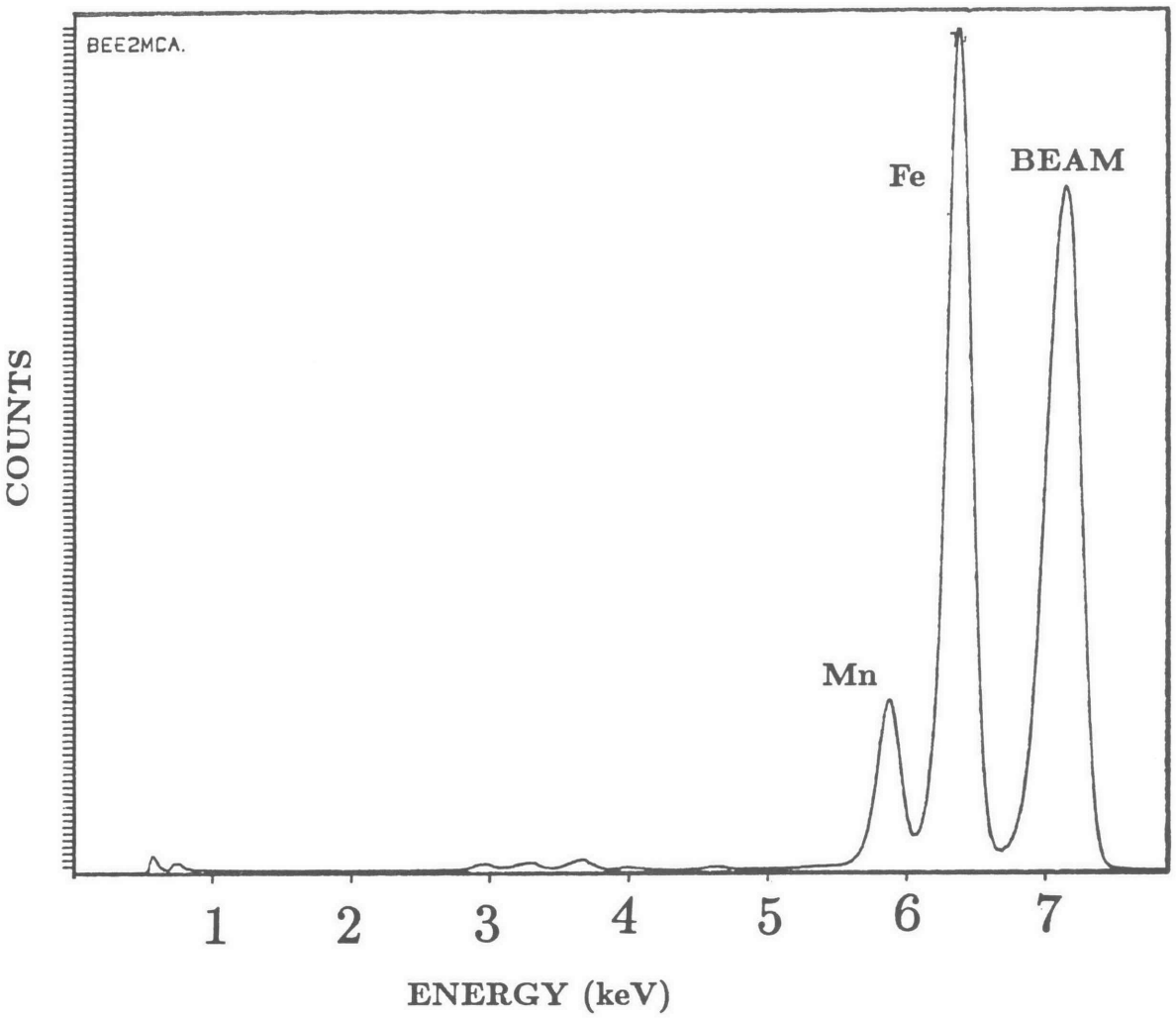


**Figure 3.9**
**Accumulated x-ray spectrum, 7.2keV on Bee**

glass fibers. Maximum count rate for the titanium signal was 4000 counts/sec. The maximum count rate for the iron signal was approximately 500 counts/sec.

A crude tomographic analysis and display was done immediately after the experiment, and the results clearly indicated the detection of the internal structure of the specimens. The data were then reanalyzed more carefully at MIT, and the results of the image reconstructions is shown in Figures 3.10-3.13.

### Results

The results of the tomographic analysis are most easily interpreted for the artificial object, specimen #2, since its composition is known. The physical structure of the distributions for both iron and titanium are faithfully reproduced in the tomographic images. The spatial resolution is, as expected, limited by the 240 micron resolution of the beam. For the image field width of 8000 microns, this is a resolution of 1.5 pixels.

The signal strength for the 500 ppm concentration of iron in the glass fibers indicates that a concentration of $\leq$ 20 ppm could easily have been detected under the same experimental circumstances. The ratio of the iron signal to the background fluctuation is 60:1.

The intensity of the titanium count rate indicates a concentration of greater than 4000 ppm in the plastic tube. Because of the extended nature of the titanium image, the ratio of maximum to minimum image intensity is only 20:1.

The iron distribution in the honeybee abdomen shows clear internal structure. The inside surface of the body cavity is visible, as is a high concentration structure near the (former) wing attachment.

### Future Development

The present results, although crude, are extremely encouraging. With simple improvements in experimental technique, significantly better results should bee obtained. An increase by a factor of 10 to the optimum value of the beam intensity would allow an increase in spatial resolution to less than 80 microns. Precise monitoring of short term beam fluctuations will allow these fluctuations to be compensated for in the reconstruction. Modifications in the data acquistion system will increase the data

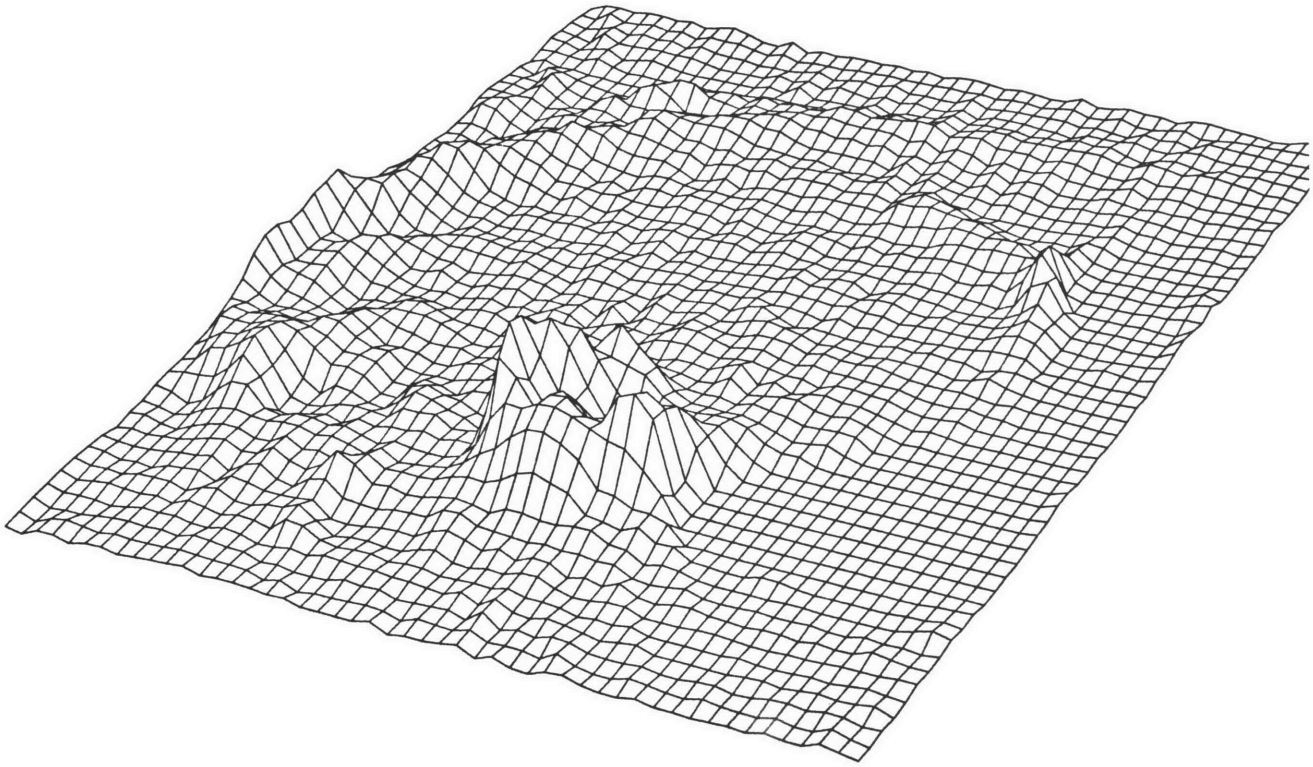

**Figure 3.10**
**Reconstructed Image: Specimen #1, Bee in Iron**

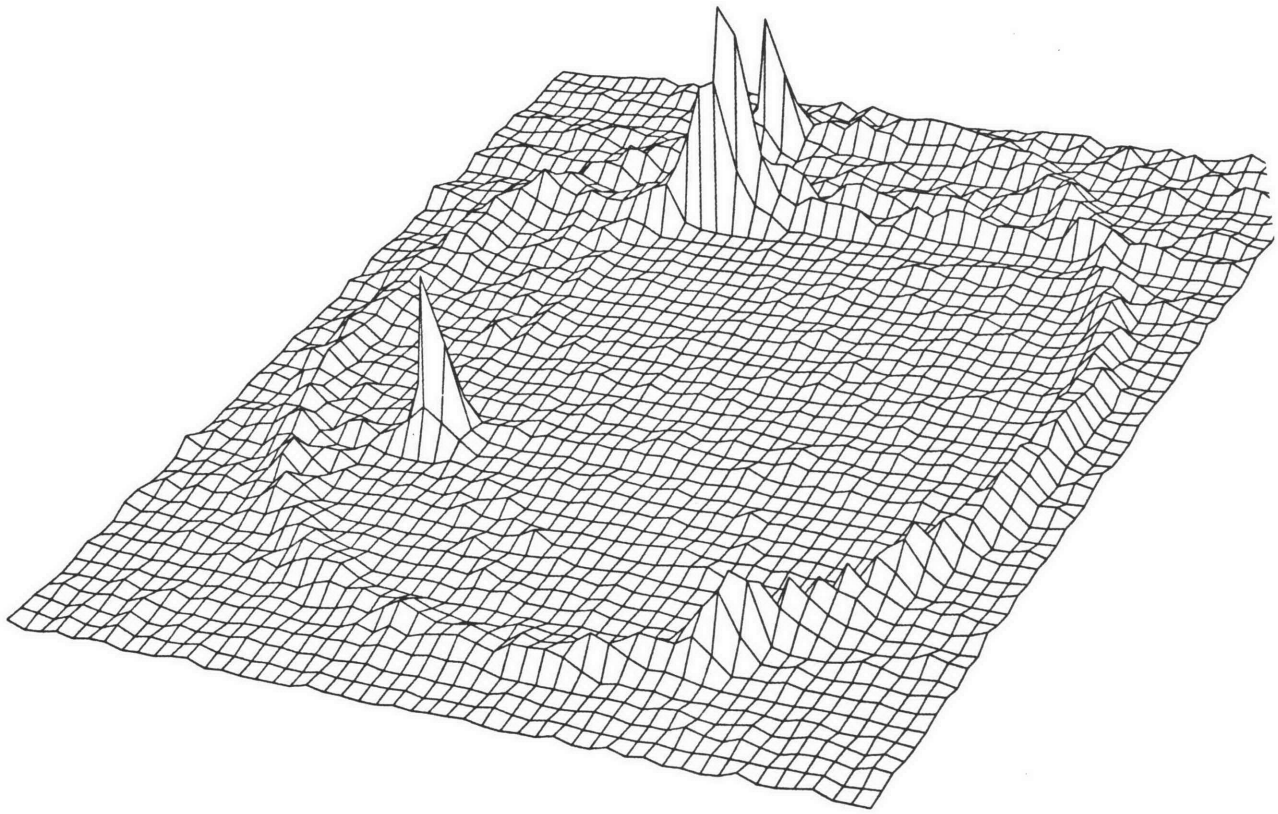

**Figure 3.11**
**Reconstructed Image: Specimen #2, Phantom in Iron**

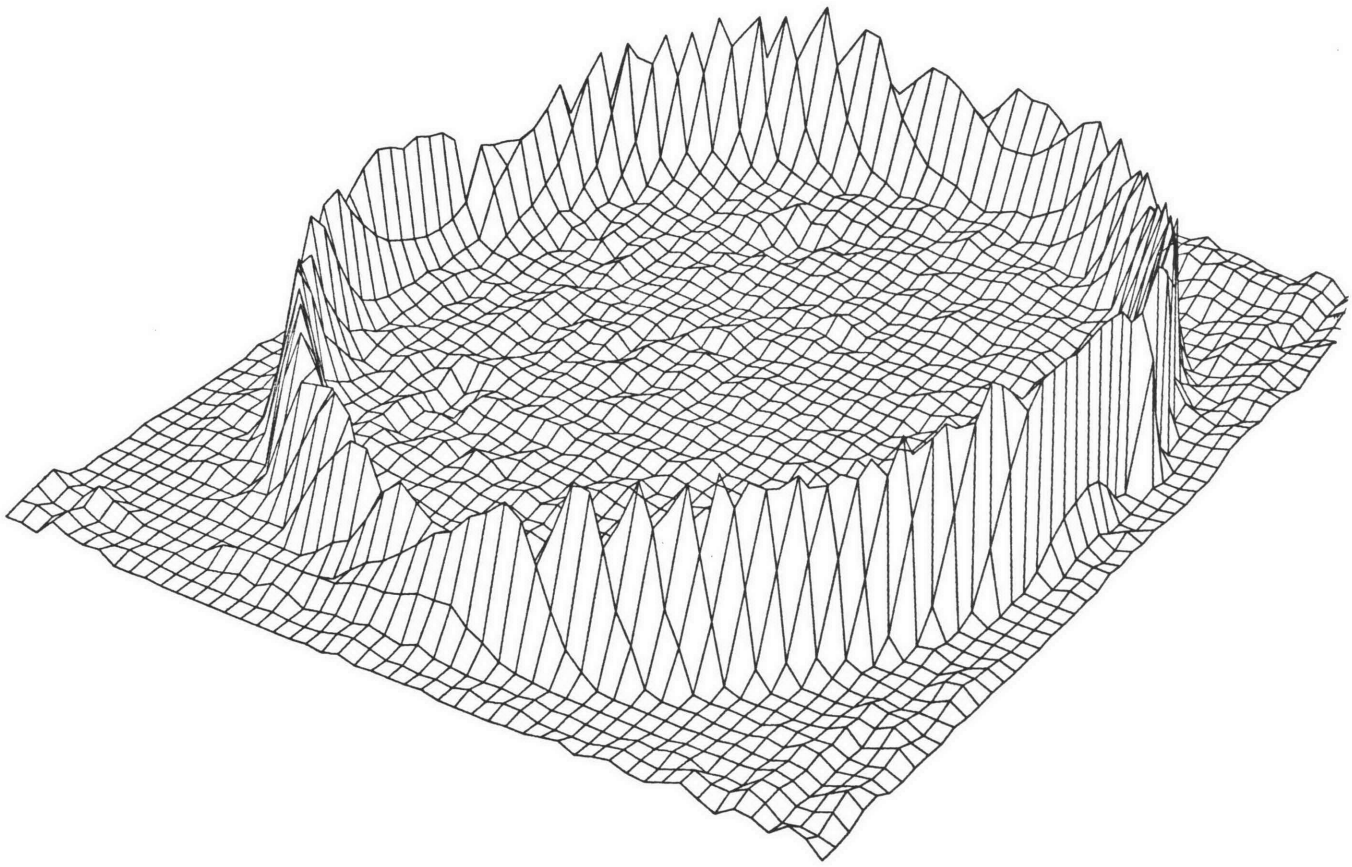

**Figure 3.12**
**Reconstructed Image: Specimen #2, Phantom in Titanium**

collection efficiency by almost a factor of 2. The next set of experiments will utilize these improvements.

A beam line specifically designed for microprobe work will allow photon flux densities in excess of $10^9$ photons/sec-$\mu^2$, as compared to an estimated $10^5$ photons/sec-$\mu^2$ for the present work. This will be done through the use of a lower resolution ($\delta E/E = .05$) monochrometer coupled with focussing optics [Appendix A]. It is expected that this combination will provide spot sizes down to 30 micron diameter.

It has recently been suggested [Sm86] that the fabrication of Fresnel Zone Plates with high efficiency for x-ray energies of 7 keV is possible. The use of such a device for beam focussing would allow the creation of sub-micron beam spots. At these spatial dimensions, the technique of elemental tomography should yield spectacular results for problems such as the analysis of trace element distribution in biological cells as well as man-made silicon microstructures.

# CHAPTER 4
# Optical Tomographic Imaging of Ion Beams

# CHAPTER 4
## Optical Tomographic Imaging of Ion Beams

A light-sensitive tomographic imaging system has been designed to monitor the intensity cross-section of a high current ion beam. The light emitted by the interaction of the ion beam with residual gas in the vacuum chamber is detected with a set of one dimensional photodiode arrays. A two dimensional intensity map of the beam cross-section is tomographically reconstructed.

### DESIGN PARAMETERS

A means to characterize the intensity distribution of an intense ion beam was required during the development of a new ion-implantation device. A system for this purpose must not distort the beam during measurement, and must not contaminate the vacuum system if it is to be used during the implantation process itself. One of the several systems that has been developed for this purpose utilizes the light emitted by the interaction of the ion beam and the residual gas in the vacuum chamber.

Measurements indicate that the luminosity of a volume element of residual gas is proportional to the current passing through the volume element. It has also been determined that the luminosity is proportional to the gas pressure at the volume element. Thus, a measurement of the visible luminosity throughout the ion beam volume will provide a measure of the ion current. The system discussed here is designed to image the cross-section of the beam at a single point.

Since only side views of the beam are available, the cross - sectional intensity distribution must be determined from a set of such views. The residual gas is so tenuous that there is a negligible amount of light absorption by the gas. Thus, a measurement of the brightness of the object is actually a measurement of the integral of the brightness distribution of the object along the line of sight. The availability of a measurement of the line integrals through a two-dimensional function allows the use of tomographic reconstruction techniques to determine the values of the function itself.

In order to provide a sufficient number of line integrals through the cross - section of the ion beam, it is necessary place cameras in the image plane, at several angles to the beam axis. The one-dimensional images from the cameras are acquired by a

computer, which then performs the tomographic calculation. The two dimensional beam intensity distribution is then displayed.

Although the cameras used have good spatial resolution, the number of cameras was constrained to 8. The quality of reconstructed images using such a small number of angular views was investigated, and it was determined that an eight view reconstruction of the beam profile would be useful for beam monitoring. An indication of the improvement in image quality is demonstrated in Figure 4.6. Here, a computer simulation was performed assuming two objects two units in diameter and separated by five units. At 8 views, the quality is reasonable. A significant increase in image quality requires twice the number of views. An ideal system would allow the acquisition of approximately 50 views.

The system (Figure 4.1) images an ion beam with a maximum diameter of 15 centimeters at a working distance of less than 20 centimeters from the beam axis. The resolution desired over the imaged volume 3 millimeters. The intensity of light emission from the beam varies over a wide range, and is on the order of $10^{-7}$ watts/cm$^2$. The beam is assumed not to have rapid spatial variation along the beam axis, and is assumed not to vary in time over intervals of less than a second. Line images should be updated at a rate of about 1 per second, and tomographic images should require less than 30 seconds at most.

## LINE CAMERA

The single view camera is made up of three major components:

1) The linear photodiode array

2) The array driver electronics

3) The imaging lens system

## PHOTODIODE ARRAY

The linear photodiode array used for testing is the RETICON Model EC/17-256. This array contains 256 pixels with 50 micron spacing. The pixel size is 50 x 420 microns. Each pixel may be modeled as a photodiode in series with a capacitor. The capacitor is initially charged up, and discharges through the photodiode at a rate proportional to the incident light intensity. The device is periodically recharged, and the total integrated light intensity is proportional to the charge needed. The spectral

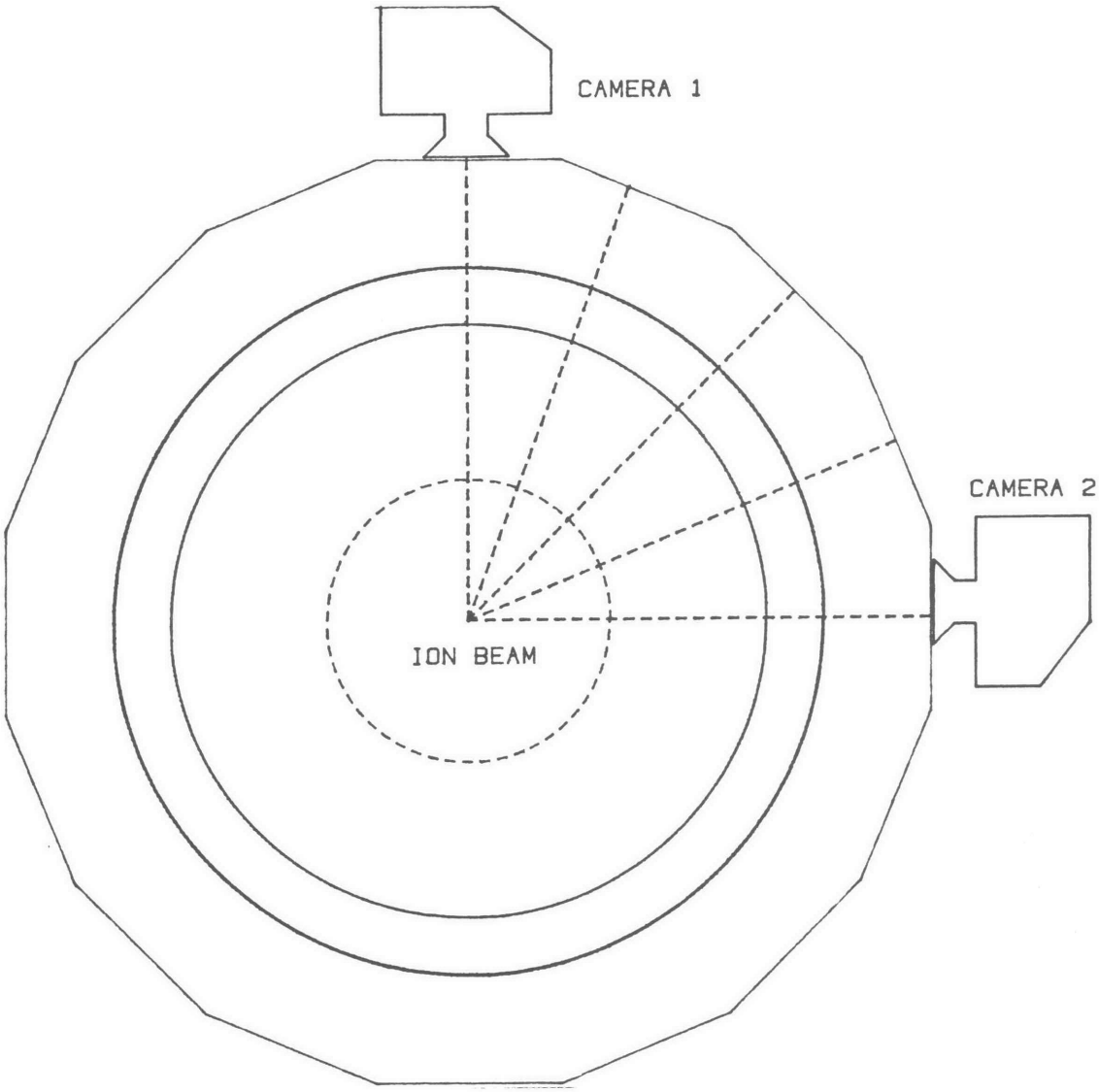


**Figure 4.1**
**Geometry of Ion Beam Imaging System**

response of the diodes extends from the near ultraviolet to the near infrared, limited primarily by the quartz cover protecting the device. The quantum efficiency is greater than 30% across the visible range.

| | |
|---|---|
| Sensitivity | 19 pa/watt/cm$^2$ |
| Dark Current | 1 pa |
| Saturation Exposure | .17 $\mu$watt-second/cm$^2$ |

**RETICON RL-256/EC 25° C**

The devices are being used at low light intensities, and the dark current contribution is important. This background can be subtracted from the signal; this requires a dark calibration measurement at the operating temperature. The dark current is a strong function of temperature, doubling every 7° C. A significant reduction of noise can be obtained by cooling the arrays with thermoelectric coolers.

Readout is accomplished with an on-chip FET multiplexer which sequentially gates the signal from each pixel onto a common signal line. The clock signal, amplifiers, and recharge circuitry are provided by the array board.

Similar devices, now becoming available from Hamamatsu, claim a much lower dark current and a larger pixel width at a lower price. A Hamamatsu 256 pixel array is being tested; if the manufacturers claims are accurate, it would be the clear choice for this application.

## DRIVER ELECTRONICS

The photodiode array is mounted on a circuit board which provides timing, video amplification, and sample-and-hold functions. The computer provides the basic clock frequency, which is used to create a multiple phase clock to drive the chip. The video signal is amplified and transmitted to the computer in a serial 'boxcar' form. Total integration time is is equal to the time required to clock out all 256 pixels, and is therefore proportional to the basic clock period.

## OPTICAL SYSTEM

The optical system is made up of a single element bi-convex lens and a rectangular aperture. The focal length of the lens is 15 mm, and lens diameter is 12 mm. The focal length is determined by the working distance, the required field of view, and the length of the photodiode array. The focus is fixed at a distance of 200 mm. It

was decided that the advantages of a more sophisticated lens would not be reflected in significantly improved image quality. The requirements of extremely wide angle of view, extreme depth of focus, and high light throughput result in such large trade-offs that the improvements available from a sophisticated multi-element lens are minor.

The wide angle of view produces an extreme curvature of field; the radius of curvature for best focus is approximately 15mm and the half length of the sensor is 12mm. As a result, the image quality degrades at the edges of the field. The presence of chromatic aberration should not be a factor in image quality due to the relative monochromaticity of the ion beam induced light emission.

The depth of field on the optical axis is dependent on the size of the lens opening. The lens opening and the distance to the object determine a particular angle, which, when extended axially some distance away from the point of focus, determines the blur size at that distance. The smaller the lens opening, the greater the depth of field, and the smaller the light intensity at the image.

In order to increase the efficiency of the system, a rectangular aperture was used in front of the lens. An out of focus point will in general be imaged as a blur with the shape of the lens aperture. In the case of a long, thin aperture, the blur will be oriented in a particular direction. The result of using such an aperture is to produce an image which is blurred in one dimension, but sharp in the perpendicular direction. For the purpose of imaging the ion beam, blur in the direction of the beam axis could be tolerated, and was increased to provide a higher intensity image. The present size of the aperture is 1.5mm X 10mm.

## TEST RESULTS

-Resolution-

The resolution of the system at the center of the field was measured for a range of object distances, with the focus fixed at 22 cm. This was done by imaging a high contrast edge and counting the number of pixels over which the intensity changed from 10% to 90% of the range. This pixel count was translated into an equivalent length at the object distance. This measurement was compared with the limiting value for a perfect lens on axis with no aberrations (Figure 4.3). The theoretical values assumed an aperture of 1.5 mm, a quantization error of 2 pixels, and an optimum focus of 22cm. The experimental values approach the limiting values quite closely.

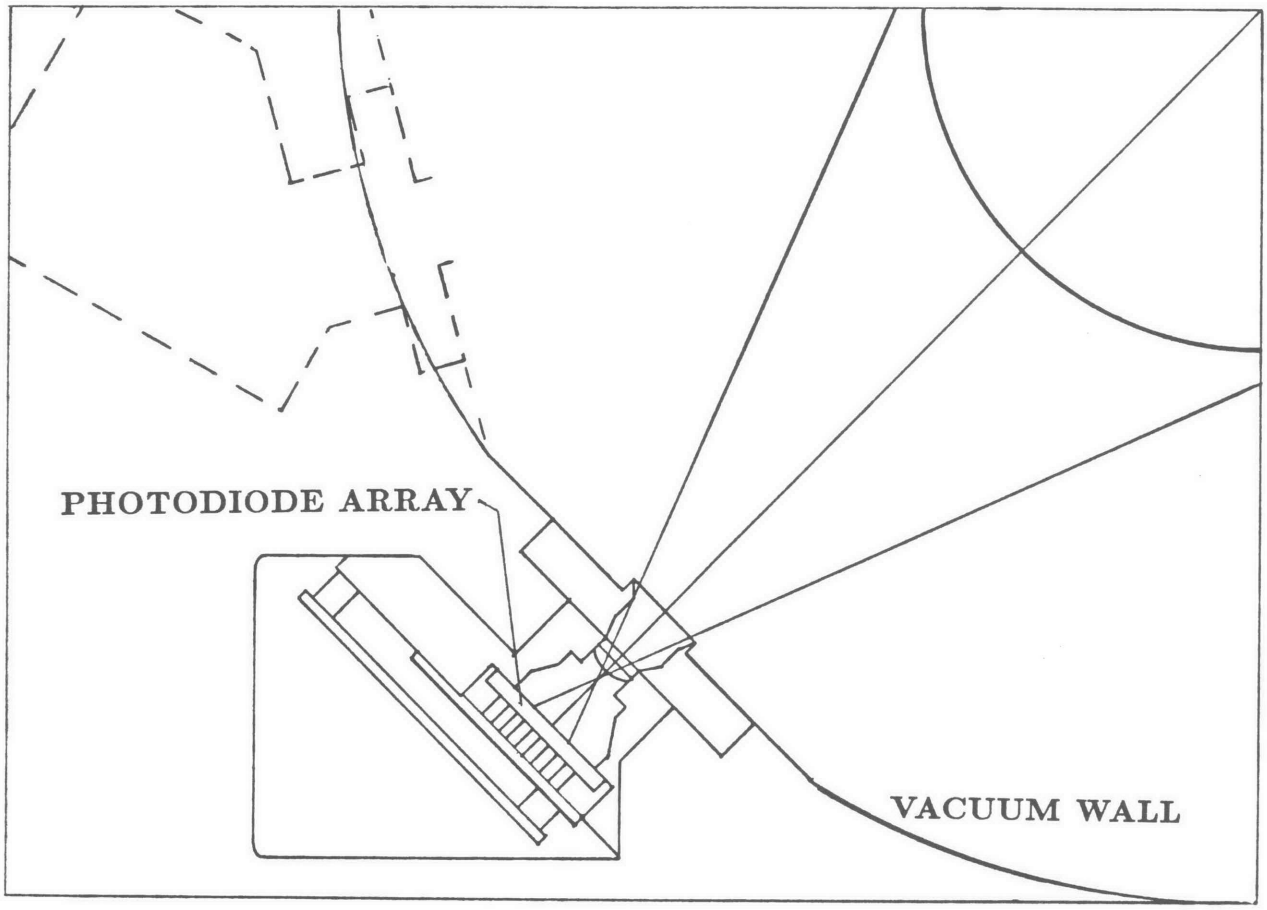


**Figure 4.2**
**CCD Camera**

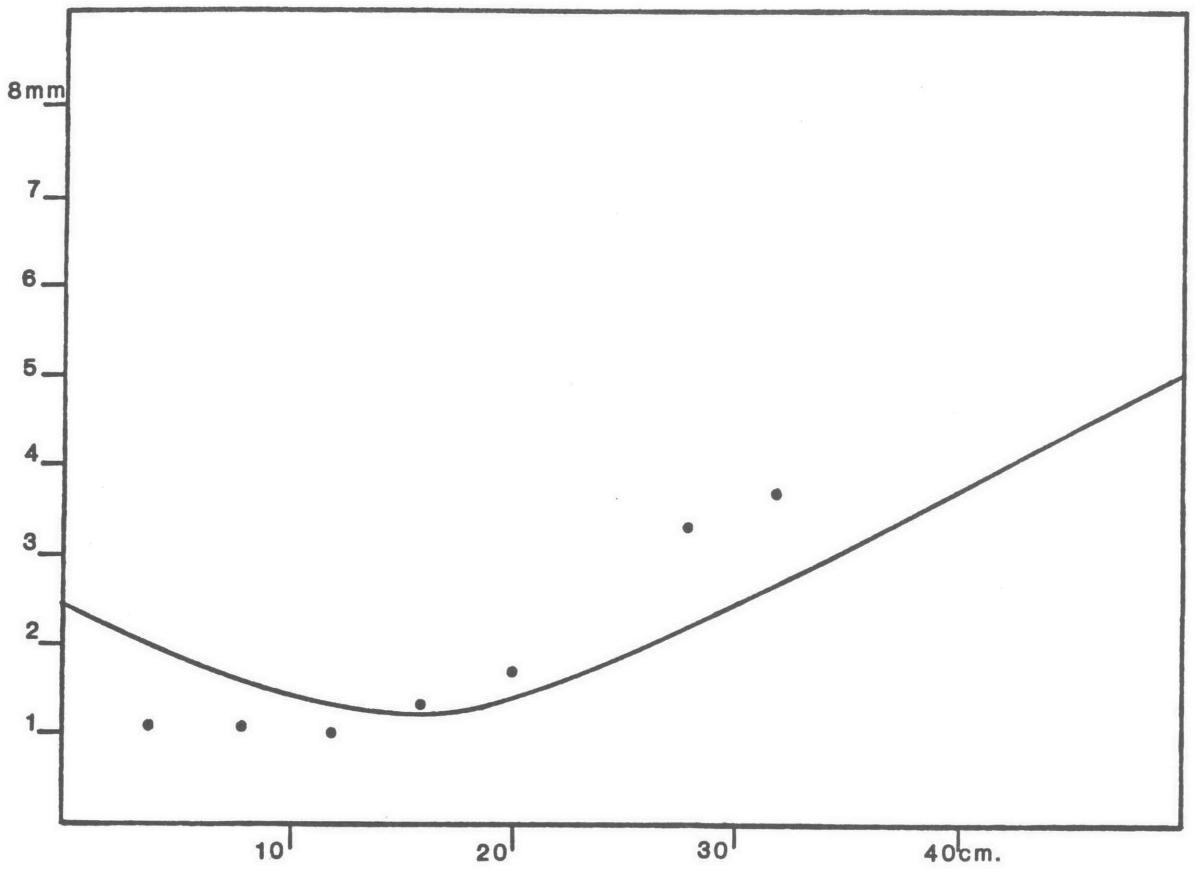


**Figure 4.3**
**Resolution as a Function of Distance**

The test pattern was placed at a distance of 22cm., and the edge was scanned across the field of view. Resolution measurements show the expected decrease in resolution off axis, with the blur size more than doubling near the far edge.

A target of 1 mm lines spaced 6 mm apart was imaged using the 1.5x30 mm aperture at optimum focus (Figure 4.4). This was compared to an image produced using a 1.5x5 mm aperture. The results are essentially the same, indicating that there is no significant loss in resolution due to the use of a rectangular aperture, while there is a sixfold increase in signal intensity.

It was noted that image contrast was very sensitive to the effect of flare- light entering the lens from non-imaged sources being scattered into the sensor array.

-Beam Imaging-

The line camera was used to image the Oxygen beam with the following beam parameters:

| | |
|---|---|
| BEAM ENERGY | 120 keV. |
| BEAM CURRENT | 25 ma. |
| GAS PRESSURE | 2.8 E-6 torr |

**BEAM PARAMETERS**

These beam parameters are expected to produce the lower limit of light intensity expected in practice. Visually, the beam was not easily detectable. The line scan camera was mounted on the vacuum chamber approximately 1.0m upstream of the wafer position. A simultaneous measurement was taken with a vertical wire scanner (Figure 4.5). The two scans agree on the general shape of the beam and the line camera scan does not show significant noise. The camera does not reproduce the intensity dip indicated by the wire scanner. This could be due to several reasons:

1) The image could contain a general background due to stray light bouncing around inside the optical system.
2) The region of light emission may extend outside of the actual beam volume by a small distance.

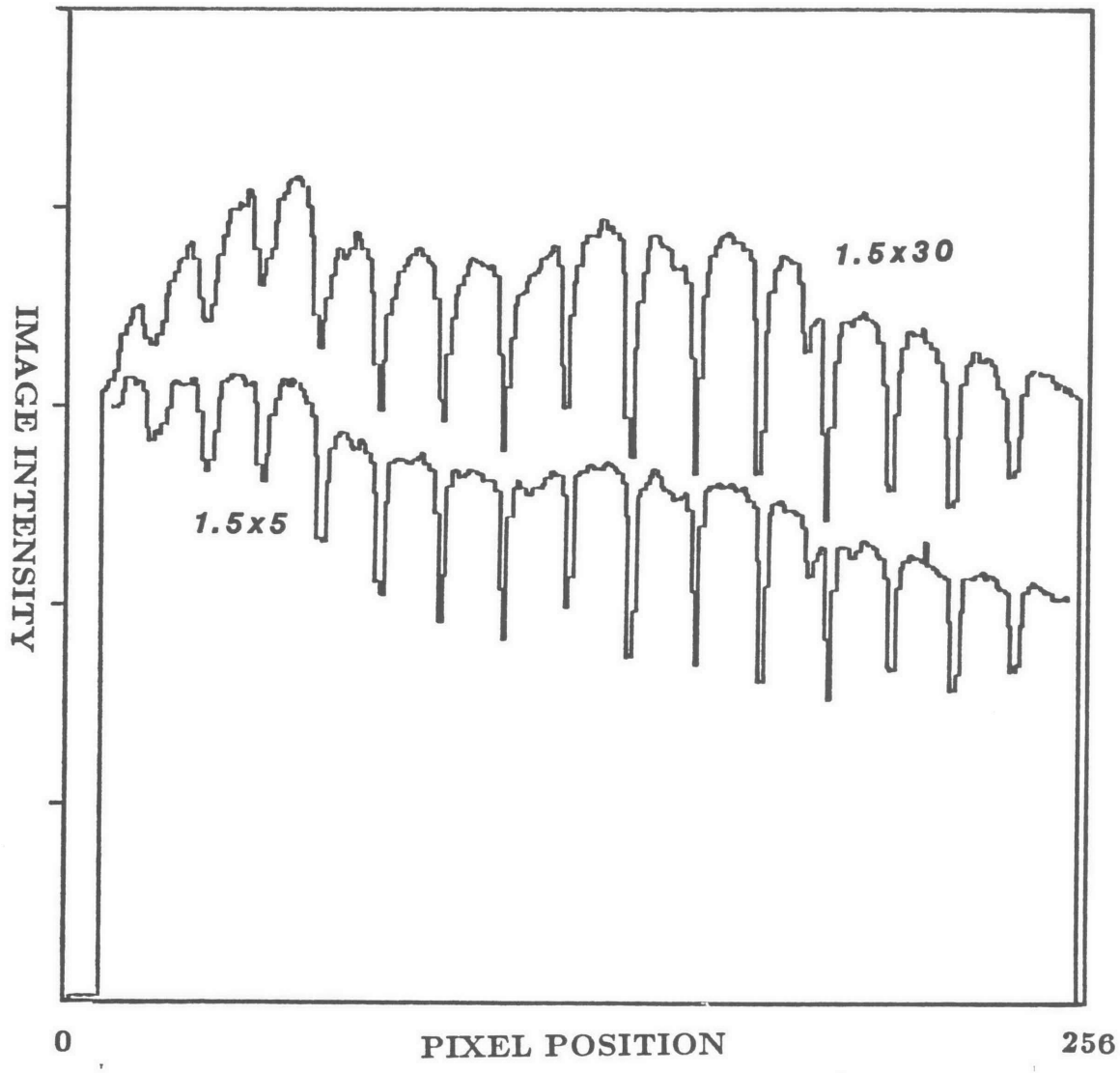


**Figure 4.4**
**Resolution Test Across Field at Optimum Focus**

3) The image differences may arise from the 'fan' geometry of the line camera vs. the parallel beam geometry of the scanner.

4) The wire scanner could produce erroneous results.

## TOMOGRAPHIC IMAGING

The creation of a cross-sectional view of the ion beam requires the acquisition of several views of the beam, each at a different azimuthal angle. A high quality image reconstructed on an N x N array requires, in general, N angular views spaced uniformly 180/N degrees apart. Each angular view should contain at least N lateral elements. Image quality acceptable for beam imaging purposes is probably available with the use of only 8 angular views; reasonably artifact free images can be produced on a 16 x 16 matrix. At least three methods have been proposed for the collection of multiple images. The first is the use of multiple fixed cameras. This has the advantages of mechanical simplicity, and collection time is minimized. The main disadvantage -the high cost of the line scanners- may tend to be offset by the lower price of the mounting equipment. The second method would have a small number of cameras mounted on a rotating gantry. The cameras would be rotated in sequence into multiple fixed viewing positions. The fixed positions would be similar to those of method 1. The third method is similar to method 2, in that it would also use a rotating gantry. In this case, the viewing positions would be continuously variable through the use of a transparent glass beam tube. This would allow the option of a large number of angular views, and therefore higher quality in the reconstructed image. One disadvantage of this method is the difficulty in producing a glass tube of sufficient optical quality.

## RECONSTRUCTION

The multiple one-dimensional angular views may be converted to a plane image through any of several reconstruction techniques. The three most common techniques are:

1) Algebraic Reconstruction Technique (ART)

2) Filtered Back Projection

3) The Method of Fourier Transforms

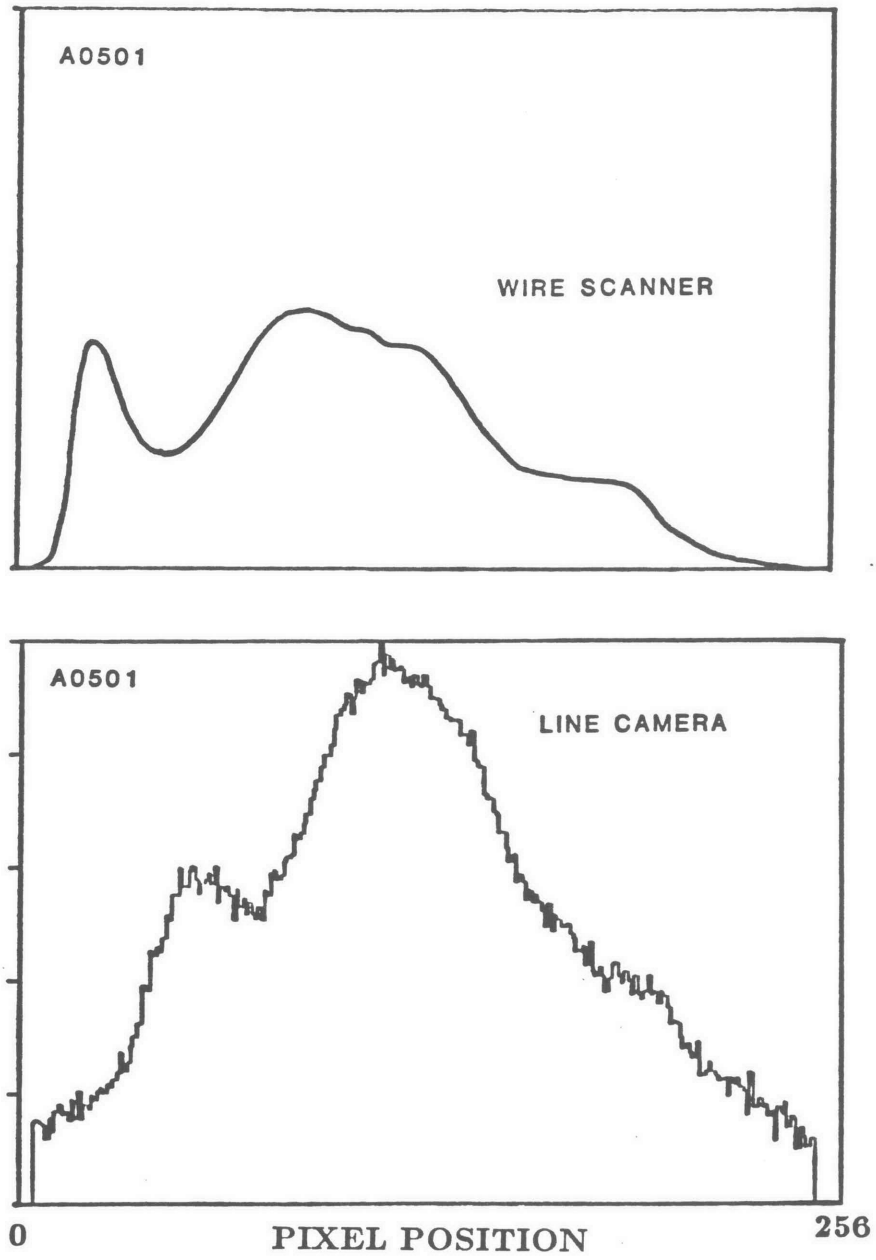


**Figure 4.5**
**Image of Minimum Intensity Ion Beam**

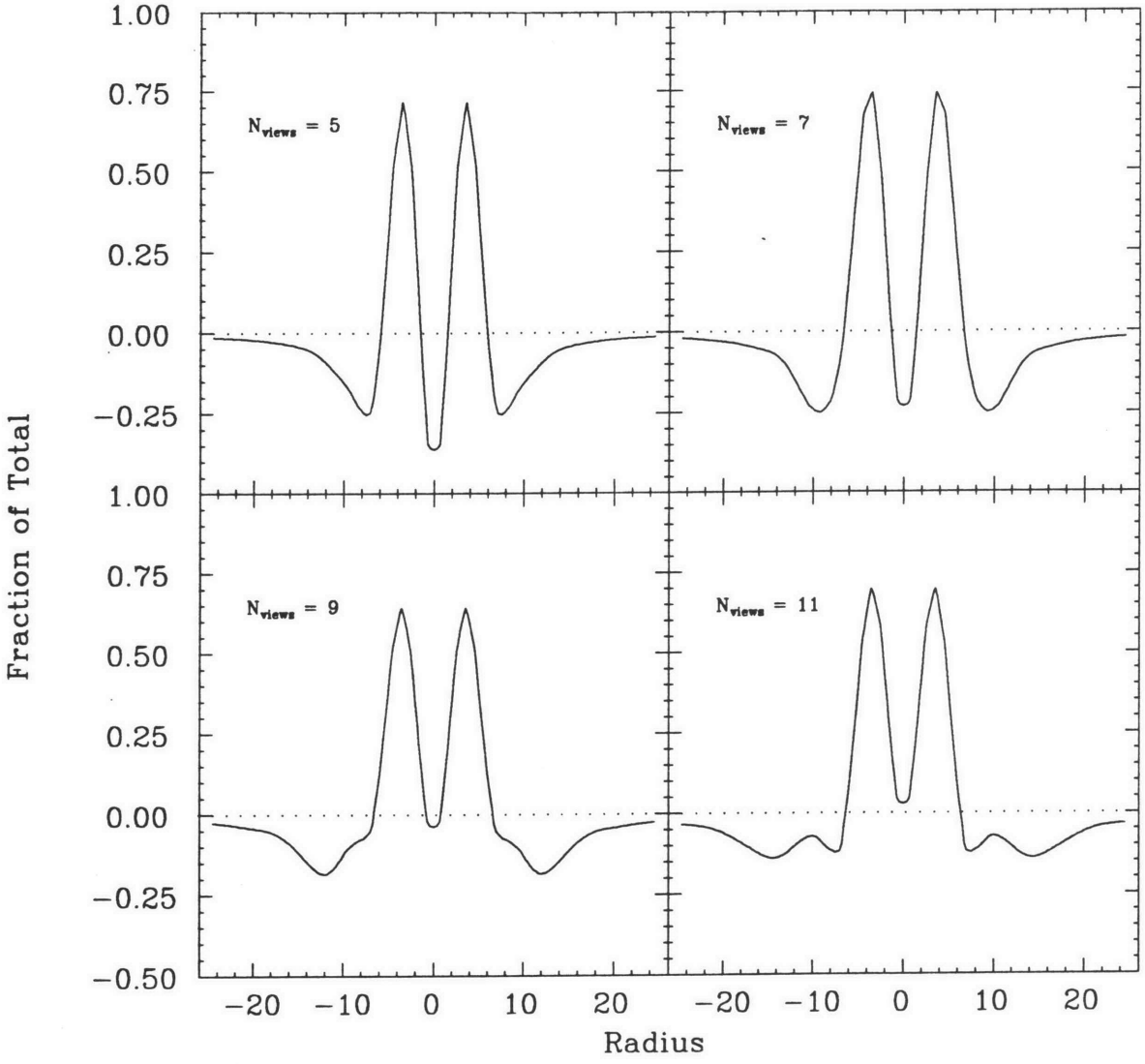


**Figure 4.6**
**Computer Simulation of Image Reconstruction**
**For Small Numbers of Views: Image Intensity**

There is no text material missing here.
Pages have been incorrectly numbered.

Page 83

Algebraic Reconstruction

ART works by making successive guesses at the original image, and comparing the projections of the trial image with the actual projection data. The difference between the trial projections and the data represents an error term and is added to the trial image. Through iteration, the technique approaches the original image. This technique works well with data that does not contain full angular coverage. It is slow, and has a tendency to diverge if left to itself.

Filtered Back Projection

The contributions are summed, and the resulting image is an approximation to the original image. If the projection is done with the raw data, a poor image will result. By first convolving the projections with a suitable filter function, the technique yields accurate images. This technique is faster than ART, and the reconstruction can be calculated as the data is collected, since each projection is treated independently.

Fourier Reconstruction

Instead of summing projections in image space, this method sums the projections in frequency space. The Fourier transform of the projection arrays are calculated, and these one dimensional transforms are projected across a two dimensional matrix at their corresponding angles. The resulting shape is two-dimensional inverse Fourier Transformed to produce the final image.

## RESULTS

The computer program IMAGE is capable of both Filtered Back Projection and Algebraic Reconstruction Techniques. The program was used to test the prototype tomographic system. The test was done with the use of a single line camera. The test object was made up of two 1cm diameter rods, one at the center of the turntable, and one at the edge of a 15cm circle. Multiple images were taken of the test object on a turntable at eight angles 22.5° apart. These images were then reconstructed into a two dimensional image. No attempt was made to remove the fan-shape distortion from the image. The result of a filtered back projection reconstruction yielded a clear image of the test object.

## COMPUTER SYSTEM

The imaging system is controlled by an LSI-11/23 microcomputer running the operating system RT-11. This combination combines powerful real-time capability with a simple, standard hardware interface. The processor has seven levels of interrupt priority; for this application, only a single level of priority was used. Two peripheral boards were used, both DEC standard, and both available from third party sources. The KWV-11 board is a general timing function board. In addition to a programmable timer, the board includes two channels each of digital pulse input and output. This board is used to provide the basic clock frequency for the camera system. The two output lines provide the CLOCK OUT and START signals to the camera. The AXV-11 board is a multiplexed 16 line A-D converter. It has a 12 bit resolution, and a maximum conversion rate of 50kHz. The resolution is about right for this application, although 10 bits would be useable. The maximum conversion rate is in practice limited by the processor speed; because of the data manipulation necessary, an effective collection rate of about 3kHz was realized. At this rate, a 256 pixel array can be converted and stored in 80msec. It was not necessary to convert even at this speed; actual scans required integration times on the order of one second to achieve an acceptable signal.

The AXV-11 also includes two 12-bit D-A converters. These were used to drive a pen plotter for data output. Data was displayed on a DEC VT-241 CRT. This terminal is able to emulate a Textronix 4014 vector terminal, and this Textronix mode was used to draw line graphs of the data. The terminal is capable of producing 4 colors or shades of gray- this is probably not enough for a proper display of two-dimensional intensity maps, and down-loaded gray scale graphics are probably necessary.

## ADDITIONAL HARDWARE

Additional hardware include buffer electronics to go between the KWV-11 unit and the array driver. The clock pulse is buffered with a pair of 7404 digital inverters to insure adequate signal fan-out. These could be replaced with differential line drivers for increased noise immunity. The start pulse is buffered through a 74121 Monostable in order to provide a start pulse that will span at least one full cycle of the clock signal. The pulse width is now varied with a potentiometer, and has been set to a width exceeding the longest clock cycle in use. This should be replaced with a properly synchronized and clocked latch circuit for obvious esthetic reasons. Power

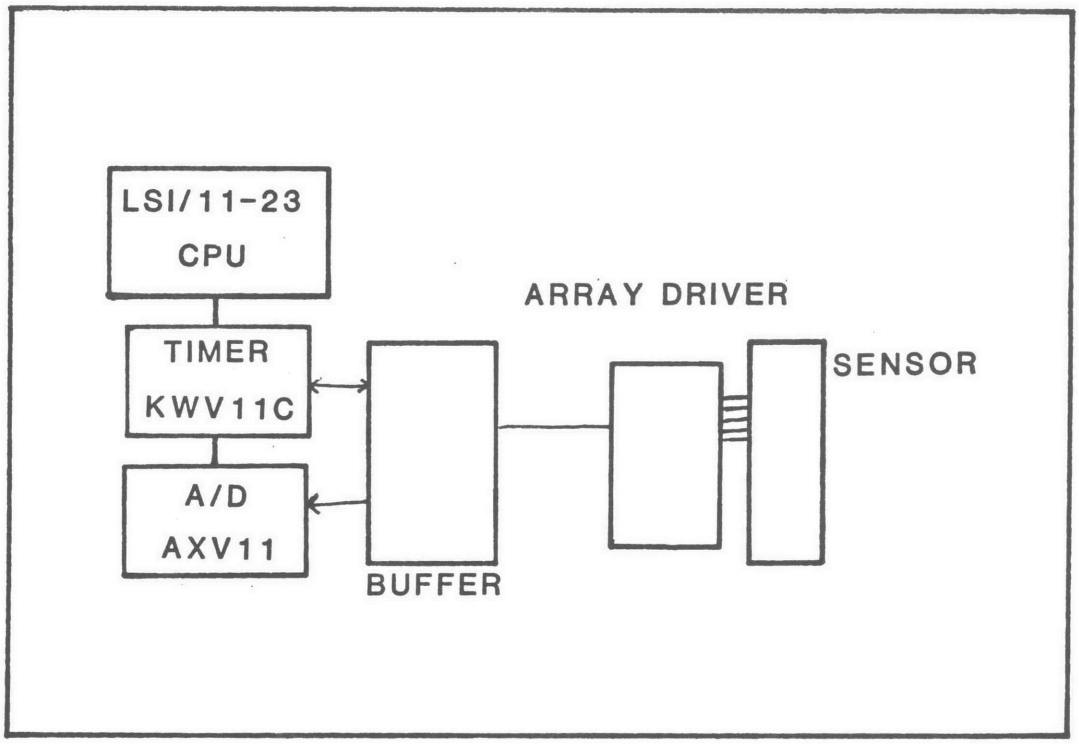


**Figure 4.8**
**Data Acquisition and Analysis**

supply and timing signals are carried to each camera through a single unshielded 6-conductor cable, with a single ground return. The data signal is transmitted through a 50 ohm coaxial cable. The camera body is electrically insulated from the beam line. A single coaxial ribbon cable should probably be used, with short lengths connecting the individual cameras.

# APPENDIX A
## Limits on the Design of the NSLS Microprobe Optical System

SYSTEM OVERVIEW:

The NSLS synchrotron microprobe beam design must attempt to satisfy the requirements of many users [Ho82]. Ideally, the monochromated beam would have a small divergence, high intensity, and a spot size ranging from a few hundred microns to less than one micron. A simple one stage system does not have the flexibility to allow trade-offs between these requirements. We have therefore decided on a two stage demagnification of the beam.

The first stage will include a channel cut monochrometer and a high acceptance lens focussing the beam to a 37$\mu$m. spot. The primary lens element will be a single grazing incidence ellipsoidal lens with a magnification factor of 1:8. Calculations indicate that we can expect a horizontal acceptance of 1.0 milliradians and a vertical acceptance of 0.17 milliradians. The lens will be coated with platinum and accept a grazing angle of up to 5 milliradians and so allow focussing of x-rays up to 17 keV. Uses which require only moderate resolution will be done at this focus. Smaller beam sizes will be obtained at this point through the use of defining pinholes. It is anticipated, however, that pinholes will prove unacceptable for important classes of experiments, in which cases the primary focus will be the object for a second stage of 1/8 magnification. If beams smaller than $\approx$ 3 microns are required, it will be possible to produce such beams at the secondary focus by the use of a field stop at the primary focus. The problems associated with slit scattering from apertures with high aspect ratios would no longer be a limitation, as they would be if the primary beam were used without re-imaging. The real limitation will probably be the precision of the secondary focussing element. A resolution of one micron, for example, would require the product:

slope error * image distance

be less than one micron. A typical slope error for a high quality small mirror is about 5 microradians. With such a mirror we would need an image distance of less than 20 centimeters from the upbeam end of the optics to provide 1 micron resolution.

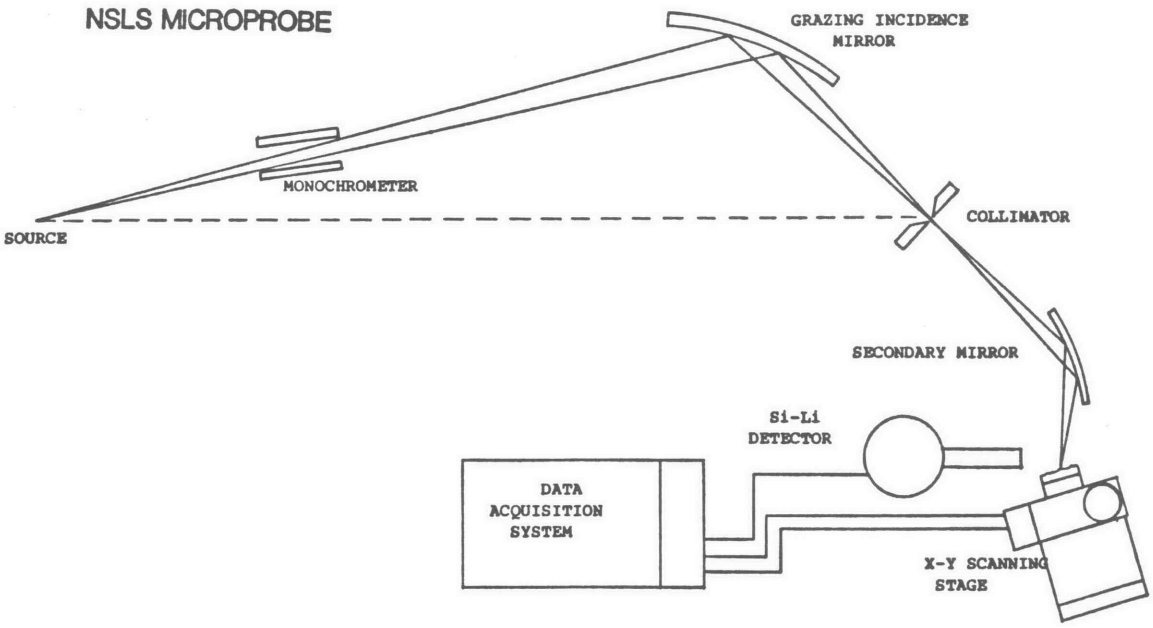


**Figure A.1**
**Components of NSLS Microprobe**

The requirement of a short image distance precludes the possibility of using a second ellipsoidal mirror as the focussing element in the second stage since such a lens would have too small a radius of curvature to be feasible. A practical second stage element is, however available in the Kirkpatrick-Baez lens, which uses two perpendicular cylindrical mirrors, each with a large radius of curvature. Such a lens could provide a magnification of 1/8 , giving a 1/64 total reduction of the synchrotron source.

PRIMARY STAGE:

The use of grazing incidence mirrors to focus x-rays is well documented [Ho82,Ic82]. Several geometries have been used, including the Kirkpatrick-Baez, toroidal, ellipsoidal, and the ellipsoid-hyperboloid pair. Frequently, the design intent is to produce the image of an extended x-ray source. In such instances, considerations of flatness of field and field of view are important. For the purposes of a microprobe, all that is desired is point to point focussing. The ellipsoid of revolution is ideally suited for this, and has the practical advantage of being a single element device.

The geometry of the ellipsoidal mirror can be described using three parameters- the major and minor axes and the location along the arc of the ellipse of the mirror section (Figure A.2). An equivalent set of parameters is the object distance R, the magnification factor M ($M = R'/R$) and the grazing angle $\Theta$. Specification of these three parameters determines a section of a unique ellipsoid of revolution. For a given application, a maximum value of the grazing angle is fixed by the range of x-ray energies that will be used and by the composition of the reflecting surface. This leaves two adjustable parameters- the object distance(R) and the magnification factor(M). Any lens with a given grazing angle may thus be characterized by a point on the R vs. M plane. Figure A.5 is a plot of R vs. M for the NSLS microprobe lens. The shaded area contains all combinations of R and M which satisfy the constraints discussed below.

For most applications, the magnification factor is required to be as large as possible, within any practical constraints on the working distance. In fact, there are further constraints on the choice of both M and R. These include the tolerances to which optical surfaces can be manufactured, as well as the minimum required horizontal and vertical acceptances of the optical system.

The requirement of a small grazing angle and reasonable working distance leads to an ellipse with a minor axis of the order of a few centimeters, and a major axis of

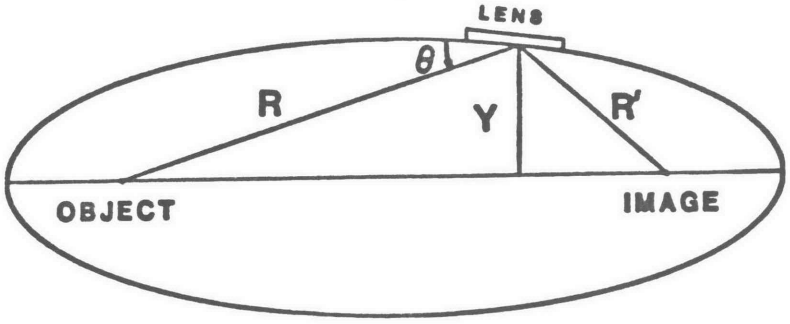


Figure A.2
Ellipsoidal Mirror Geometry

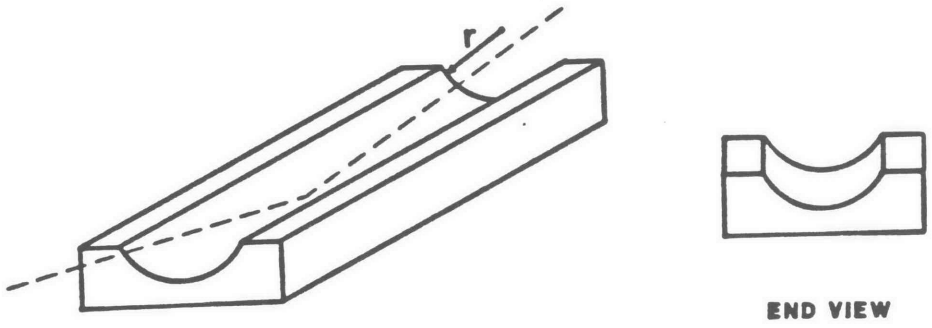


Figure A.3
Ellipsoidal Mirror

the order of a few hundred centimeters. The length of the mirror is governed by the maximum permissible deviation of the grazing angle from optimum and is discussed below. The shape of the final mirror is shown in Figure A.3.

Errors in the production of the theoretical optical figure are the most direct limitation on the final spot size. Slope error is the deviation of the slope of the optical surface from its correct value. A random distribution of such errors over the optical surface will lead to a finite blur circle centered at the theoretical image point. This blur circle must be convolved with the image produced by a perfectly formed mirror to determine the actual size of the image spot.

The effect of the slope error can be resolved into components parallel and perpendicular to the beam direction; the two components do not contribute in the same way to the blur circle. Figure A.4 shows that the parallel slope error $dq$ leads to a displacement of the incident ray of:

$$dl = R' * 2dq$$
$$dl = MR * 2dq$$

The perpendicular error d$\rho$ displaces the incident ray along the cone defined by the incident beam direction and $2\Theta$. This means that for a typical grazing incidence mirror, the permissible perpendicular slope error is $1/2\Theta$ times larger than the parallel slope error:

$$ds = R' * 2\Theta d\rho$$
$$ds = MR * 2\Theta d\rho$$

It is reasonable in the case of a source of fixed size such as a synchrotron, to express a maximum permissible blur circle as a fraction $f$ of the ideal image size $A * M$, where $A$ is the size of the synchrotron source. Thus, the relative blur:

$$f = dl/(AM)$$
$$f = 2 * dq * R/A$$

Given some maximum acceptable blur fraction, this leads to a constraint on the object distance R:

$$R = fA/2 * dq$$

Thus, when the blur circle is expressed as a fraction of the image size, the object distance is independent of the magnification factor M as indicated by the horizontal line in Figure A.5.

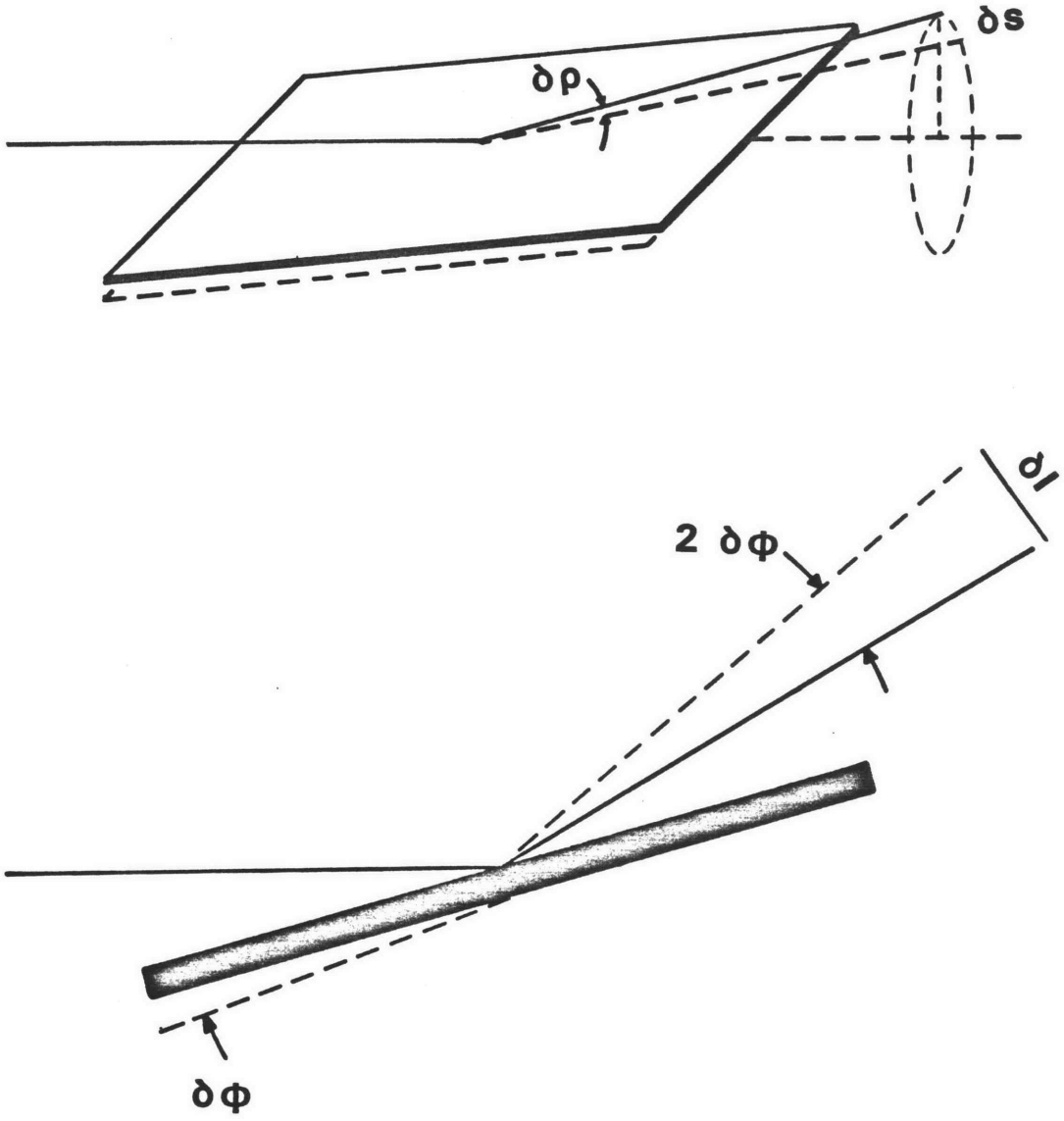


**Figure A.4**
**Parallel and Perpendicular Slope Errors**

The production of lenses with a small radius of curvature is difficult, and so there are practical limits on the radius of curvature in the direction perpendicular the beam. This radius is given by the distance from the center of the lens to the axis rotation (see Figure A.2):

$$r = Y_0 = \frac{RR'sin2\Theta}{(R2 + R'2 + 2RR'cos2\Theta)^{1/2}} \qquad (A.1)$$

for $\Theta << 1$,

$$r = 2\Theta R/((1/M)^2 + 2/M + 1)^{1/2}$$
$$r = 2R\Theta/((1/M) + 1)$$

For a constraint of a minimum r, this leads to a constraint on the magnification M:

$$1/M = (2\Theta R/r) - 1 \qquad (A.2)$$

This is shown in Figure A.5 as the slanted line. The area bounded by the constraints on M and R is the region of constructable lenses, and the intersection of these lines is the lens of highest demagnification.

The optical aperture of the lens as seen by the grazing incidence beam is shown in Figure 3. It is apparent that the horizontal dimension of the lens may not be expanded indefinitely since it is limited to twice the rotation radius (r) of the ellipsoid. The maximum horizontal angular acceptance of the lens is thus determined by this radius and the object distance:

$$h = 2r/R$$

$$h = 4R\Theta/(1/M) + 1 \qquad (A.3)$$

In practice, the construction of a lens with this maximum acceptance angle would be difficult, and so the acceptance is likely to be less than the limiting value.

The vertical dimension of the optical aperture is determined to first order by the length of the lens and the grazing angle (Figure 3):

$$\text{vertical dimension} = L\Theta$$

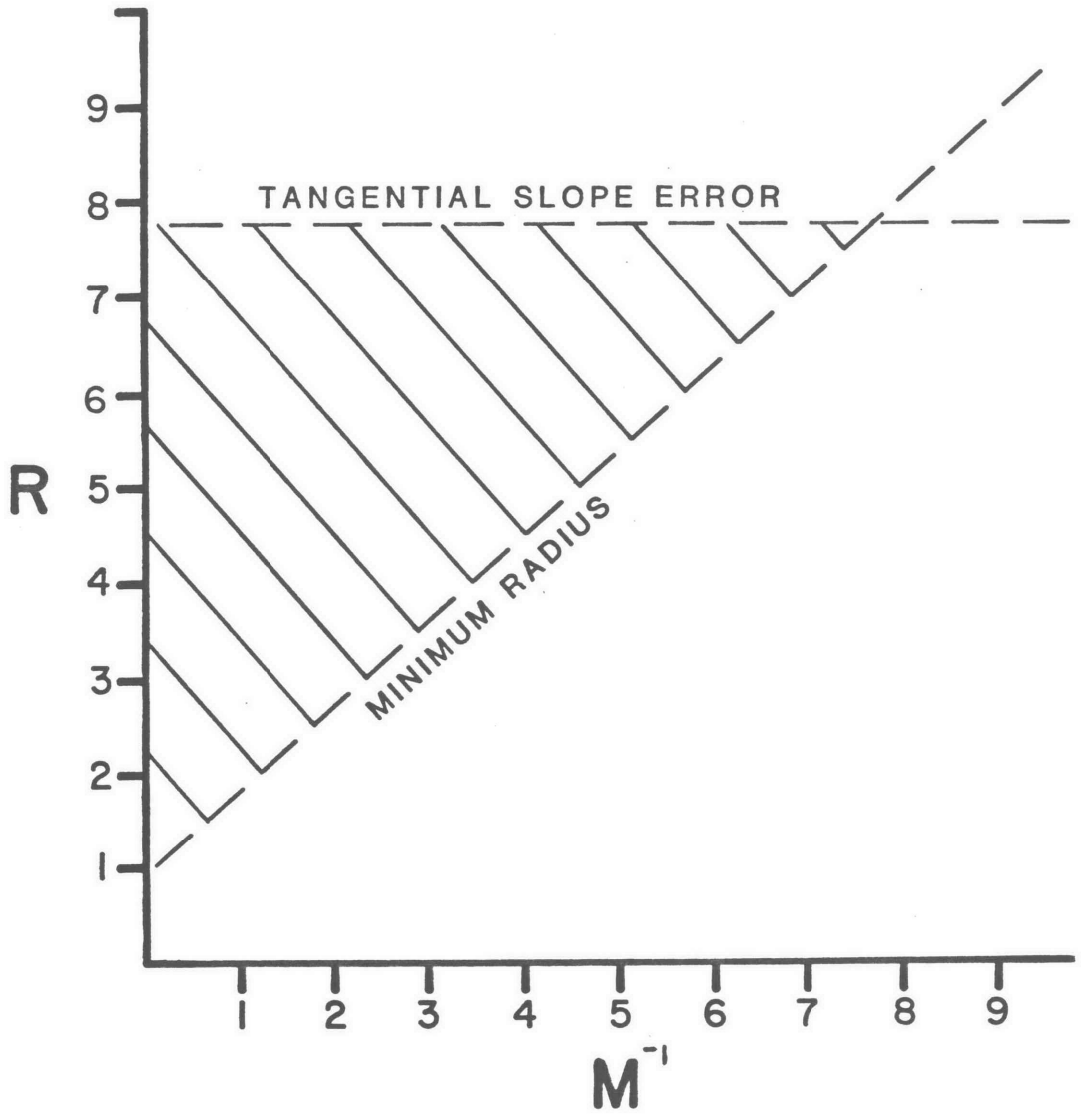


**Figure A.5**
**Constraints on Lens Parameters**

The vertical angular acceptance is given by:

$$v = L\Theta/R \qquad (A.4)$$

The above equation assumes that the lens is essentially flat in the long direction- an assumption that is true to first order for short lenses.

The length of the lens cannot be extended indefinitely. One consideration is that it is more difficult to maintain close tolerances on a longer lens. A second consideration is that the grazing angle at the ends of the lens is larger than at the lens center. For a given x-ray energy, the effective length of the lens will be the length of the section for which the grazing angle is less than the critical angle for that energy. The effective length, and therefore the effective vertical acceptance, is thus dependent on the energy of the incident beam. In the case of the microprobe lens, we required that the grazing angle at the ends of the lens not exceed 5.4 mrad. This requirement was satisfied by a length of 28 centimeters.

The ellipsoidal mirror focuses a point source at one focus to a point image at the other. In the case of an off axis point source, the image produced is not an off axis point image, but rather an arc centered on the optical axis. The radius of the arc is equal to the magnified displacement of the point source. If the lens is a full figure of revolution, the arc is a circle. For a lens that subtends a smaller angle of revolution, the arc will subtend that same angle. It is clear that an extended source may suffer from significant distortion.

The synchrotron source is an extended source, and it is necessary to determine what effect this has on the final image. A raytrace program was used to determine the aberrations of a perfectly made ellipsoidal mirror. The shape of this mirror was determined using the tolerance considerations that we have outlined. The object source used in the raytrace analysis was a rectangle with dimensions similar to the size of the NSLS. It was determined that the synchrotron source will be imaged without significant distortion if the horizontal acceptance angle is less than 1.0 milliradian.

CONCLUSIONS:

The ability to demagnify a pointlike source, such as a synchrotron beam, is under some conditions determined by how well the lens is made, and not by the inherent

properties of the ellipsoidal geometry. Once the limiting manufacturing tolerances are estimated, the optimum lens parameters are determined. Listed below are the constraints that were used in designing the lens. Of these, the minimum radius of curvature and tangential slope error are manufacturing tolerances. These were to some extent a matter of cost, but it would be difficult to have a lens with significantly better tolerances made for any reasonable price at the present time. The remaining constraints were our minimum requirements for a useful scientific instrument. Values of M and R based on these figures are also listed, along with the actual final parameters for the lens.

## Performance Requirements

| | | |
|---|---|---|
| Object Size | A | 300x1200 microns |
| Grazing Angle (center) | Θ | 5.0 milliradians |
| (ends) | | 5.4 milliradians |
| Relative Blur Circle | f | 1/4 |

## Manufacture Constraints

| | | |
|---|---|---|
| Maximum Tangential Slope Error | dq | .005 milliradians |
| Minimum Radius of Curvature | r | 1.0 centimeters |

## Final Results

| PARAMETER | | OPTIMUM | ACTUAL VALUE |
|---|---|---|---|
| MAGNIFICATION | M | 1/7.7 | 1/8 |
| OBJECT DISTANCE | R | 780 | 800 centimeters |
| HORIZONTAL ACCEPTANCE | h | 2.5 | 0.5 milliradians |
| LENGTH | L | | 20 centimeters |
| VERTICAL ACCEPTANCE | v | | .17 milliradians |
| SEMIMAJOR AXIS | | | 450 centimeters |
| SEMIMINOR AXIS | | | 1.4 centimeters |

# APPENDIX B
# ION INDUCED X-RAYS FOR X-RAY FLUORESCENCE ANALYSIS

L. Grodzins and P. Boisseau

## SUMMARY

Energetic ions bombarding pure element targets induce characteristic x-rays with high probability and with negligible bremsstrahlung background. The cross sections for x-ray production by protons reach $10^3$ b and heavy ions attain cross sections $Z^2$ times higher. Small accelerators can produce monoenergetic x-rays from 1 to 20 kev with fluxes in excess of $10^{10}$ /sr/$\mu$A of protons; heavy ion accelerators can achieve one to two orders of magnitude more. These Ion induced x-rays can be quite effective for X-ray induced X-ray fluorescence. For bulk samples, the method of IXX is as sensitive as PIXE itself; for many elemental analysis problems IXX may be the preferred technique. IXX enjoys the advantages of the widely used conventional x-ray induced x-ray fluorescence techniques; lighter constituents in heavy matrices can be effectively studied; liquid, even living targets can be used; heating and radiation damage are minimal; absolute quantitative analysis is straightforward even for oddly shaped samples. Focussed x-ray beams can be produced with considerably less background than can be obtained with EXX. IXX should be a valuable addition to the arsenal of analytic techniques available with present ion accelerators. We also remark that IXX facilities using stored beams of 20-30 MeV protons could produce monochromatic photon intensities of $10^{14}$ photons/sr/kW of power dissipated in the target. Such beams could be developed into x-ray probes competitive with any other technique for elemental analysis of small samples.

## INTRODUCTION

Electron induced x-ray fluorescence has been developed into a powerful tool for elemental analysis of minor constituents. In the early 1970s it was realized that proton induced x-ray fluorescence could be more effective than electrons for trace element analysis since the background is orders of magnitude less intense with an ion than with an electron beam [Jo70,Fo74]. The improvement in elemental sensitivity by two to three orders of magnitude has led to the wide acceptance of PIXE techniques for bulk [Jo76] and microprobe analysis [Co79]. The third well-developed method for inducing characteristic x- rays uses monochromatic incident photons whose energy is not too far above the binding energy of the electrons in the sought-for element [Mu72]. If the detector of the characteristic x-rays can exclude or suppress the Compton and

Rayleigh scattering from the target, then x-ray induced x-ray fluorescence is orders of magnitude more sensitive to trace elements than is PIXE. The distinct merits and drawbacks of these three techniques have been much discussed in the literature [Go77,Sp80]. For our purposes it is sufficient to note that the intrinsic sensitivities of the techniques span a range of some six orders of magnitude with electron induced x-ray fluorescence at the one part in $10^{4-6}$ level, monochromatic photon induced fluorescence (XX) at the one part in $10^{8-10}$ level, and proton induced x-ray fluorescence in between [Gr]. These intrinsic sensitivities are, however, seldom realized in practice due to limitations in obtaining a sufficient signal strength in the face of target heating and radiation damage or limitations in available fluences. Overall, however, there is general agreement that, in principal, the XX technique is the method of choice for x-ray induced fluorescence since it results in the highest theoretical elemental sensitivity accomplished with the least heating or radiation done to the sample.

At the present time there is widespread use of electron beams for the generation of such x-rays. The x-ray tubes used for such EXX studies are relatively inexpensive and quite powerful. Small EXX units are in routine use for bulk analysis at the parts per million range of sensitivity[Go77]. Commercial sources delivering 10 kW of beam power are available which can, for example, produce $10^{15}$ /s/sr of Cu x-rays and substantially improve the sensitivity of the EXX technique through the use of wave-length dispersive detectors, but such sources are not in wide use. The instrument which comes closest to fulfilling the ideal generator for x-ray induced x-ray fluorescence is the dedicated synchrotron radiation sources proliferating throughout the world. Intensities of monochromatic (dE/E = 1%) x-ray beams will exceed $10^{14}$ /s/msr and focussed beam densities exceeding $10^{10}/\mu m^2$) are expected to be available [Sp80]. With these tunable, monoenergetic beams it will be possible to carry out XX studies at high spatial resolution and at the theoretical sensitivity limits ($\leq 10^{-9}$g/g) and do so with minimum target heating or radiation damage to the samples [Sp80,Gr,Go].

This paper discusses the merits of generating x-rays for XX studies through the use of energetic proton and heavier ion beams. Shortly after the BAPS abstract was submitted we were informed of recent work on the same subject [Pe] carried out by Peisach's group in South Africa who were exploiting the fact that lighter elements in heavier hosts can be selectively observed with the proper choice of x-rays produced in proton bombardment. And a few weeks ago we received a preprint from a Birmingham group who are exploiting the advantages of IXX techniques for studying biological samples [Ma]. Their paper referenced the work of Lin et al of Taiwan who, in a 1978

paper, called the technique PXX, for proton induced x-rays for x-ray fluorescence [Pe]. The IXX wheel has in fact been reinvented many times; a careful evaluation was carried out in the early 1960's, before the development of high resolution, high counting rate x-ray detectors [Bi63]. Birks concludes his study of electron, proton and photon sources for XX studies with the statement that "If a low-cost proton source could be found, it would have considerable advantage over electron excitation because of the reduction of background interference."

The technique of IXX should be better known. We begin by reviewing XX, the analytic determination of elements using beams of monochromatic photons in order to emphasize the important connection between fluence and sensitivity.

## PROTON INDUCED X-RAY FLUORESCENCE

Consider the expected distribution of radiations in the study of zinc and lighter elements in a carbon host using 9.886 kev K x-rays. The induced radiations, per $10^{12}$ incident fluence per mg/cm$^2$ or target thickness, are given in Figure B.1. The solid angle efficiencies and energy resolutions are nominal values for energy and wave length dispersive detectors. The signal strengths are for one atom of Zn, Cu, Ni, Co and Fe, per million atoms of the host. (The cross sections for K x-ray fluorescence using a 9.886 kev beam, range from 9000 b for zinc to 3000 b for iron.)

The left panel of Figure B.1 shows the expected radiation in a solid state detector; the incident x-rays are unpolarized. A number of trace elements are measured simultaneously. The sensitivity is limited to about one part per million by the imperfect collection of the total energy into a single peak in the detector [Go77]; the resulting tails of the Compton and Rayleigh peaks are shown schematically in Figure B.1. An order of magnitude gain in sensitivity to Ni and Cu can be realized if a critical absorber of Zn is interceded between the target and the detector. However, the critical absorber rapidly reduces the sensitivity to the lighter elements. Nevertheless, the use of Si-Li detectors can give sensitivities well below a part per million for medium weight trace elements in light matrices.

The middle panel is similar but the incident radiation is from a synchrotron. As a consequence of the polarization of the x-ray beam in the synchrotron plane, the Rayleigh and Compton scattering are suppressed at 90° to the beam. The reduction of the tails of the elastic and inelastic peaks, by about a factor of 100, results in a

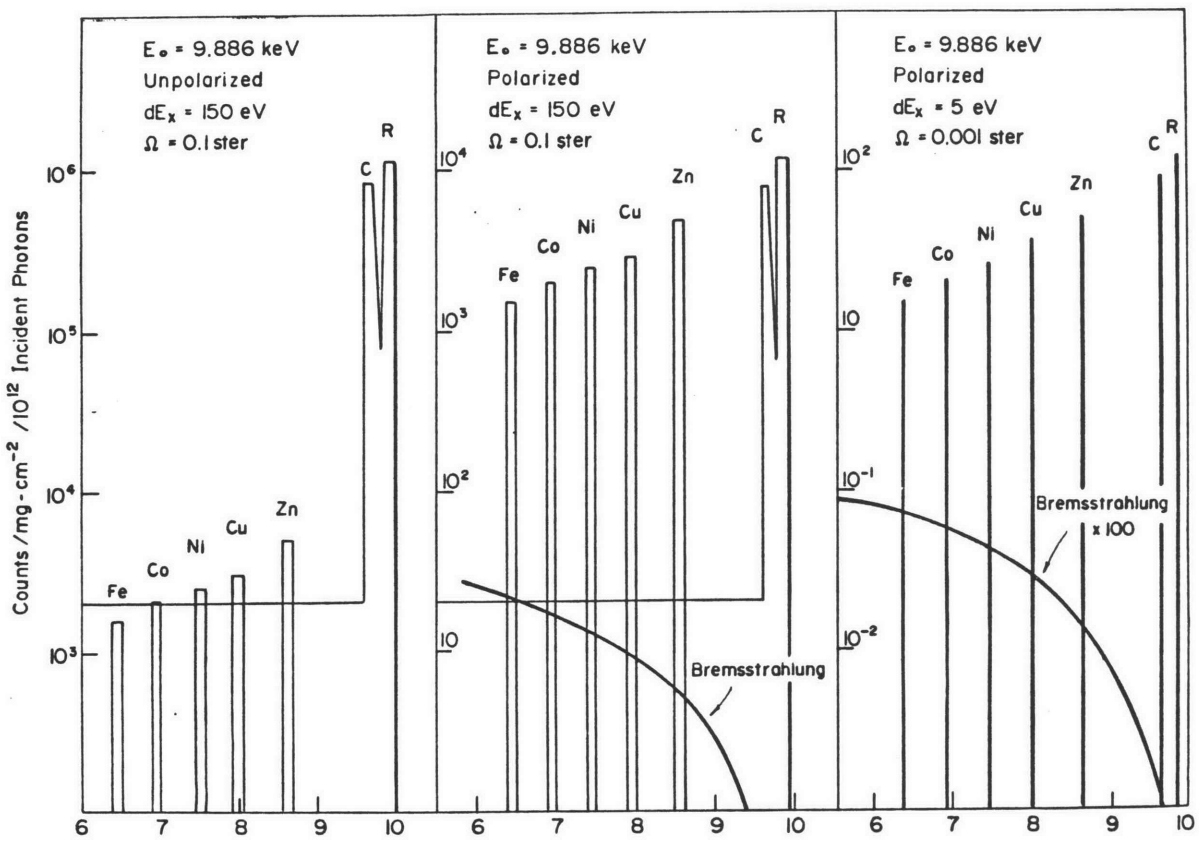


**Figure B.1**

**The X-ray induced radiations in a carbon sample containing one atomic part per million of Fe through Zn; counts versus x-ray energy. Left panel: incident radiation unpolarized, solid state detector. Middle panel: incident radiation polarized. Right panel: wave length dispersive detector.**

corresponding gain in sensitivity, into the parts per billion range even when solid state detectors are used.

The ultimate sensitivity is reached with the use of wave-length dispersive detectors whose resolution is comparable with the natural line width [Gr]. Bremsstrahlung from photo-electrons is then the only background, apart from ambient radiation. The expected spectrum is shown in the right panel of Figure B.1; the bremsstrahlung intensity has been multiplied by a factor of 100. The signal to noise ratio is, in principle, independent of the polarization of the incident beam; for convenience of scale the Compton and Rayleigh scattering are shown for a polarized beam. The sensitivity of XX exceeds one part per billion for all the elements shown. But the high sensitivity has been achieved at a great cost in signal. A fluence of $10^{12}$ results in a signal of 50 counts when the one mg/cm$^2$ carbon sample contains one part per million of Zn. Clearly, to obtain a signal when the trace concentration is a part per billion - - and the background is still negligible – requires a fluence on the target of $\approx 10^{15}$.

In summary, photon induced x-ray fluorescence is in principle capable of sensitivities at the level of $1{:}10^{10}$ ; even a heavy matrix such as iron does not worsen the intrinsic sensitivity below about 10 parts per billion for most element/sample systems. (8) However, and it is a big however, the fluence on the target in excess of $10^{15}$ , which appears necessary to attain these sensitivities, is beyond the present capabilities of all but the most powerful synchrotron radiation sources. With other x-ray sources it pays to trade energy resolution for solid angle in order to retain sensitivities below a part per million with fluences of the order of $10^{12}$ . Energetic ion beams from existing accelerators can produce such fluences in modest times.

## ION INDUCED X-RAYS

The cross sections for heavy ion induced x-rays have been measured over wide ranges of the projectile-target combinations and projectile energies. (10) For our purposes it is sufficient to emphasize that:

The cross sections for x-ray production by protons follow a universal curve which scales according to the binary encounter model. (3)

The maximum cross sections for x-ray production by protons is reached at about the matching velocity; that is, when E eV, where A and Z are the atomic weight and number of the target atom and m is the mass of the electron; the cross section

for x-ray production in Fe peaks at about $10^3$ barns at a E 20 MeV. The energy at matching velocity is generally greater than the Coulomb barrier energy, the natural limit for PIXE studies; above it the nuclear reaction gamma rays unduly burden the energy dispersive detectors normally used. The Coulomb barrier is not a limit with IXX since the x-ray detector can be well shielded from the production target and the primary x-rays are being produced by the matrix atoms of the target and not by a trace impurity.

Molecular orbital effects can substantially increase the binary encounter cross section especially at lower velocities [Ga70]. These enhancements, which can be important in thick target yields, are ignored here.

It is obviously not necessary to consider L x-ray production and it is not useful to consider K x-ray production from elements much greater than about Sn(Z=50); it is almost always possible to find the appropriate K x-ray from a lighter target which will selectively ionize the L3 edge of the heavier sample atom so that only a two line x-ray spectrum is observed.

Calculations of x-ray production were carried out for both thin and thick targets and for both reflection and transmission geometries. Only the reflection geometry is considered here since it yields the higher intensities.

The K x-ray yields expected from the bombardment of thick targets by one microampere of energetic protons are given in Figure B.2. Targets range from Z = 10 to 50. Three fixed proton energy curves, of 2, 4 and 6 MeV, are shown as well as two variable energy curves, corresponding to the Coulomb barrier energy of the sample nucleus and to the proton energy which yields the maximum ionization cross section. Protons of 4 MeV available from the typical small electrostatic accelerators induce more than $10^{11}$ characteristic K x- rays per microampere of beam over the range from Z=10 to Z$\approx$ 30 i.e. from about 1 to 9 kev. The yield of 17.4 kev K x-rays from a Mo target is more than an order of magnitude smaller. Larger accelerators can produce maximum yields over the entire range of interest

A heavy ion is a more effective inducer of atomic ionization than is a proton. Figure B.3 shows the yields expected for H, Li, C and O beams under three conditions. The left panel is for a thin target, 0.1 mg/cm thick with the beam energies at the Coulomb barrier of the target nuclei. For the lighter nuclei, the production gain is a factor of Z . For the heavier elements, the gain is substantially less since the velocity

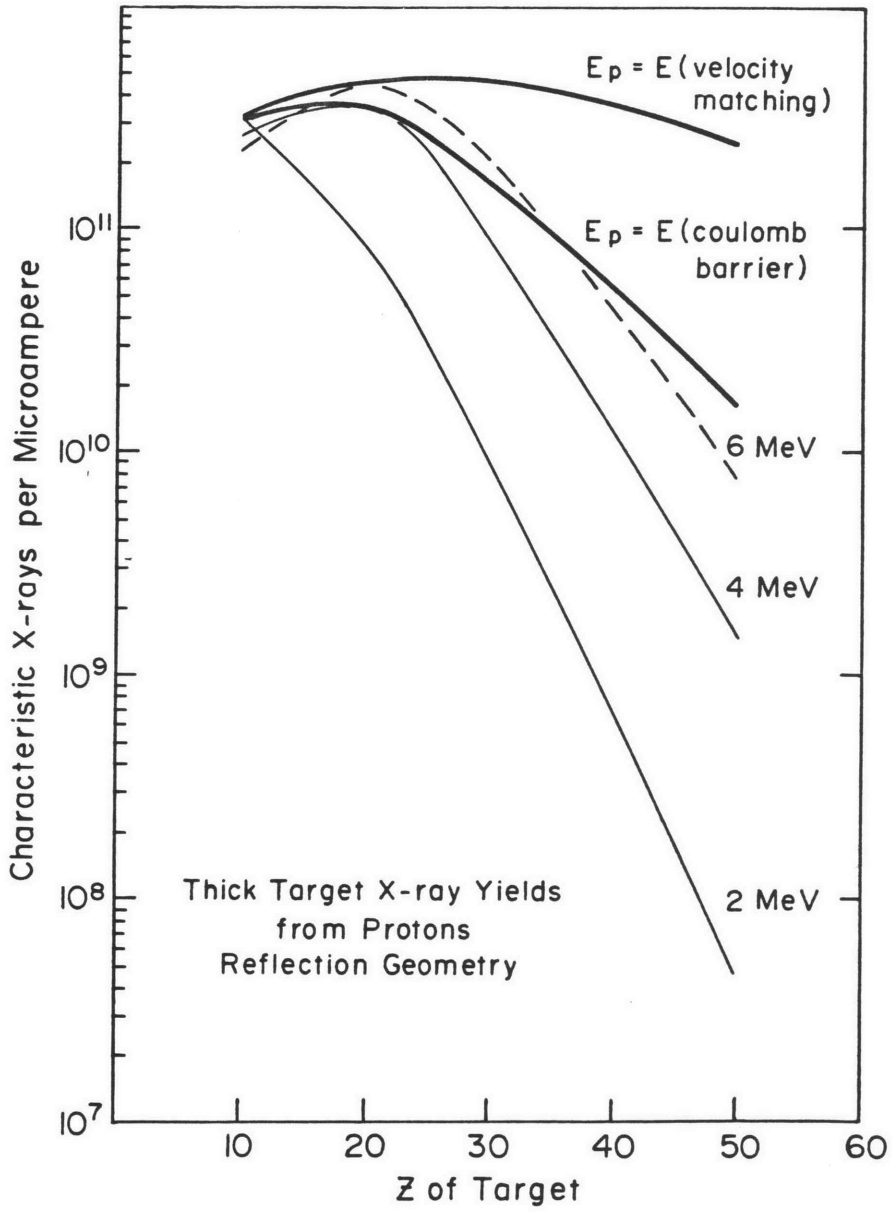


**Figure B.2**

**Thick target x-ray yields for protons. The cross sections for x-ray production scale as the square of the atomic number of the projectile. Neon beams have 100 times the cross section for ionizing than do protons of the same velocity [Ga78].**

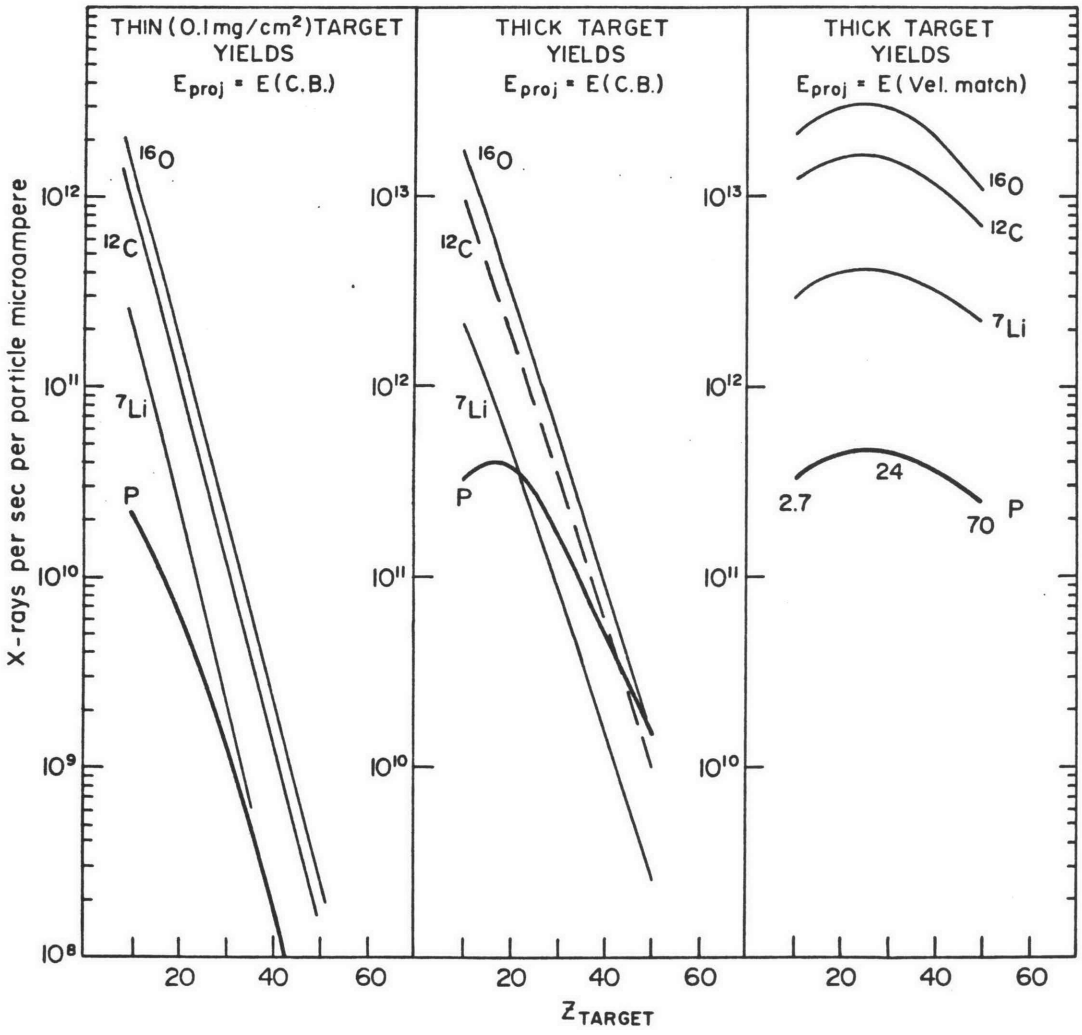


**Figure B.3**

**X-ray yields for thin and thick targets and for ions of Coulomb barrier and optimum energies.**

of the projectile is slower than the optimum value. The middle panel shows the yield for Coulomb barrier energies on a thick target. The yields are up substantially but the heavy ions only make a significant difference for the lightest targets where the absorption of the low energy x- rays determines the effective target thickness for all projectiles. As the targets get heavier the specific stopping power of the heavier ions determines the effective target thickness. The right panel of Figure B.3 shows the yield expected when the ion velocities approximately match the velocities of the K electrons and the production cross sections are close to maximum. These results are shown in order to bring out the Z dependence of the yield and to show the ultimate potential of heavy ions for x-ray production; the yields from C and O beams are in the range of $10^{13}$ per particle microampere (i.e. per $6x10^{12}$ particles). Very heavy projectiles may be practical for the production of the lowest x-ray energies. They are not of practical interest for the heavier targets since the required energies of the beams are very high; e.g. at Z = 50, the proton energy is 70 MeV and the oxygen energy must be 16 times higher.

## IXX

The conclusion from Figure B.1, left panel, is that IXX can result in ppm sensitivity with fluences of the order of $10^{10-11}$ if solid state detectors subtending large solid angles are used. According to Figure B.2, these requirements can be readily met in modest running times using small accelerators which can deliver microamperes of 4 MeV protons; higher energies are particularly useful for x-rays above about 13 keV; lowering the proton energies rapidly worsens the production efficiency.

Consider a typical poor geometry, Figure B.4. The sample subtends a solid angle of $\approx$2 msr and a proton intensity of $10\mu A$ of 4 MeV generators a flux of $1.5x10^{7}$ Mo x-rays, or $10^{8}$ /s Ge x-rays or $5x10^{10}$ /s Ti x-rays. Sensitivities at the ppm level are obtainable in less than 1000 seconds.

Figure B.5 shows a spectrum of induced x-rays from an NBS orchard leaves standard, taken with a 1 microampere, 3 MeV proton beam which generated Mo x-rays from a thick target; the geometry was more than an order of magnitude tighter than that of Figure B.4, the proton fluence was 1000 $\mu$C. All of the expected lines are observed including those from Rb(12 $\mu$g/g). The intensities agree with those expected from the standard with the exception of the Fe lines which show evidence of contamination traced to fluorescence in the nominally pure aluminum in the chamber.

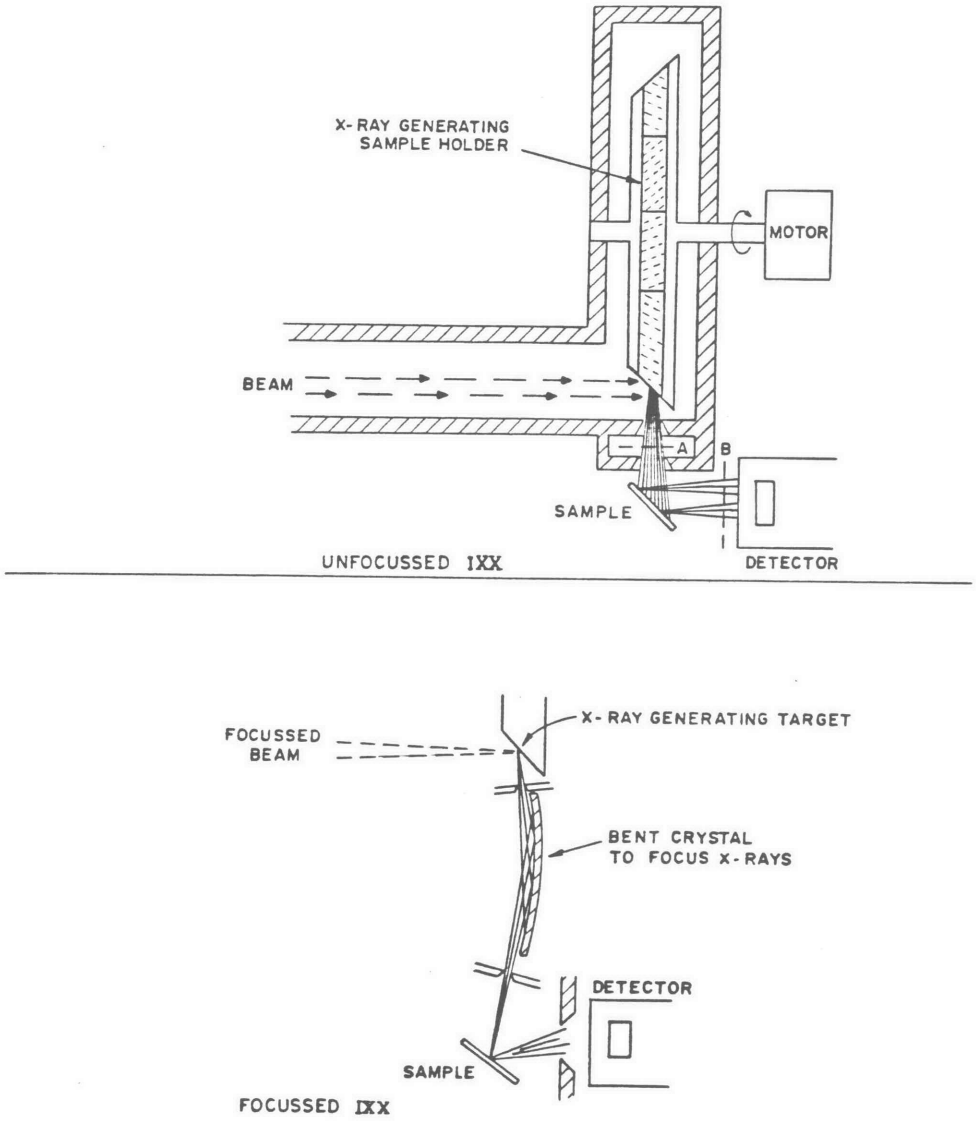


**Figure B.4**

**Schematic drawings of two possible ion induced x-ray configurations for x-ray fluorescence. For bulk analysis, the optics may be unfocussed as in Fig 4A. For probe studies, a focussed optics, depicted in Fig 4B, may be more appropriate.**

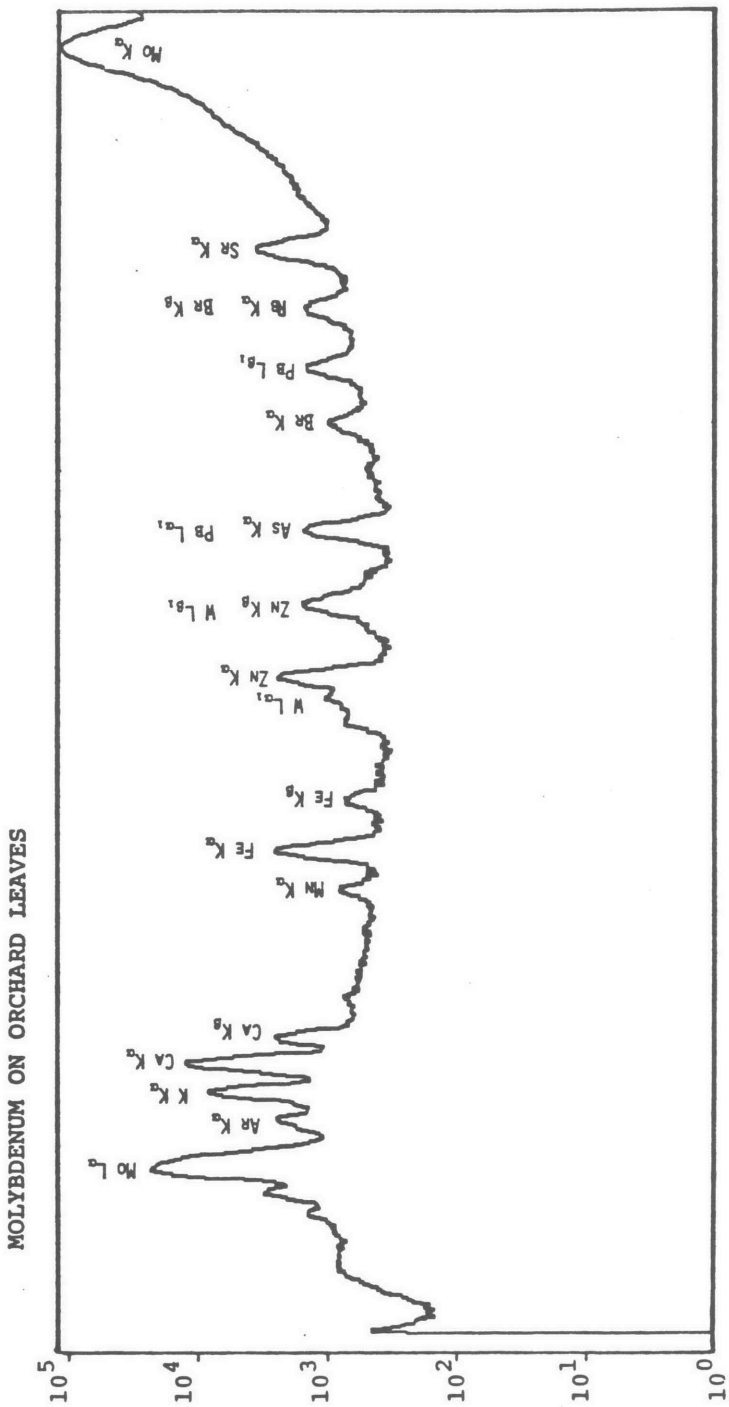


**Figure B.5**

**The x-ray distribution from an NBS orchard leaves standard bombarded with Mo x-rays generated by a 1 uA beam of 3 MeV protons.**

The need for pure materials in the collimating system and the generating chamber is already evident at the ppm level; the problem will become acute when one tries to attain sensitivities of 1 ppb. Other runs taken with Ni, Zn and Ge targets on NBS standards of bovine liver, orchard leaves and glass, confirmed the essential features of Figure B.1, left. For example, the Ni in orchard leaves present at 1.3 $\mu$g/g was easily observed with a good geometry run using a Ge target. A number of other examples of the results of IXX can be found in references [Pe,Ma,Li78].

IXX should be effective for x-ray probe studies. There is negligible bremsstrahlung accompanying the monochromatic x-rays which can be produced by ion beams focussed to micron dimensions. The focussing optics can therefore have very poor energy resolution, and good collection efficiency to concentrate a significant portion of the x-ray flux. One geometrical arrangement, Figure B.4, might use bent crystals of pyrolytic graphite, with an efficiency of $\approx 10^{-3}$ and $\approx 10^{-4}$ for Cu and Mo x-rays respectively, to demagnify by a factor of 10 or so, concentrating the monochromatic radiation to a 100 $\mu m^2$ or less; the focussing geometry must, of course, be changed appropriately for each x-ray energy. We stress the evident fact that the usefulness of focussing optics improves dramatically as the energy of the protons or heavier ions increases. But is should also be emphasized that focussing can be gainfully used for Ti and Cu x-rays even with the 4 MeV beams from smaller, high current accelerators which can deliver $> 10\mu A/cm^2$ . With such beams it should be possible to obtain $> 10^7$ /s monoenergetic photons in a $100\mu m$ spot. And that is sufficient for many studies of biological materials.

The higher the bombarding energy, up to the velocity matching condition, the higher the x-ray production cross section, and the smaller the specific energy loss in the target. The conversion of the proton energy to x-ray energy increases from $10^{-2}$% at 3 MeV to 0.3% at 25 MeV; higher proton energies are probably more efficient. These large energy-transfer efficiencies, which are approximately the same as obtainable with electron beams, make it interesting to consider a proton storage ring x-ray generator for IXX and other high intensity x-ray experiments.

A 100-150 MeV proton storage ring, storing 1mA of current, has been proposed [In]; it could produce a 10 $\mu$m diameter spot on a 1 $\mu g/cm^2$ internal gas target. Such beams will induce $10^{10-11}$ monoenergetic x-rays which could be focussed to ¡1$\mu$m, with flux densities in the range of $10^{7-8}/\mu^2$. Such flux densities are considerably less than those expected from the microprobe beams being proposed for synchrotron light

sources but the IXX microbeams could have much the better spatial resolution. IXX microbeams from storage ring sources would be powerful probes of trace elements at the cellular level in bio-medical samples.

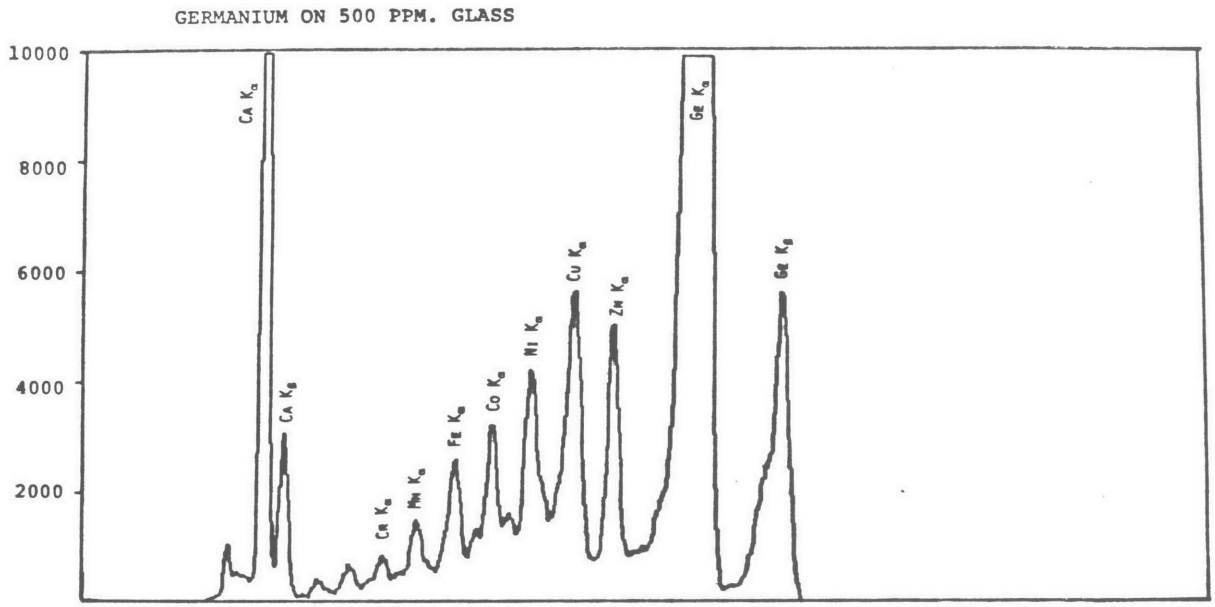
GERMANIUM ON 500 PPM. GLASS
10000
8000
6000
4000
2000
Ca Kα
Ca Kβ
Ca Kα
Mn Kα
Fe Kα
Co Kα
Ni Kα
Cu Kα
Zn Kα
Ge Kα
Ge Kβ

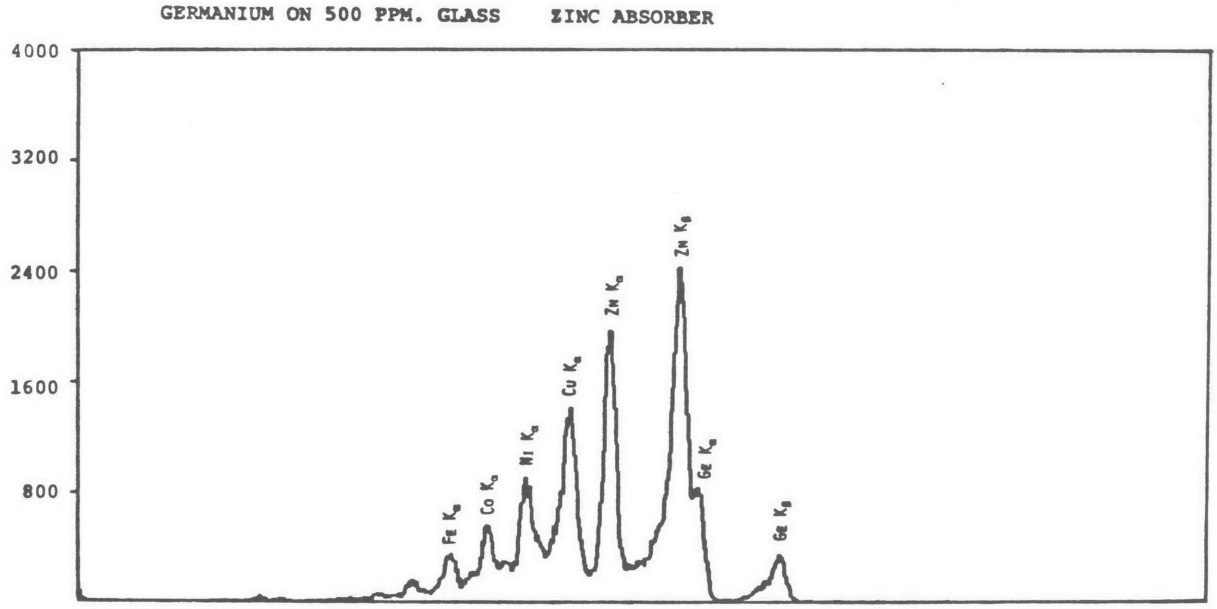
GERMANIUM ON 500 PPM. GLASS ZINC ABSORBER
4000
3200
2400
1600
800
Fe Kα
Co Kα
Ni Kα
Cu Kα
Zn Kα
Zn Kβ
Ge Kα
Ge Kβ

Figure B.6

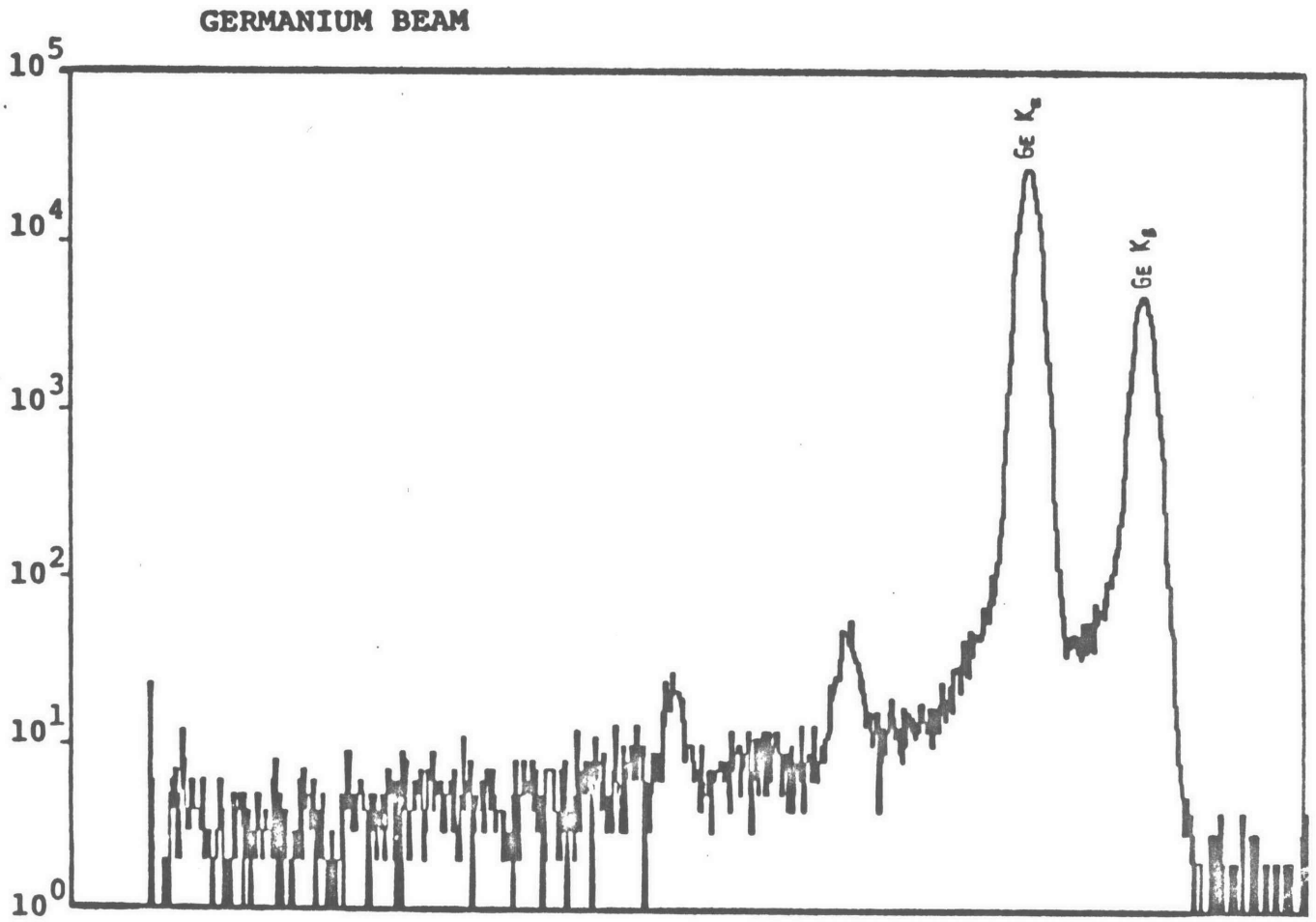


Figure B.7

# APPENDIX C

## SCANNING RUTHERFORD BACKSCATTERING SPECTROSCOPY

*P. Boisseau, L. Grodzins, P. Hurst*

*MIT Laboratory for Nuclear Science, Cambridge, Massachusetts*

A facility for scanning Rutherford Backscattering Spectroscopy has been developed. Spatially resolved RBS analysis has been used to characterize the concentration uniformity of oxygen and arsenic implanted silicon wafers. The technique allows rapid determination of implant dose and depth profile.

Rutherford Backscattering Spectroscopy (RBS) has, over the last several years, developed into an important technique for obtaining elemental depth profiles in material analysis. RBS has the advantages of good depth resolution ($\approx$ 200Å), sensitivity to a wide range of elements, and instrumental simplicity. Quantitative results can be easily obtained; this is aided by the availability of accurate computer programs for RBS spectrum synthesis.

A typical geometry for performing RBS analysis is shown in Figure 1. The sample is mounted in a fixed position relative to the beam and detector. The incident beam is typically a 2-3 MeV beam of alpha particles with a beam diameter on the order of 1mm. The detector is usually a surface-barrier type, positioned at an angle close to $180^o$. For the purpose of quantitative analysis, some means of measuring the incident beam intensity is usually provided. The use of a beam chopper with monitor detector is shown.

This arrangement is adequate for most purposes, and the addition of a multiple sample holder provides rapid interrogation of specimens. Frequently, however, it is important to measure how a the composition of a single specimen varies across its surface. The example discussed here is the determination of ion implant uniformity across single silicon wafers. To facilitate this kind of analysis, we have developed a scanning system to obtain spatially resolved RBS data for samples up to 10 centimeters in diameter.

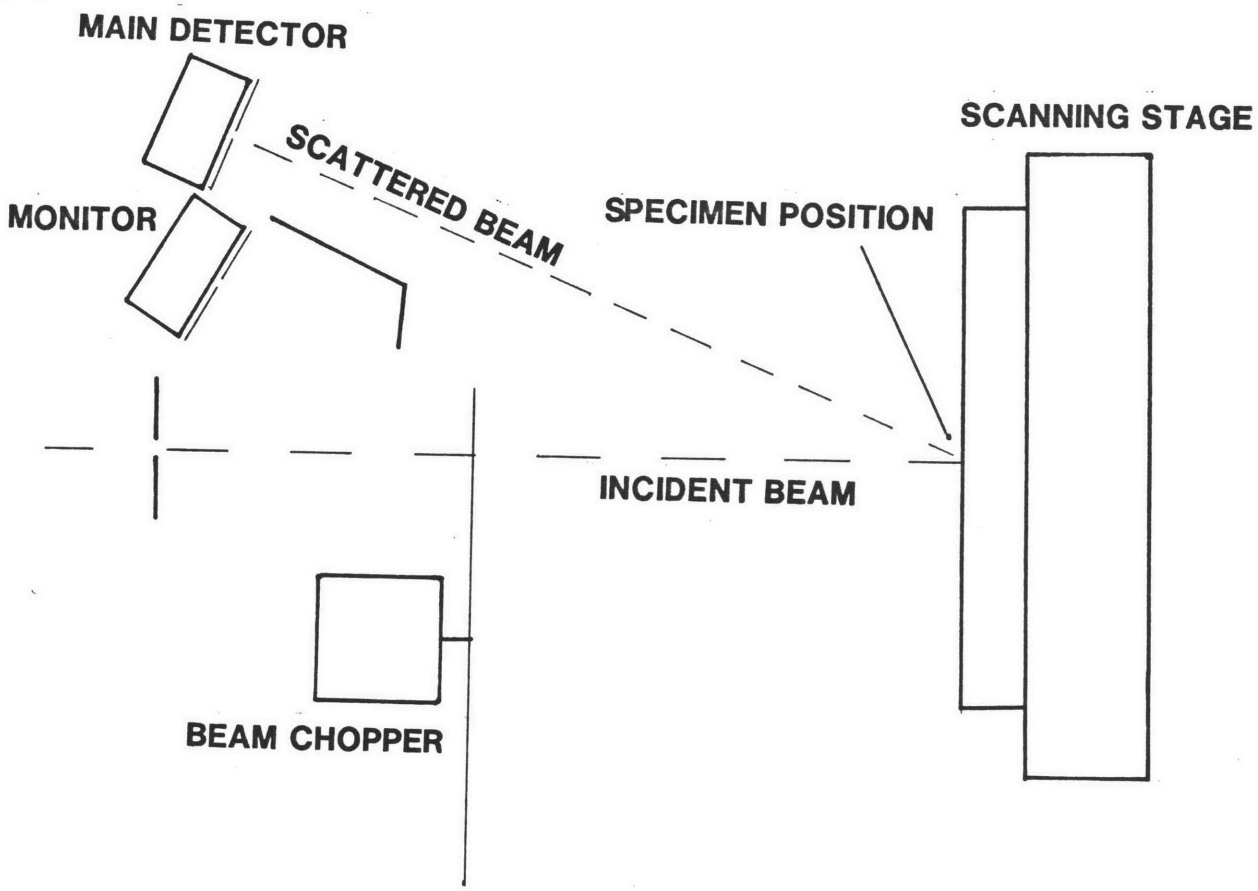


**Figure 1**
Typical Rutherford Backscattering Apparatus

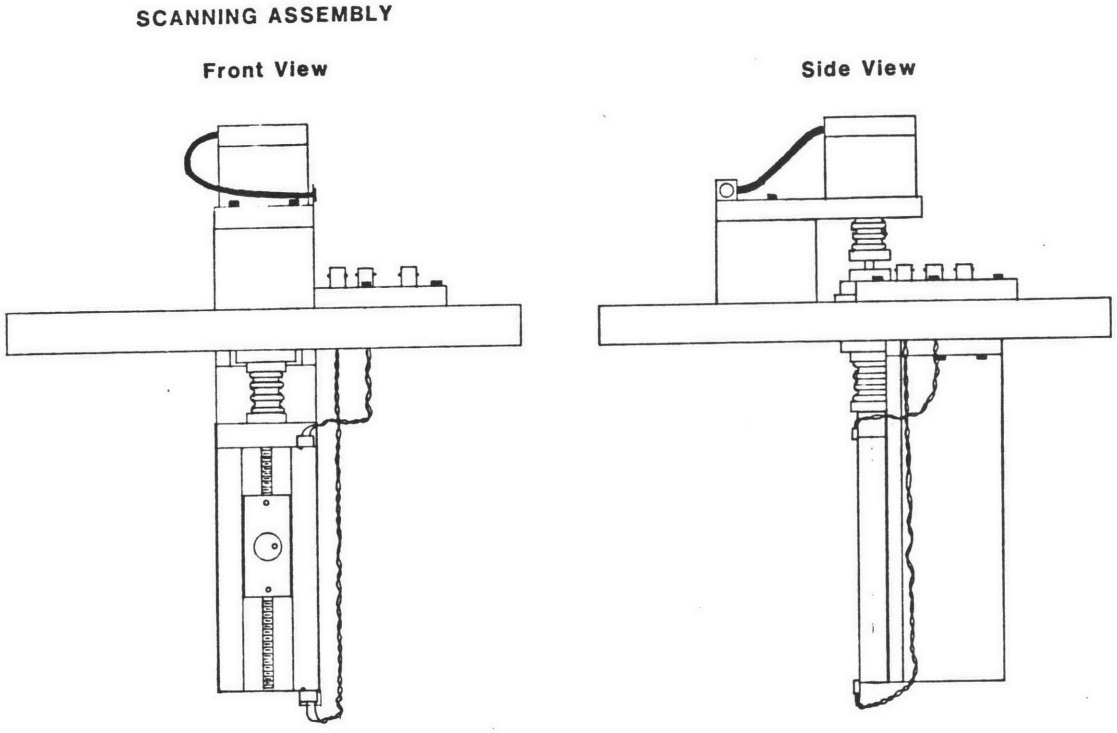


**Figure 2**
Linear Scanning Stage

The addition of a computer controlled scanning stage and appropriate software allows the acquistion of spatially resolved RBS. The beam/detector geometry is fixed, and the sample is scanned across the beam by means of a linear stage (Figure 2). The stage is driven by stepping motors under computer control, and has a minimum step size of 10 microns. Spatial resolution is thus limited by the diameter of the incident beam, which for the present results were 400-800 microns. The maximum scan length is 10cm., allowing a scan to span the diameter of a standard semiconductor wafer. The entire scanner can be rotated about its vertical axis.

Since it is difficult to collect total beam charge from the scanning stage, the beam intensity is measured indirectly. A second detector is used to collect particles backscattered from a rotating tantalum beam chopper. This signal is also collected point by point, allowing residual beam fluctuation effects to be removed. The chopper signal also the total beam dose to be determined for the purposes of quantitative analysis.

The data acquisition and control system allows the operator to select a scan of any length up to the 10cm limit. The scan is divided into a selectable number of data intervals, depending on the required spatial resolution. As the stage scans the specimen, a full 1024 channel spectrum is collected for each data interval. Individual spectra at all data intervals and spatial intensity maps of selected spectral regions may be generated during the acquisition. The scan is repeated continuously for the full data acquisition time to average out beam intensity fluctuations, as well as to minimize the effect of beam heating on the specimen.

The scanning method was used to examine silicon wafers implanted with approximately $10^{18}$ atoms/cm$^2$ of oxygen at 160 keV. The implantation was accomplished by rotating the wafers through a stationary beam of roughly rectangular crossection[]. The total oxygen dose and the temperature during implantation (500°C) was sufficient to create a saturated layer of $SiO_2$[]. It was expected that total oxygen dose would be uniform in the direction of rotation, and would reflect any nonuniformity of the ion beam in the direction perpendicular to the rotation. Data on the uniformity of both the total oxygen dose and the depth profile was needed.

RBS scans were taken radially from the center of the wafer to the edge, both parallel to the direction of rotation as well as in the perpendicular direction. Each radial scan was made up of 20 data points equally spaced. The RBS spectrum summed

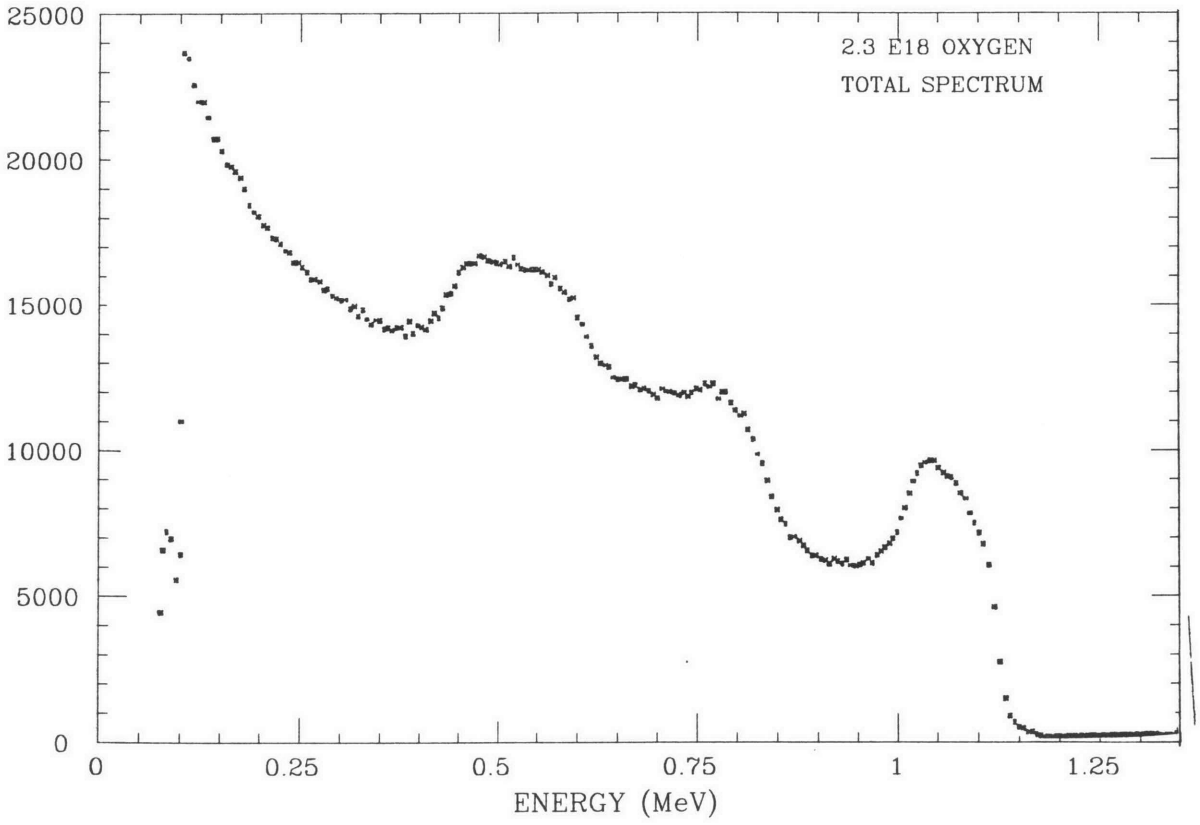


**Figure 3**

Total energy spectrum for backscattered alpha particles. The high energy edge at 1.125 MeV corresponds to scattering from the top surface of the silicon. Region #1 is the signal from the implanted oxygen. The dip in region #2 is due to the displacement of silicon by oxygen.

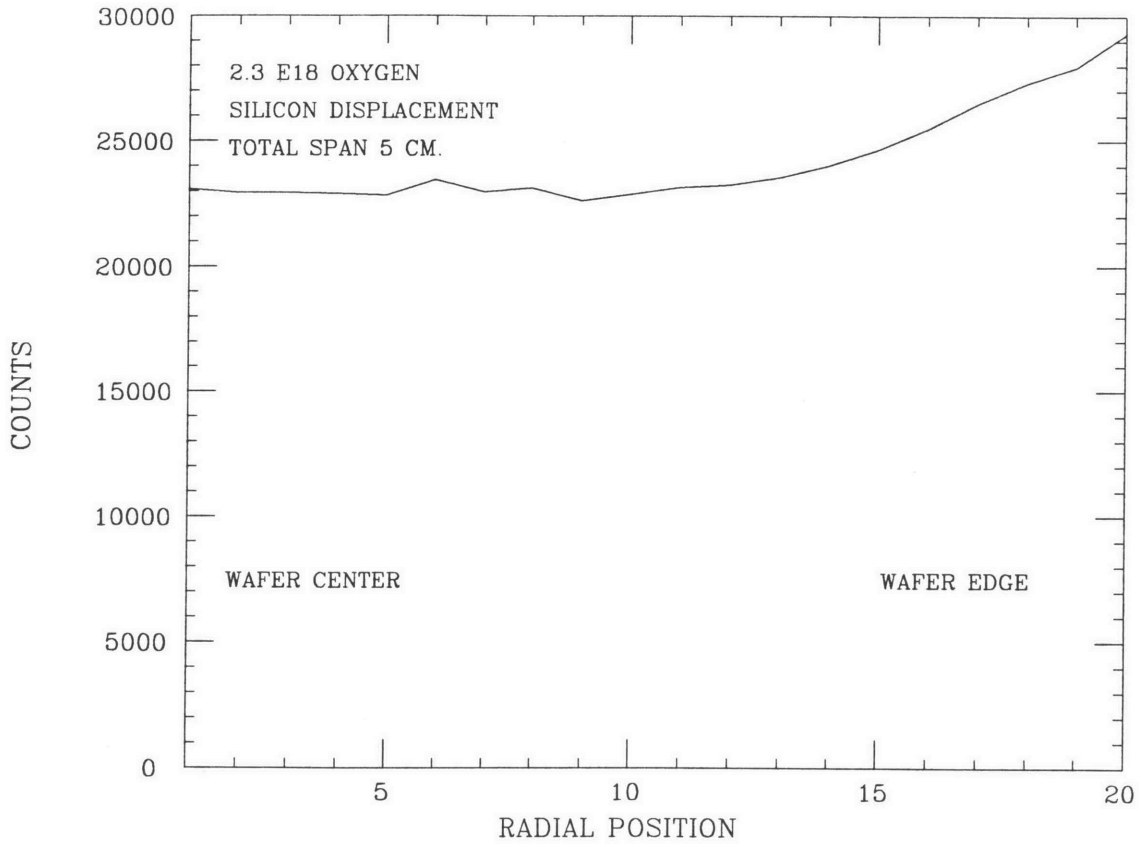


**Figure 4**

Intensity of region #2 as a function of position. The central dip corresponds to in increased oxygen concentration in the central region of the wafer.

over all spatial channels is shown in Fig 3. The oxygen containing layer results in an oxygen peak in the spectrum (region 1), and a corresponding dip in the silicon signal due to displacement of the silicon by oxygen (region 2). A plot of the depth of the region 2 dip, which is proportional to the oxygen dose is shown in Fig 4. The scan in the perpendicular direction shows a clear rolloff of the oxygen dose at the edge of the wafer. The distribution in the parallel direction is quite uniform.

A second oxygen implanted wafer, with a uniform dose, was scanned. In this wafer, there is a change in the depth profile from the center to the edge of the wafer; the distribution is shifted deeper near the center of the wafer. This corresponds to a visible stripe extending across the wafer diameter presumably caused by thin-film interference in the surface silicon layer. The change in implant depth suggests the existence of crystal channelling during the implantation process.

A silicon wafer implanted with $\approx 10^{16}$ arsenic atoms/cm$^2$ was examined. Two scans were performed; for the second scan the stage was oriented in such a way that planar channelling of the alpha beam could be observed. Spectra from the non channeled scan indicate a uniform dose of arsenic across the wafer, and a silicon signal characteristic of a non-channeled geometry. Spectra taken in the channeled configuration show an apparent variation in the arsenic dose, as well as a smooth radial variation in the degree of crystallinity.

**Conclusions** The enhancement of Rutherford Backscattering Spectroscopy with a computer controlled scanning system allows rapid and convenient characterization of dose and depth information for extended specimens. Although particularly convenient for the analysis of silicon wafers, it is expected that the system will be used for many of the analyses which would otherwise be done at a single point, and will undoubtedly provide important spatial information in specimens where no variation is expected.